SLAC-R-95-476
UC-414

MEASUREMENT OF THE POLARIZED FORWARD-BACKWARD ASYMMETRY OF B QUARKS USING MOMENTUM-WEIGHTED TRACK CHARGE AT SLD*

Thomas Robert Junk

Stanford Linear Accelerator Center
Stanford University, Stanford, CA 94309

SLAC-REPORT-95-476
November 1995

Prepared for the Department of Energy
under contract number DE-AC03-76SF00515

Printed in the United States of America. Available from the National Technical Information Service, U.S. Department of Commerce, 5285 Port Royal, Springfield, Virginia 22161

* Ph.D. thesis, Stanford University

Abstract

This thesis presents a direct measurement of the parity-violating parameter A_b by analyzing the polarized forward-backward asymmetry of b quarks in $e^+e^- \to Z^0 \to b\bar{b}$. Data were taken at the Stanford Linear Accelerator Center (SLAC), with the Stanford Large Detector (SLD), which records the products of e^+e^- interactions at a center of mass energy $\sqrt{s} = 91.2$ GeV/c^2 at the SLAC Linear Collider (SLC). The SLC/SLD experimental apparatus provides a unique and ideal environment for measuring electroweak asymmetries. Heavy flavor decays of the Z^0 were identified inclusively by taking advantage of the long lifetime of B hadrons, the small, stable SLC beam spot, and SLD's precise tracking detectors. Two analysis techniques for measuring A_b are presented: a binned fit to the left-right forward-backwards asymmetry of tagged events signed with momentum-weighted track charge, and a self-calibrating maximum-likelihood technique using momentum-weighted charge from the two hemispheres in each tagged event. From our 1994–1995 sample of 3.6 pb^{-1}, having a luminosity-weighted average e^- polarization of 77.3%, and our 1993 sample of 1.8 pb^{-1}, having a luminosity-weighted polarization of 63.1%, we obtain $A_b = 0.848 \pm 0.046(\text{stat.}) \pm 0.050(\text{syst.})$.

Acknowledgements

Behind every measurement in particle physics these days is the work of many people doing an enormous variety of tasks. With these people I have worked, played, and learned much, and I owe a deep debt of gratitude to each one. I must tender my apologies in advance for my deserving colleagues I have mistakenly left out.

First, I would like to thank my advisor, Rafe Schindler, for encouraging me to take part in the SLD experiment. His leadership example in the SLD heavy flavors working group inspired us all. His insistence on excellence in detector work and physics analysis has left its mark on many topics pursued at SLD, including this one. I have learned much as a graduate student, and Rafe has played an important role in my graduate experience.

For his courage and strength in the face of adversity, I thank Marty Breidenbach. It was his perserverance which kept SLD together and active, and which has paid off handsomely in physics results. And also for his kindness toward graduate students, I give him my deepest gratitude. Thanks go also to Charlie Baltay, our co-spokesman and statesman-at-large, who keeps SLD on the world map.

Special thanks go to Bruce Schumm, whose guidance and suggestions are integral to this thesis. Bruce shows by example and by critical participation, how careful physics analyses are done, and it is my hope to live up to those exacting standards in what I do. I would also like to thank Bruce for his unique sense of humor, which has lightened many a dark night at the terminal and on the experiment. I would like to thank Su Dong for his support of the heavy flavor physics group, his excellent troubleshooting ability, and his acumen with intricate physics topics. Su Dong always gave us something interesting to think about.

It has been a joy to work with the Compton polarimeter gang and the electroweak group — Mike Woods, Morris Swartz, Charlie Prescott, Peter Rowson, Mike Fero, Bruce Schumm, Dave Calloway, Eric Torrence, Ross King, Amit Lath, Ray Frey, Ken Moffeit, and Achim Wiedemann. Also many thanks to Guy Blaylock, whose beam energy measurements proved to be valuable diagnostics. It has also been a pleasure to work with the calorimeter crew — Iris Abt, Eric Vella, Tony Waite, Bill Wisniewski, Andy Bazarko, Peter Rowson, Behzad Sanii, and Brooks Collins. And the interface between the hardware, the data, the tapes, and the folks on shift, the online group: Jim Russell, Mike Huffer, Joanne Bogart, Dave Sherden, Owen Saxton, and Jack Hoeflich.

I don't think anyone on SLD had a better office companion than myself. Homer Neal has provided boundless energy, dedication, and good cheer to everything he does. His work on tagging $Z^0 \to b\bar{b}$ events has been used in the analysis presented in this thesis. I'll also relish my times with my fellow graduate students Mike and Holly Hildreth, Dave Williams, Tom Pavel, Jon Labs, Fritz DeJongh, Bijan Nemati, Pablo Saez, Matt Strassler, Jared Levy, Alex Hsieh, Chris Perez, Amanda Peet, Angela Cotera, Mary Jane Adriaans, Jie Zheng, Max Allen, Mark Ndesandjo and Mike Condron.

Special thanks to the SLAC theory group, particularly Michael Peskin, Joanne Hewett, and Tom Rizzo, who inspire us and give us renewed interest in our measurements.

I am positive the SLD collaboration would not function at all without Barbara Barrera, Margaret Helton, and Mary Brau; certainly not nearly as well without the good cheer and good sense they possess. The SLAC illustrations department has been invaluable in providing many illustrations used in this thesis.

The whole SLD gang have been great pals and guides these years – Tony Johnson, Richard Dubois, Terry Schalk, Len Moss, Karen Heidenreich, Jim Brau, Jenny Huber, Sarah Hedges, Bob Messner, Geordie Zapalac, Steve Wagner, Phil Burrows, Chris Dammerell, John Jaros, Bill Ash, Steve Manly, Dave Muller, Jaroslav Va'Vra, Tom Markiewicz, Leon Rochester, Tracy Usher, Joe Perl, Gary Bower, Hiro Masuda, Mary King, Takashi Muryama, Henry Band, and Dick Prepost. Thanks also to my friends Kevin Pitts, Eric Weiss, John Coller, Eric Church, Anthony Szumilo, Jingchen Zhou, Hyejoo Kang, Cheng Gang Fan, John Yamartino, Saul Gonzales, Nancy Mar, Donatella Falciai, Victor Serbo, Aaron Chou, Nety Krishna, Stefane Willocq, Xiaoqing Yang, Hwanbae Park, Ken Baird, and Peter Tenenbaum.

The SLC has been a difficult accelerator to commission and operate. The efforts of the physicists, operators, and technical staff have been heroic, and have brought about the success of the program. Special thanks to Nan Phinney, Mark Ross, Paul Emma, Franz-Joseph Decker, and the whole gang.

I would also like to thank my family for their support and encouragement through these years — My father William, my mother Lucille, and my brother Kenneth.

And lastly, I would like to thank Ann Williamson for her patience and support through these times that have been alternately trying and exhilirating.

Many heartfelt thanks to all the hard-working and fun people I have had as friends these past years.

Contents

List of Tables

List of Figures

Chapter 1

Introduction

This thesis presents a measurement of the polarized forward-backward asymmetry of b-quark production in e^+e^- collisions at $\sqrt{s} = 91.2$ GeV. This asymmetry provides a direct measurement of parity violation in the electroweak couplings of the bottom quark, in particular the difference between the strengths of the couplings of left-handed b quarks and right-handed b quarks to the Z^0 boson. The asymmetry is often referred to in the literature as A_b, and sometimes as A_b^{LR} or A_{LR}^b.

The experimental determination of A_b is under intense study worldwide, with efforts from SLC and the four LEP experiments; each year its measured value becomes more precise. Measuring A_b constitutes a stringent test of the predictions of the Standard Model, and may either confirm our current understanding of the fundamental interactions between elementary particles, or help point the way to extending our models and deepening our knowledge. Particular interest is focused on A_b at this time because recent, precise measurements of $R_b = \Gamma(Z^0 \to b\bar{b})/\Gamma(Z^0 \to \text{hadrons})$ show a noticeable discrepancy [1] with the prediction of the Standard Model and may be hinting at new phenomena modifying the interaction between the Z^0 and the b quark.

This measurement was performed at the Stanford Linear Accelerator Center (SLAC), using data collected in 1993-1995 with the SLAC Large Detector (SLD) at the Stanford Linear Collider (SLC). SLC is the first linear e^+e^- collider and produces Z^0 bosons on resonance in collisions of polarized electrons with unpolarized positrons. The SLD is an ideal experiment for studying electroweak physics and the physics of heavy flavor for several reasons. Roughly 22% of hadronic Z^0 decays are decays into $b\bar{b}$, and the resulting B hadrons receive a large boost in the laboratory frame of reference. The exceedingly small, stable beams of SLC, and the precision tracking performance of SLD allow analyses to take advantage of knowledge of both the production and decay points of long-lived heavy hadrons. The polarization of the electron beam consistently runs near 80%, and its helicity may be aligned either along or opposite the direction of travel.

With these tools, a direct measurement of the parity-violating couplings of the Z^0 to the b quark can be made. The remainder of this chapter presents this asymmetry in the context of the current understanding of elementary particle physics, and how a precise measurement of it may augment this understanding.

1.1 Introduction to the Standard Model

Physicists of the late 19^{th} century lived in a time in which nearly all observable phenomena could be accounted for with the existing models of the time: deterministic classical mechanics, Newtonian gravitation, Maxwell's recently unified description of electricity and magnetism, and thermodynamics. Only a few problems remained unexplained; three experimental, and one theoretical: radioactive decay, atomic line spectra, the blackbody radiation curve, and the description of propagating electromagnetic radiation in a moving frame. Investigation of these topics and the questions raised in the process opened the floodgates of physical discovery in the last one hundred years.

The road to our current model of the weak interactions began when Becquerel inadvertently left a photographic emulsion enclosed in a light-tight container under a sample of uranium salts and observed an exposure, thereby discovering spontaneous radioactive decay of heavy elements. In many ways, this interaction has been one of the more experimentally accessible ones and therefore one of the first observed, but also one of the most resistant to explanation. Weak interactions mediating nuclear decay take place on time scales easily measurable with ordinary clocks; the radioactive materials may be obtained from mines; and the detection apparatus is modest. At the time, neither the electron nor the nucleus had been discovered, so the origin of these rays remained a mystery.

In the mean time, investigations into the spectra of excited atomic hydrogen and the spectrum of thermal blackbody radiation gave birth in the 1920's to a quantum mechanical description of subatomic phenomena. Combining the formalism of quantum mechanics with special relativity in the early 1930's gave rise to the quantum field theory describing the interaction of charged particles and electromagnetic radiation, Quantum Electrodynamics (QED), to be described briefly below.

The observed spectrum of beta particles from radioactive decay of heavy nuclei was found to be continuous, which was not possible for a two-body decay of a heavy object. A third particle was introduced by Pauli, the neutrino, which would account for the missing energy and spin in beta decay [2]. Shortly thereafter, Enrico Fermi proposed a field-theoretic approach to describing beta decay by introducing a four-fermion vertex which coupled, for instance, a neutron, a proton, an electron, and a neutrino together at one point with a vector coupling. It was discovered that theories incorporating this vertex predicted infinite reaction probabilities once one-loop radiative correction calculations were attempted, even though experiments confirmed its tree-level predictions.

In 1956, Lee and Yang [3], after reviewing the literature, noticed that parity and charge-conjugation symmetries had not been checked in the weak interactions, and that they could possibly be violated. A series of experiments by Wu [4], Lederman, Garwin, and Schwartz [5], and Friedman and Telegdi [6] was conducted to test parity conservation in nuclear β-decay and in $\pi^{\pm}$ and $\mu^{\pm}$ decay, finding that parity was maximally violated by charged weak currents. It was observed that these currents coupled only to left-handed fermions and right-handed antifermions. Maximal parity violation could easily be introduced into the Fermi model by substituting the vector coupling by a $V - A$ coupling at the four-fermion vertex.

Yang and Mills proposed in 1956 [7] a formulation of quantum field theory that allowed the introduction of non-Abelian gauge symmetry groups, an extension of the Abelian symmetries of QED. Glashow [8], Weinberg [9], and Salam [10] proposed

Table 1.1: Fermion constituents of the Standard Model

$$\begin{pmatrix} \nu_e \\ e \end{pmatrix}_L \quad \begin{pmatrix} \nu_\mu \\ \mu \end{pmatrix}_L \quad \begin{pmatrix} \nu_\tau \\ \tau \end{pmatrix}_L \quad e_R \quad \mu_R \quad \tau_R$$

$$\begin{pmatrix} u \\ d \end{pmatrix}_L \quad \begin{pmatrix} c \\ s \end{pmatrix}_L \quad \begin{pmatrix} t \\ b \end{pmatrix}_L \quad \begin{matrix} u_R \\ d_R \end{matrix} \quad \begin{matrix} c_R \\ s_R \end{matrix} \quad \begin{matrix} t_R \\ b_R \end{matrix}$$

a model, described below, which incorporated both the electromagnetic and weak interactions as low-energy manifestations of a single interaction with $SU(2) \times U(1)$ gauge symmetry. The mediators of the electroweak force in this model are the photon (γ), the heavy Z^0 boson, and the charged doublet $W^\pm$.

At the outset, the Glashow-Weinberg-Salam model seemed beset with difficulties. It called for massive gauge bosons (mass terms could not be added to the Lagrangian and maintain gauge invariance), and it did not appear to be renormalizable. The first problem was addressed in Weinberg's paper [9] by incorporating the Higgs mechanism [11] of spontaneously breaking the symmetry of the theory in order to impart mass to the $W^\pm$ and the Z^0. The existence of a neutral, scalar Higgs boson remains unverified by experiment. Gerard t'Hooft solved [12] the renormalization problem in 1971, promoting the Weinberg-Salam model to a viable theory of electroweak interactions. The complete demonstration of the renormalizability of the electroweak theory requires fermions to be grouped in generations in order to cancel triangle anomalies.

Weak neutral currents, predicted by the Weinberg-Salam model, were first observed in 1973 [13][14] in the interactions $\overline{\nu}_\mu e \rightarrow \overline{\nu}_\mu e$, $\nu_\mu N \rightarrow \nu_\mu X$, and $\overline{\nu}_\mu N \rightarrow \overline{\nu}_\mu X$. Neutral currents are carried therefore by both the photon and the Z^0, and their amplitudes interfere.

A further vindication of the model came from the discovery of the J/ψ, a $c\overline{c}$ bound state. The charm quark was predicted by the GIM mechanism [15] as an explanation for the lack of flavor-changing neutral currents in decays of the kaon. A third generation, heralded by the discovery of the τ lepton in 1975 [16], and filled in with the discovery of the Υ meson, a bound $b\bar{b}$ state, in 1977 [17], and finally the t quark in 1995 [18][19], confirmed the basic doublet structure of fermions. In the gauge boson sector, the $W^{\pm}$ and the Z^0 were first identified in hadronic $p\bar{p}$ collisions at the $SP\overline{P}S$ collider at CERN in 1983 [20][21].

1.2 The Electroweak Interaction

The next two sections outline the electroweak sector of the Standard Model. Detailed presentations of this material may also be found in References [23], and [24], and [27]. This presentation roughly follows the notation and logic of Halzen and Martin [22].

1.2.1 The Electromagnetic Interaction

The most elegant formulations of physical models are the ones that start with the fewest postulates and describe the broadest range of observable behavior. Here we will start with the postulate of local gauge invariance and arrive at the formulation of QED. The Dirac equation for spin-1/2 particles,

$$(i\gamma^{\mu}\partial_{\mu} - m)\psi = 0 \tag{1.1}$$

can be obtained from the Lagrangian

$$\mathcal{L} = i\overline{\psi}\gamma_{\mu}\partial^{\mu}\psi - m\overline{\psi}\psi. \tag{1.2}$$

This Lagrangian is already invariant under the transformation

$$\psi(x) \rightarrow e^{i\alpha}\psi(x), \tag{1.3}$$

where α is a constant. This global symmetry, through an application of Noether's theorem, requires the conservation of electric charge:

$$\partial_{\mu}j^{\mu} = 0, \tag{1.4}$$

where

$$j^{\mu} = -e\overline{\psi}\gamma^{\mu}\psi. \tag{1.5}$$

If the phase $e^{i\alpha}$ is allowed to be a function of space and time, then the Lagrangian in Equation 1.2 is no longer invariant due to the presence of the derivative. The necessary modification to preserve local gauge invariance is to replace the derivative ∂_μ with a "covariant derivative" D_μ:

$$\mathcal{L} = i\overline{\psi}\gamma_\mu D^\mu \psi - m\overline{\psi}\psi, \tag{1.6}$$

with

$$D_\mu = \partial_\mu - ieA_\mu, \tag{1.7}$$

where the field A_μ transforms as

$$A_\mu \rightarrow A_\mu + \frac{1}{e}\partial_\mu \alpha. \tag{1.8}$$

Finally, a photon kinetic energy term must be added, and local gauge invariance restricts its form to combinations of the field strength tensor $F_{\mu\nu}$. The QED Lagrangian then follows:

$$\mathcal{L} = \overline{\psi}(i\gamma^\mu \partial_\mu - m)\psi + e\overline{\psi}\gamma^\mu A_\mu \psi - \frac{1}{4}F_{\mu\nu}F^{\mu\nu}. \tag{1.9}$$

with

$$F_{\mu\nu} = \partial_\mu A_\nu - \partial_\nu A_\mu. \tag{1.10}$$

This gauge symmetry precludes adding a term proportional to $A_\mu A^\mu$ and therefore requires that the photon be massless, unless the symmetry is broken by an interaction with another field. There currently is no experimental evidence for photon mass. and the upper bound is set at 3×10^{-27} eV/c^2 [25].

1.2.2 Unification With the Weak Force

Because the weak interaction couples left-handed particles within isodoublets (the right-handed versions of the fermions do not interact with the charged weak current). we seek a local gauge symmetry with the same symmetry as the spin-$\frac{1}{2}$ representation of the rotation group. The group $SU(2)$ is chosen for this; a convenient set of generators is the set of Pauli matrices $\sigma^i, i = 1, 2, 3$. This symmetry is often referred to as $SU(2)_L$ because it describes the sector that interacts with only the left-handed fermions. The gauge transformation for the weak current then becomes

$$\psi \rightarrow e^{ig\frac{\sigma^i}{2}\Lambda^i}\psi, \tag{1.11}$$

where the Λ^i are three real functions of space and time and g is a constant. As before, it is necessary to introduce new fields into the theory in order to preserve the gauge invariance of the derivative term. The covariant derivative has the form

$$D_\mu = \partial_\mu - ig\frac{\sigma^i}{2}W^i_\mu, \tag{1.12}$$

where the three additional fields W^i_μ describe a massless isotriplet of gauge bosons. Because the Pauli matrices σ^i do not commute, the gauge transformation of the W^i_μ must include an extra term:

$$W^i_\mu \rightarrow W^i_\mu + \partial_\mu\Lambda^i - g\vec{\Lambda}\times\vec{W}_\mu. \tag{1.13}$$

The additional term adds an interaction between the gauge bosons. This feature is not surprising, since the weak charged bosons must interact with the photon at tree level. The kinetic energy term in the Lagrangian, $-\frac{1}{4}\vec{W}_{\mu\nu}\cdot\vec{W}^{\mu\nu}$, uses a form of the field strength tensor slightly modified from the QED case:

$$W^i_{\mu\nu} = \partial_\mu W^i_\nu - \partial_\nu W^i_\mu - g\vec{W}_\mu\times\vec{W}_\nu. \tag{1.14}$$

The new fields W^i_μ interact with an isospin triplet of weak currents,

$$J^i_\mu = \overline{\chi}_L\gamma_\mu\frac{\sigma^i}{2}\chi_L, \tag{1.15}$$

where χ_L is one of the left-handed isodoublets of Table 1.1.

In addition to the $SU(2)_L$ symmetry, the $U(1)$ symmetry of QED is incorporated. Because weak neutral currents do not have a pure $V-A$ form, the neutral member of the weak isotriplet mentioned above cannot alone be the correct representation. Instead, a linear combination of the gauge boson of the $U(1)$ symmetry and the neutral member of the above isotriplet is sought. The generator of the $U(1)$ symmetry is then named the "weak hypercharge" Y, and is defined to be

$$Y \equiv 2(Q - T^3), \tag{1.16}$$

Table 1.2: Fermion quantum numbers. The second and third generations of quarks and leptons have identical quantum numbers. There is no right-handed neutrino in the Standard Model because it cannot interact with any of the gauge bosons.

	Fermion	T	T^3	Q	Y
Leptons	ν_e	$\frac{1}{2}$	$\frac{1}{2}$	0	-1
	e_L^-	$\frac{1}{2}$	$-\frac{1}{2}$	-1	-1
	e_R^-	0	0	-1	-2
Quarks	u_L	$\frac{1}{2}$	$\frac{1}{2}$	$\frac{2}{3}$	$\frac{1}{3}$
	d_L	$\frac{1}{2}$	$-\frac{1}{2}$	$-\frac{1}{3}$	$\frac{1}{3}$
	u_R	0	0	$\frac{2}{3}$	$\frac{4}{3}$
	d_R	0	0	$-\frac{1}{3}$	$-\frac{2}{3}$

where Q is charge and T^3 is the third component of isospin (see Table 1.2 for a listing of T^3 for the fermions in the Standard Model). The corresponding current follows immediately:

$$J_\mu^Y = 2(J_\mu^{em} - J_\mu^3) \tag{1.17}$$

The gauge group generated by Y is often referred to as $U(1)_Y$. The gauge field introduced to maintain local $U(1)_Y$ invariance is labeled B_μ and carries an independent coupling constant g'. The interaction term in the Lagrangian becomes

$$\mathcal{L}_{int}^{EW} = -ig(J^i)^\mu W_\mu^i - i\frac{g'}{2}(J^Y)^\mu B_\mu. \tag{1.18}$$

The fields

$$W_\mu^\pm = \sqrt{\frac{1}{2}}(W_\mu^1 \mp iW_\mu^2) \tag{1.19}$$

describe the physical weak charged currents and W_μ^3 and B_μ are neutral fields. The linear combination of neutral fields necessary to represent the physical neutral gauge bosons γ and Z^0 is not specified by the theory, but may be parameterized by the Weinberg angle θ_W:

$$A_\mu = B_\mu \cos\theta_W + W_\mu^3 \sin\theta_W, \tag{1.20}$$

and

$$Z_\mu = -B_\mu \sin\theta_W + W_\mu^3 \cos\theta_W. \tag{1.21}$$

Since the coupling of the electromagnetic current J_μ to the photon field has strength e, we may identify the couplings

$$g \sin\theta_W = g' \cos\theta_W = e, \tag{1.22}$$

which has the immediate consequence

$$\tan\theta_W = \frac{g'}{g}. \tag{1.23}$$

At this point, the only parameters of the electroweak interaction that need to be determined from experiment are the values of the coupling constant e and the Weinberg angle θ_W.

1.2.3 Spontaneous Symmetry Breaking and Gauge Boson Masses

In the previous section we have ignored the fact that some of the gauge bosons indeed have mass. It is this mass that makes the weak interactions "weak." After all, the coupling constants are closely related to the QED coupling, yet the forces mediate interactions that happen much more slowly than electromagnetic ones. The weakness of the weak force is just a manifestation of the denominator of the propagator of the $W^\pm$ and the Z^0. For low-Q^2 interactions, the energy dependence of the propagator is dwarfed by the masses of the weak bosons ($\sim$90 GeV), that it can be safely approximated by a constant that can be combined with the coupling constant to form an effective strength at low energies.

Introduction of mass into the electroweak model has to be done with some delicacy, because the $SU(2)_L \times U(1)_Y$ symmetry prohibits mass terms of the form $M_W^2 W_\mu W^\mu$ just as the QED $U(1)$ symmetry does. The goal is to introduce an interaction whose Lagrangian preserves the $SU(2)_L \times U(1)_Y$ symmetry, but whose ground state breaks it. It is not necessary to break the entire symmetry group, as the photon is to remain massless — the $U(1)_{EM}$ subgroup of the theory is to remain unbroken.

The solution involves hypothesizing four additional scalar fields ϕ_i and adding to the Lagrangian of the Standard Model the term

$$\mathcal{L}_{Higgs} = \left| \left(i\partial_\mu - g\sigma^i W^i_\mu - g' \frac{Y}{2} B_\mu \right) \phi \right|^2 - V(\phi) \tag{1.24}$$

The simplest choice of fields ϕ that preserve the gauge invariance of $\mathcal{L}_{Higgs}$ is an isodoublet with weak hypercharge $Y = 1$, a choice originally made by Weinberg:

$$\phi = \begin{pmatrix} (\phi_1 + i\phi_2)/\sqrt{2} \\ (\phi_3 + i\phi_4)/\sqrt{2} \end{pmatrix} \tag{1.25}$$

The symmetry is broken by a judicious choice of the potential function

$$V(\phi) = \mu^2 \phi^\dagger \phi + \frac{\lambda}{2} (\phi^\dagger \phi)^2, \tag{1.26}$$

chosen with $\mu^2 < 0$ and $\lambda > 0$. This potential is minimized when

$$\phi^\dagger \phi = -\mu^2 / \lambda. \tag{1.27}$$

This set of ϕ that minimizes V is invariant under $SU(2)$ transformations. although when the system settles into a ground state, it only chooses one point among the possible ones. Without loss of generality we may set ϕ_1, ϕ_2, and ϕ_4 to zero, then

$$\phi_3^2 = -\frac{\mu^2}{\lambda} \equiv v^2, \tag{1.28}$$

The vacuum ϕ in this case is

$$\phi_0 = \sqrt{\frac{1}{2}} \begin{pmatrix} 0 \\ v \end{pmatrix}. \tag{1.29}$$

Because there are four degrees of freedom of ϕ and only one constraint which specifies the minimum, the minimizing manifold is three-dimensional. Since ϕ may fluctuate within this manifold without an energy penalty, these fluctuations correspond to three massless Nambu-Goldstone bosons [26]. These additional degrees of freedom are actually just overcounting the gauge degrees of freedom, and do not appear in the standard Lagrangian. The remaining degree of freedom corresponds to a physical scalar Higgs field h with a particle whose mass is $-\lambda v^2/2$. The relevant mass-generating term for the gauge bosons in Equation 1.24, expressed in the basis of physical gauge bosons, then is

$$\left|\left(-ig\frac{1}{2}\sigma^i W^i_\mu - i\frac{g'}{2}B_\mu\right)\phi\right|^2 =$$
$$(\frac{1}{2}vg)^2 W^+_\mu W^{-\mu} + \frac{1}{8}v^2\left[gW^3_\mu - g'B_\mu\right]^2 + 0\left[g'W^3_\mu + gB_\mu\right]^2. \tag{1.30}$$

From this relation, the coefficients of the terms quadratic in the fields yield the masses of the vector bosons. The mass of the charged W is the simplest, with

$$M_{W^\pm} = \frac{1}{2}vg. \tag{1.31}$$

Using 1.20, 1.21, and 1.23, we obtain

$$A_\mu = \frac{g'W^3_\mu + gB_\mu}{\sqrt{g^2 + g'^2}} \tag{1.32}$$

for the photon, and so its mass coefficient is zero from Equation 1.30, and

$$Z_\mu = \frac{gW^3_\mu - g'B_\mu}{\sqrt{g^2 + g'^2}}, \tag{1.33}$$

yielding the Z^0 mass, also read off from Equation 1.30

$$M_Z = \frac{1}{2}v\sqrt{g^2 + g'^2}. \tag{1.34}$$

Combining 1.34 with 1.31 yields the relation

$$\frac{M_W}{M_Z} = \rho\cos\theta_W, \tag{1.35}$$

where $\rho = 1$ until radiative corrections are applied.

The parameters of the electroweak sector of the Standard model number three. They are e, $\sin^2\theta_W$, and v, the vacuum expectation value of the Higgs. In terms of observables that can be measured with precision, three necessary parameters are α_{EM}, M_Z, and G_μ. With these three parameters, Standard Model predictions at tree level (modulo effects like phase space which depend on fermion masses). At one loop, the masses of fermions and the Higgs mass enter, and non-standard phenomena may have effects at energies achievable with current accelerators.

1.3 The Strong Interaction

An integral portion of the standard picture of elementary particle interactions is the model of the strong interaction. Various detailed treatments are available in the literature [27] [22]. The strong interaction has many features which differentiate it from the electroweak interaction, although both can be formulated as local gauge theories. These differences include

- *Range.* The strong interaction has a very short range, while the electromagnetic portion of the electroweak interaction has an infinite range.
- *Asymptotic Freedom.* The strength of the strong interaction decreases with increasing Q^2 of the interaction. This feature was observed first in deep-inelastic $e - p$ scattering.
- *Confinement.* The partons within hadrons cannot be isolated. No observable particle has a bare color charge.
- *Symmetry.* The strong interaction obeys flavor symmetry and also conserves parity.
- *Hadron Structure.* Quarks are bound within hadrons which contain either three quarks, three antiquarks, or a quark and an antiquark.

The quark model originally contained a paradox regarding the structure of hadrons. Some baryons, it seemed, violated the spin-statistics theorem in that three quarks in them seemed to occupy the same quantum state. These hadrons include the Δ^{++} and the Ω^-. The flavor assignments for the quarks are all the same, for both of these baryons, and each quark only has two spin states available to it, so there is no assignment of spins that can preserve the Pauli exclusion principle. Furthermore, the spin of the Δ^{++} was found to be 3/2, indicating that all three quarks shared the same spin state. Another degree of freedom with at least three distinct values needed to be introduced to preserve the statistics.

The model which grew out of that necessity and which best describes the strong interactions is referred to as "Quantum Chromodynamics," and is formulated as a non-Abelian Yang-Mills gauge theory with $SU(3)$ as its symmetry group; each quark transforms as a triplet (three values of the color charge). The local gauge symmetry for QCD for a quark of flavor $k = u,d,s,c,b$, or t is

$$q_k \rightarrow e^{ig\lambda_a\Lambda_a} q_k, \tag{1.36}$$

where the λ_a are the eight generator matrices of $SU(3)$, commonly known as Gell-Mann matrices, and Λ_a are functions of space and time. To construct a covariant derivative that is gauge invariant, eight fields A^a_μ, corresponding to eight bi-colored gluons, must be introduced in the same way as they were for the electroweak interaction:

$$D_\mu q_k = (\partial_\mu - igA_\mu)q_k, \tag{1.37}$$

with

$$A_\mu = \sum_{a=1}^{8} A^a_\mu \lambda^a/2. \tag{1.38}$$

The coupling constant g is a single parameter left to be determined experimentally. The Lagrangian can then be expressed as

$$\mathcal{L}_{QCD} = -\frac{1}{2}\mathrm{tr}G_{\mu\nu}G^{\mu\nu} + \sum_{k=1}^{n_{flavors}} \overline{q}_k(i\gamma^\mu D_\mu - m_k)q_k, \tag{1.39}$$

with the field-strength tensor $G_{\mu\nu}$ defined similarly to that of QED, with a non-Abelian piece added:

$$G_{\mu\nu} = \partial_\mu A_\nu - \partial_\nu A_\mu - ig\left[A_\mu, A_\nu\right]. \tag{1.40}$$

In this manner, QCD has been referred to as "eight copies of QED," although its non-Abelian nature lends it some rather unique properties.

The non-Abelian terms in the QCD Lagrangian give rise to interactions between gluons, the gauge bosons of QCD. This is a manifestation of the property of gluons in that not only do they couple to objects with color charge, they themselves carry color charge. The new diagrams introduced into the theory are a triple-gluon vertex, as well as a four-gluon vertex, shown in Figure 1.1

In contrast to the electroweak gauge boson sector, there is no evidence for gluon mass, and so the mechanism of spontaneous symmetry breaking is not necessary.

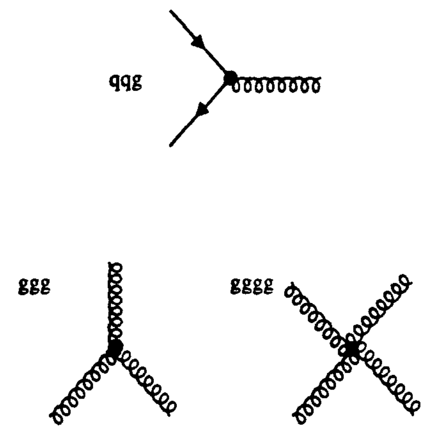

Figure 1.1: Vertex diagrams in QCD.

Further evidence for QCD comes from the energy-dependent behavior of

$$R_{had} = \frac{\Gamma(e^+e^- \to \text{hadrons})}{\Gamma(e^+e^- \to \mu^+\mu^-)}. \tag{1.41}$$

This function shows distinct energy thresholds, marked by resonances at which $q\overline{q}$ pairs are produced that form vector mesons. Above these thresholds, R_{had} assumes a higher value because of the availability of more hadronic final states. The rate for $e^+e^- \to \mu^+\mu^-$ is readily calculable from QED (and the electroweak interaction at higher energies), and so jumps in the value of R_{had} above thresholds quantitatively measure the numbers of new available final states. It is observed that the changes in R_{had} correspond to three times that which would be naïvely predicted if the quark color degrees of freedom were ignored.

This model of strong interactions has the requisite ingredients to satisfy the properties listed at the beginning of this section. In particular, the non-Abelian self-interaction of the gluons provides QCD with the ability to explain asymptotic freedom [28][27]. In contrast to the Abelian QCD case, in which the vacuum polarizes to screen charges at large distances, the QCD vacuum actually anti-screens charges, and its coupling becomes stronger at large distances and lower energy scales. This feature of QCD is the reason many believe it has the ability to model quark confinement, although a rigorous demonstration has not been produced yet.

If a quark within a hadron is struck, say, with an impinging photon, it will pull away from the other quark(s) in the hadron. Because the strength of the color interaction increases with distance, energy stored in the field of gluons between the quarks builds as the struck quark moves away. At some point, it becomes energetically favorable to produce a $q\bar{q}$ pair from the vacuum. The colors chosen for the new $q\bar{q}$ pair must be chosen so that the newly formed hadrons are color singlets. It is this process, called *fragmentation*, which gives the hadronic decays of the Z^0 their characteristic structure in the SLD; quarks are not observed in the final state, even though very high-energy, back-to-back quarks are produced by the decay. Instead, a large number of color-singlet hadrons, traveling in largely the same directions as the original quarks, appears in the detector. This process of hadron formation cannot be predicted perturbatively, although it can be modeled with computer simulation. A recursive algorithm was proposed by Feynman and Field [29], and its latest implementation for simulations of e^+e^- collisions is the JETSET 7.4 Monte Carlo [30][31], used in this thesis.

The property of asymptotic freedom also plays a role in the structure of Z^0 decays. Very high-Q^2 processes may be modeled perturbatively because the strong coupling constant α_s has a relatively small value at high energy. The value of α_s at the Z^0 energies is $\sim$0.12, with ambiguities arising from the different techniques for measuring it and their interpretations. Perturbation theory for the strong interactions is not quite as safe as that for QED, owing to its larger coupling constant — it is not clear whether some perturbative series converge at all. Modeling of non-perturbative effects may be accomplished with the aid of lattice QCD computer simulations [32].

Nonetheless, perturbative QCD radiation plays a large role in hadronic Z^0 decay. Visible in many such decays is a third "jet" of final-state hadrons, corresponding to a hard gluon radiated by the quarks [33]. Because the gluon is a colored object which may not escape to large distances, it too must fragment into hadrons. The rate at which this process happens is a measure of α_s, although the energy scale of this interaction is somewhat ambiguous [34][35].

The combined effect of hard gluon radiation and the fragmentation process removes energy from the original quark emitted by the Z^0. For the case of $Z^0 \rightarrow u\overline{u}$ or $Z^0 \rightarrow d\overline{d}$, the many quarks pulled from the vacuum are indistinguishable from the ones into which the Z^0 decayed. But in the case of a heavy flavor decay of the Z^0, there is only one heavy-flavor hadron in each hemisphere, and the fragmentation function, describing the energy of that hadron as a fraction of half of $\sqrt{s}$, is well defined. For the light-flavor decays of the Z^0, the energy-loss fraction is an important ingredient in the recursive algorithm describing the hadronization process.

The fragmentation function describing the momentum of the fastest hadron in light-quark events is well parameterized by the "Lund symmetric function:" [30]

$$f(z) \propto z^{-1}(1-z^2)^a e^{-bm_\perp^2/z}, \tag{1.42}$$

where $z = 2E(\text{hadron})/\sqrt{s}$, $m_\perp$ is the "transverse mass"

$$m_\perp^2 = E^2 - p_{||}^2, \tag{1.43}$$

and a and b are tunable parameters. The fragmentation function iteratively describes hadron formation for lower-energy hadrons in the parton shower. The parameters a and b typically have values of 0.18 and 0.34 GeV^{-2} [36] so the momentum distributions of final-state particles best match available data. It is called a "symmetric" function because it describes a breaking string as viewed either from either end. This model has been tremendously successful at a wide range of energies. The values of a and b were originally tuned at PETRA energies and the model reproduces the observed hadron spectrum at LEP energies with very little further adjustment.

The model above does not describe heavy flavor production very well; the actual fragmentation function for c and b quarks is much harder than that for the light flavors. The reason the heavy hadron carries a larger fraction of the available energy is described in [37]. In short, the additional hadrons formed in the fragmentation process are produced with a speed (or boost, γ) that is less than the speed (or γ) of the leading heavy quark. Because the γ of the heavy quark before the fragmentation process scales as $1/m_Q$, the energy fractions the extra fragmentation tracks receive is $\sim$1 GeV$/m_Q$.

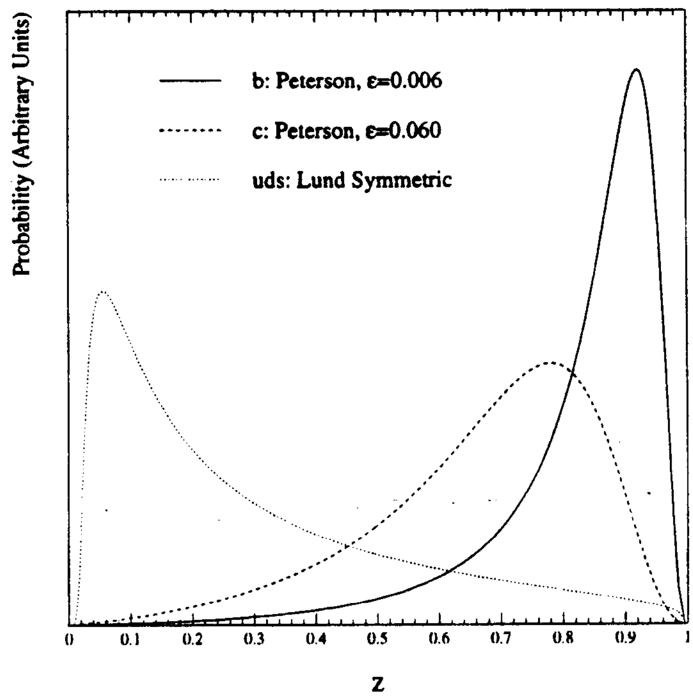

Figure 1.2: The fragmentation functions for uds, c, and b. The Lund symmetric function, described in the text, depends strongly on the value of $m_\perp$, which is chosen on each splitting. Shown here is the Lund symmetric function with $m_\perp = 300\text{MeV}/\text{c}^2$

The fragmentation function commonly used to model $Z^0 \to b\bar{b}$ and $Z^0 \to c\bar{c}$ is the Peterson function:

$$f(z) \propto \frac{1}{z\,(1-(1/z)-\epsilon_Q/(1-z))^2}, \tag{1.44}$$

with the parameter ϵ_Q chosen to be 0.060 for c quarks, and 0.006 for b quarks. These fragmentation distributions are shown in Figure 1.2. The stiffness of the b fragmentation function is one of the features that allows a momentum-weighted charge measurement of A_b to be effective, because weighting the tracks' charges with their momenta de-emphasizes the role of fragmentation tracks.

1.4 Tree-Level Asymmetries at the Z^0

Observable asymmetries on the Z^0 resonance depend almost entirely on the couplings of fermions to the Z^0, but since there is a small contribution from s-channel γ exchange, it will be included here. The couplings of the fermions to the Z^0 and the γ are summarized in Table 1.3 [38]. The notation is described below.

The neutral current coupling of a fermion f to the Z^0 has vector and axial-vector components parameterized by v^{Zf} and a^{Zf}:

$$J^{Zf} \propto \overline{f}(v^{Zf} + a^{Zf}\gamma_5)f. \tag{1.45}$$

The coupling of the same fermion f to the photon is purely a vector coupling and its strength is proportional to the charge of the fermion Q_f. Because the spin projection operators have the forms

$$\begin{aligned} P_L &= (1-\gamma_5)/2, \quad \text{and} \\ P_R &= (1+\gamma_5)/2, \end{aligned} \tag{1.46}$$

the left-handed and right-handed couplings of the fermion f to the Z^0 may be defined to be

$$\begin{aligned} c_L^{Zf} &= (v^{Zf} + a^{Zf})/2, \quad \text{and} \\ c_R^{Zf} &= (v^{Zf} - a^{Zf})/2. \end{aligned} \tag{1.47}$$

The energy dependence of the observable asymmetries to be described has its origin in the combination of two gauge bosons, the γ and the Z^0, in the propagator. When adding the graphs of Figure 1.3, the matrix element for $e^+e^- \to f\overline{f}$ is

$$M_{ij} = \left(\frac{e}{\sin\theta_W \cos\theta_W}\right)^2 \frac{-i}{s - m_Z^2 + i\Gamma_Z m_Z} c_i^{Ze} c_j^{Zf} + e^2 \frac{-i}{s} Q_e Q_f, \tag{1.48}$$

where $i, j = L, R$ are the helicity indices for the initial state electron and final-state fermion respectively.

In what follows, only the angular and initial- and final-state helicity dependences of the differential cross-sections will be retained, and the energy dependence of the

Table 1.3: Chiral couplings of the standard fermions to the γ and Z^0. The couplings to the γ are spin-independent and depend only on the charge Q_f.

		Z^0 coupling			
fermion	Q_f	v^{Zf}	a^{Zf}	c_R^{Zf}	c_L^{Zf}
e, μ, τ	-1	$-\frac{1}{2} + 2\sin^2\theta_W$	$-\frac{1}{2}$	$\sin^2\theta_W$	$-\frac{1}{2} + \sin^2\theta_W$
ν_e, ν_μ, ν_τ	0	$\frac{1}{2}$	$\frac{1}{2}$	0	$\frac{1}{2}$
u, c, t	$\frac{2}{3}$	$\frac{1}{2} - \frac{4}{3}\sin^2\theta_W$	$\frac{1}{2}$	$-\frac{2}{3}\sin^2\theta_W$	$\frac{1}{2} - \frac{2}{3}\sin^2\theta_W$
d, s, b	$-\frac{1}{3}$	$-\frac{1}{2} + \frac{2}{3}\sin^2\theta_W$	$-\frac{1}{2}$	$\frac{1}{3}\sin^2\theta_W$	$-\frac{1}{2} + \frac{1}{3}\sin^2\theta_W$

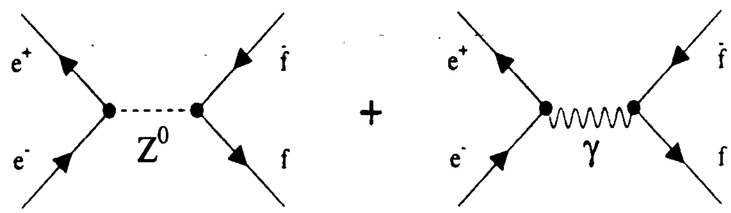

Figure 1.3: Tree-level electroweak contributions to $e^+e^- \to f\bar{f}$ in the Standard Model.

total cross section will be factored out. In addition, the final state e^+e^- will be omitted because there is an additional t-channel γ-exchange diagram which contributes significantly, and even diverges at small scattering angles.

Equation 1.48 provides a definition of the left- and right-handed couplings to the combined electroweak current. It is convenient in what follows to express the product $c_i^e c_j^f$ with the same helicity indices i, j as before:

$$c_i^e c_j^f = c_i^{Ze} c_j^{Zf} + Q_e Q_f \Lambda, \tag{1.49}$$

where

$$\Lambda(s) = \frac{s - m_Z^2 + i\Gamma_Z m_Z}{s} \sin^2\theta_W \cos^2\theta_W. \tag{1.50}$$

The square of the combined couplings appears in the final cross sections, so a more useful combination is

$$\left|c_i^e c_j^f\right|^2 = \left(c_i^{Ze} c_j^{Zf}\right) + 2c_i^{Ze} c_j^{Zf} Q_e Q_f \mathrm{Re}\{\Lambda(s)\} + Q_e^2 Q_f^2 |\Lambda(s)|^2. \tag{1.51}$$

The first term of this relation is the pure Z^0 coupling; the last is a γ-exchange term, and the middle term is the $\gamma - Z$ interference term. If $s = m_Z^2$, this interference term vanishes, reducing the sensitivity of asymmetry measurements to additional neutral gauge bosons, including the photon.

If θ is defined to be the angle between the incoming e^- beam and the outgoing fermion f, then

$$\frac{d\sigma_{RR}}{d\Omega} \propto \left(c_R^e c_R^f\right)^2 (1 + \cos^2\theta + 2\cos\theta), \tag{1.52}$$

$$\frac{d\sigma_{LL}}{d\Omega} \propto \left(c_L^e c_L^f\right)^2 (1 + \cos^2\theta + 2\cos\theta), \tag{1.53}$$

$$\frac{d\sigma_{LR}}{d\Omega} \propto \left(c_L^e c_R^f\right)^2 (1 + \cos^2\theta - 2\cos\theta), \tag{1.54}$$

and

$$\frac{d\sigma_{RL}}{d\Omega} \propto \left(c_R^e c_L^f\right)^2 (1 + \cos^2\theta - 2\cos\theta). \tag{1.55}$$

The helicity of the positron is not specified because it is fixed by the helicity of the incoming electron beam. A left-handed electron will only couple with a right-handed positron at the Zee vertex owing to helicity conservation at high energies*. The above relations convey in their functional form only the conservation of angular momentum; the actual parity violation comes about by the differing values of c_R^f and c_L^f. This can easily be summarized in that if a Z^0 is produced with a right-handed electron beam traveling in the $+\hat{z}$ direction, then the expectation value of the spin of the Z^0 is unity in the $+\hat{z}$ direction. Since the Z^0 prefers to couple to left-handed fermions and right-handed antifermions, then the antifermion will be sent forwards (along the direction of travel of the e^-) preferentially, and the fermion backwards, in order to conserve angular momentum.

The polarization of the outgoing fermion cannot be ascertained from experimental observables, except in the important case of the τ, so the polarized cross-sections must

*It is helicity conservation that suppresses direct production of scalars at high-energy e^+e^- machines, by a factor of m_e^2/s.

Table 1.4: Values of A_f for $\sin^2\theta_W$=0.23, calculated with radiative corrections in reference [39], and their sensitivity to $\sin^2\theta_W$.

Fermion type	A_f	$\frac{\partial A_f}{\partial \sin^2\theta_W}$
e, μ, τ	0.16	-7.85
u, c, t	0.67	-3.45
d, s, b	0.94	-0.63

be summed over final-state fermion polarizations to obtain

$$\frac{d\sigma_R}{d\Omega} \propto \left[(c_R^{f2} + c_L^{f2})(1+\cos^2\theta) + 2(c_R^{f2} - c_L^{f2})\cos\theta\right] \tag{1.56}$$

and

$$\frac{d\sigma_L}{d\Omega} \propto \left[(c_R^{f2} + c_L^{f2})(1+\cos^2\theta) - 2(c_R^{f2} - c_L^{f2})\cos\theta\right], \tag{1.57}$$

where the helicity index on σ refers now only to the incident electron beam. As a further simplification, we may combine the fermion couplings into asymmetry parameters

$$A_f \equiv \frac{2v_f a_f}{v_f^2 + a_f^2} = \frac{c_L^f - c_R^f}{c_L^f + c_R^f}. \tag{1.58}$$

Substituting in the vector and axial vector couplings of the fermions to the Z^0 in terms of $\sin^2\theta_W$, before radiative corrections,

$$A_f^{SM,Born} = \frac{1 + |Q_f|^2\sin^2\theta_W}{1 + (1 + |Q_f|^2\sin^2\theta_W)^2}. \tag{1.59}$$

The mass of the final-state fermion couples its L and R states and gives it a finite probability to flip its spin. The modification to the A_f parameter is [40]†

$$A_f = \frac{2\beta v_f a_f}{\frac{3-\beta^2}{2}v_f^2 + \beta^2 a_f^2}, \tag{1.60}$$

†In reference [40], both the formulas for the β-dependent A_f and β have typographical errors. The correct formulas are presented here.

where $\beta^2 = 1 - 4\frac{m_f^2}{m_Z^2}$ is the speed of the outgoing fermion. For the b quark, this increases the expected asymmetry by ~0.02% and will be accounted for in this thesis.

Using the parameters A_f, omitting the dependence on energy, and creating a linear combination of L and R polarization states to form a partially unpolarized initial state, the angular dependence of the differential cross section can be expressed as

$$\frac{d\sigma^f(P_e)}{d\cos\theta} \propto (1 - A_e P_e)(1 + \cos^2\theta) + 2(A_e - P_e)A_f \cos\theta, \tag{1.61}$$

where P_e is the polarization of the incoming electron beam. With this formalism, we may then parameterize the tree-level Standard Model predictions of observable asymmetries A_{LR}, A_{FB}^f, $A_{FB}^{\tau pol}$, and $\tilde{A}_{FB}^f$.

1.4.1 The Left-Right Production Asymmetry A_{LR}

One of the simplest and most powerful asymmetries that can be formed with an experiment with a polarized electron beam is the left-right asymmetry A_{LR} which directly measures the asymmetry in the chiral couplings of electrons to the Z^0. It is measured by producing equal amounts of luminosity using a left-handed and right-handed electron beam on unpolarized positrons. It then remains to count the $f\bar{f}$ final states (rejecting the e^+e^- final state) for both initial helicities and form the asymmetry

$$A_{LR}^{raw} = \frac{N_L - N_R}{N_L + N_R} = P_e A_e. \tag{1.62}$$

SLD's measurements of A_{LR} are described in References [41] and [42].

One of the main virtues of this asymmetry is that it does not require the isolation of any particular final state, except the experimentally distinct e^+e^- state. Another benefit of this measurement is that it is very insensitive to the details of the detector. As long as its detection efficiency for fermions is the same as that for antifermions at each value of cosθ, efficiency effects cancel in the ratio. Because the Z^0 decays into a back-to-back fermion-antifermion pair, this detection efficiency can be further safeguarded by building a detector that is symmetric about its midplane perpendicular to the beam axis. Its third virtue is that it is a very sensitive measurement of $\sin^2\theta_W$. Its dependence can be obtained from Equation 1.59 and is listed in Table 1.4. Given

SLC's electron polarization of 77% in 1994, this single asymmetry provides the most powerful technique of measuring $\sin^2\theta_W$ at present.

The $\sin^2\theta_W$ that is measured by A_{LR} is a physical parameter, and so necessarily incorporates effects of propagator and vertex radiative corrections, to be described in Section 1.5. The measurement, however, is corrected for the effects of initial-state radiation, which may be calculated from QED. The measurement yields $\sin^2\theta_W^{eff}$, the "effective" weak mixing angle parameter [43], which parameterizes the remaining radiative corrections. Vertex corrections at the final vertex do not affect the couplings at the initial vertex significantly, unless the energy is far from the Z^0 pole and γ exchange becomes significant. The most important radiative corrections are the vacuum polarization diagrams in the gauge boson propagator. These lend to A_{LR} sensitivity to m_{top} as well as m_{Higgs}. With the recent measurements of m_{top} from CDF [18] and D0 [19], this measurement may provide the best knowledge of what mass the Higgs boson is expected to have.

The dependence of A_{LR} on the colliding energy of the beams is shown in Figure 1.4, highlighting the need to correct for off-pole measurements.

1.4.2 Unpolarized Forward-Backward Asymmetries A^f_{FB}

In the absence of a polarized electron beam, electroweak asymmetry measurements must rely on other parity-violating asymmetries. One of these approaches is to compare the number of fermions of a particular species which travel forwards in the detector (along the direction of the electron beam) to those that travel backwards. Because the Z^0 couples preferentially to the left-handed component of the unpolarized electron beam, the expectation value of its spin along the $\hat{z}$ axis does not vanish, and there is an asymmetry in the forward-backward distribution of fermions in the final state, A^f_{FB}. This asymmetry relies on parity violation at both the production and decay vertices, so its value is proportional to the product of initial- and final-state coupling asymmetries:

$$A^f_{FB}(P_e = 0) = \frac{\sigma^f_F - \sigma^f_B}{\sigma^f_F - \sigma^f_B} = \frac{3}{4}A_e A_f, \tag{1.63}$$

where

$$\sigma_B = \int_{-1}^{0} \frac{d\sigma}{d\cos\theta} d\cos\theta, \tag{1.64}$$

and

$$\sigma_F = \int_{0}^{1} \frac{d\sigma}{d\cos\theta} d\cos\theta. \tag{1.65}$$

The differential cross-sections $\sigma_{F,B}$ are averaged over initial state polarizations and summed over final state polarizations, as at an unpolarized experiment, there is no control over either one. Care must be taken, however, that the initial state is genuinely unpolarized, as the effect on the cross section of any residual polarization is quite dramatic.

One feature of the definition of A^f_{FB} is that it involves an asymmetry of cross sections integrated over $\cos\theta$, and particle detectors invariably have a loss of acceptance at large values of $|\cos\theta|$ owing to their solenoidal nature and the necessity of having an aperture for the beams. A more ideal quantity to form involves finding the forward-backward asymmetry as a function of $|\cos\theta$ and then fitting the function

$$A^f_{FB}(|\cos\theta|) = \frac{\sigma^f(\cos\theta) - \sigma^f(-\cos\theta)}{\sigma^f(\cos\theta) + \sigma^f(-\cos\theta)} = A_e A_f \frac{2|\cos\theta|}{1+\cos^2\theta} \tag{1.66}$$

to it. With this technique, the detector acceptance function cancels in the numerator and denominator of the formed asymmetry, if it is binned finely enough.

For the lepton final states $\mu^+\mu^-$ and $\tau^+\tau^-$ this asymmetry measures the products $A_e A_\mu$ and $A_e A_\tau$. Assuming that the lepton coupling asymmetries are identical, then the quantity A_e^2 is measured, with its strong dependence on $\sin^2\theta_W$ given in Table 1.4.

To improve the statistical power of the measurement of $\sin^2\theta_W$ at LEP, A^b_{FB} is measured, largely because the value of A_b is large in the Standard Model, 0.94, and because pure and efficient samples of $Z^0 \to b\bar{b}$ may be obtained by either tagging high-P_T leptons from B decay, or by using precision vertex detectors to identify long-lived particles. Nonetheless, it is still the combination $\frac{3}{4}A_e A_b$ which is measured, with most of the dependence on $\sin^2\theta_W$ coming from A_e. The Standard Model must be invoked to provide a prediction of A_b in order to extract $\sin^2\theta_W$.

The energy dependence of A^b_{FB} is shown in Figure 1.4. The LEP accelerator performs energy scans, so the energy dependence of this asymmetry near the Z^0 pole can be measured by each of the LEP experiments.

1.4.3 Forward-Backward Tau Polarization Asymmetry $A_{FB}^{P(\tau)}$

An e^+e^- experiment with unpolarized beams is incapable of measuring A_{LR} directly, and the A_{FB}^f measurements are sensitive to a product of asymmetries. If there is new physics at a vertex or just a poorly modeled radiative correction, then the extraction of A_e from the A_{FB}^f will be incorrect. The asymmetry of $e^+e^- \to e^+e^-$ would reduce the assumptions on the asymmetries, but its value is modified by t-channel exchange diagrams.

Nonetheless, an independent measurement of A_e can be made at an unpolarized experiment, provided that the data sample is large. The technique used is to measure the final-state polarization of τ leptons from Z^0 decay. The taus themselves have asymmetric couplings to the Z^0, and exhibit a forward-backward asymmetry. The polarization of the taus as a function of polar angle depends only on the expectation value of the spin of the Z^0, and is a consequence of angular momentum conservation, as expressed in equations 1.52–1.55. Using these relations, one may derive the expectation value of the final-state fermion polarization,

$$P_\tau(\theta) = \frac{-A_\tau(1+\cos^2\theta) + 2F(P_e)\cos\theta}{1+\cos^2\theta - 2A_\tau F(P_e)\cos\theta}, \tag{1.67}$$

where

$$F(P_e) = \frac{P_e - A_e}{1 - P_e A_e}. \tag{1.68}$$

If the electron beam is unpolarized, then

$$P_\tau = \frac{-A_\tau - A_e\,(2\cos\theta/(1+\cos^2\theta))}{1 + A_\tau A_e\,(2\cos\theta/(1+\cos^2\theta))}. \tag{1.69}$$

A measurement of the polar angle distribution of the final-state fermion polarization can be fit to Formula 1.69, with A_τ and A_e as independent parameters. This fit provides very nearly uncorrelated measurements of A_e and A_τ. The reason for this separation is that the denominator of Equation 1.69 is very near unity, which enables the average polarization to yield information about A_τ while the angular dependence yields information about A_e.

The reason the $Z^0 \to \tau^+\tau^-$ channel is chosen is because the average final state polarization of the taus may be measured, owing to the helicity dependence of the distribution of the decay products. In particular, the channels $\tau \rightarrow e\overline{\nu}_e\nu_\tau$, $\tau \rightarrow \mu\overline{\nu}_\mu\nu_\tau$, $\tau \rightarrow \pi\nu_\tau$, $\tau \rightarrow \rho\nu_\tau$, and $\tau \rightarrow a_1\nu_\tau$ contain information about the helicity of the parent tau [44].

1.4.4 Polarized Forward-Backward Asymmetries $\tilde{A}^f_{FB}$

The availability of one polarized beam enables an independent combination of cross sections to be formed from Equation 1.61. This combination is often called the "left-right forward-backward asymmetry" because it involves forming a combination that is antisymmetric in both beam helicity and cosθ, and is denoted $\tilde{A}^f_{FB}$:

$$\tilde{A}^f_{FB} = \frac{\sigma^f_{FL} - \sigma^f_{BL} + \sigma^f_{BR} - \sigma^f_{FR}}{\sigma^f_{FL} + \sigma^f_{BL} + \sigma^f_{BR} + \sigma^f_{FR}}, \tag{1.70}$$

where L and R refer to the helicity of the incident electron beam; F and B have the same definitions as in Equations 1.65 and 1.64. The positron beam is assumed to be unpolarized. If the electron beam has polarization P_e, then this asymmetry can be expressed in terms of the coupling asymmetry using Equation 1.61:

$$\tilde{A}^f_{FB} = \frac{3}{4}P_e A_f. \tag{1.71}$$

Measuring this asymmetry was first proposed by Blondel, Lynn, Renard, and Verzegnassi [39] in 1988, and SLD's measurements are described in References [45], [46], [47], [48], [49], [50], and this thesis.

One of the most important reasons for studying this asymmetry is that it is independent of the asymmetry in the couplings of the initial state. While the combination $A_e A_f$ can be measured for various fermions f at LEP, SLD is able to factor that expression and measure A_e and A_f independently. The importance of this arises from the need to constrain corrections to the Zff vertex independently of those to the Zee vertex, because couplings to new particles at at the vertex could be different.

It is also the case that for the particular final state of $b\overline{b}$, the dependence on $\sin^2\theta_W$ is very small, as can be calculated at Born level from Equation 1.59. Radiative corrections do not modify the dependence of A_b on $\sin^2\theta_W$ much, as can be seen in Table 1.4. This is simply a re-expression of the fact that A_b is relatively insensitive to propagator corrections, in part due to the b quark's small coupling to the photon. As will be shown later, Standard Model vertex corrections also have very little effect on A_b. For these reasons, the Standard Model has a very narrow range of predictions of A_b as a function of m_{top} and m_{Higgs}. If any discrepancy were found in its value, it almost certainly is a sign of new phenomena.

Naturally, the argument for the unpolarized case, found in Equation 1.66, which cancels the detector acceptance as a function of polar angle, also applies to this asymmetry:

$$\tilde{A}^f_{FB}(|\cos\theta|) = \frac{\sigma^f_L(\cos\theta) - \sigma^f_L(-\cos\theta) + \sigma^f_R(-\cos\theta) - \sigma^f_R(\cos\theta)}{\sigma^f_L(\cos\theta) + \sigma^f_L(-\cos\theta) + \sigma^f_R(-\cos\theta) + \sigma^f_R(\cos\theta)} = P_e A_f \frac{2|\cos\theta|}{1+\cos^2\theta}. \tag{1.72}$$

The energy dependence of A^b_{LR}, shown in Figure 1.4, is minimal, due largely to the fact that the $\gamma - Z$ interference is small. Energies deviating from the Z^0 pole energy increase the relative fraction of right-handed coupling of the b quark to the electroweak neutral current, owing to the larger contribution of the photon exchange graph.

1.5 Radiative Corrections

Radiative corrections modify the Born-level cross-sections and asymmetries and must be included in models in order to fit observations. Some corrections arise from the ordinary physics of QED and QCD, and others are modifications arising from particles that have yet to be discovered. It is important to correct for the known effects, so as to arrive at unbiased estimations of what effect new physics has on the measurements.

1.5.1 Bremsstrahlung

Bremsstrahlung, the radiation of energy from accelerated charges, has classical and quantum-mechanical pictures. This radiation can take two forms — initial state radiation (ISR) of photons from the incoming electron and positron, and final-state radiation (FSR), primarily of gluons, from quarks. Quarks also couple to the electromagnetic field, but the radiation cross-section is suppressed by $(\alpha_{EM}/\alpha_s)^2$, in

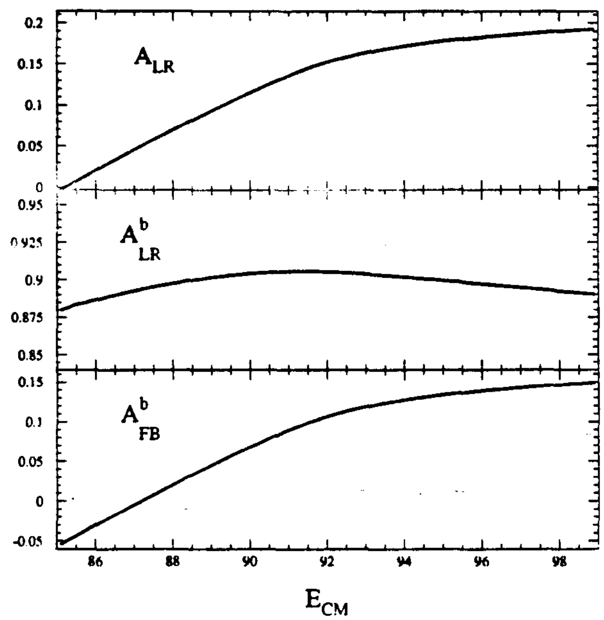

Figure 1.4: Dependence of the asymmetries A_{LR}, A^b_{LR}, and A^b_{FB} on the center-of mass energy. Results are obtained from ZFITTER [51] using $\alpha_s = 0.118$, $m_t = 180$, $m_{Higgs} = 300$. and $m_Z = 91.187$.

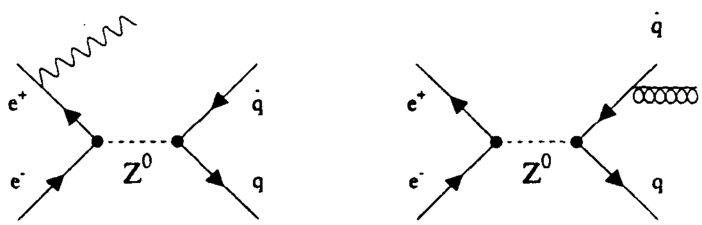

Figure 1.5: Lowest-order bremsstrahlung contributions to $e^+e^- \to Z^0 \to q\bar{q}$ — initial state photon radiation, and final-state gluon radiation.

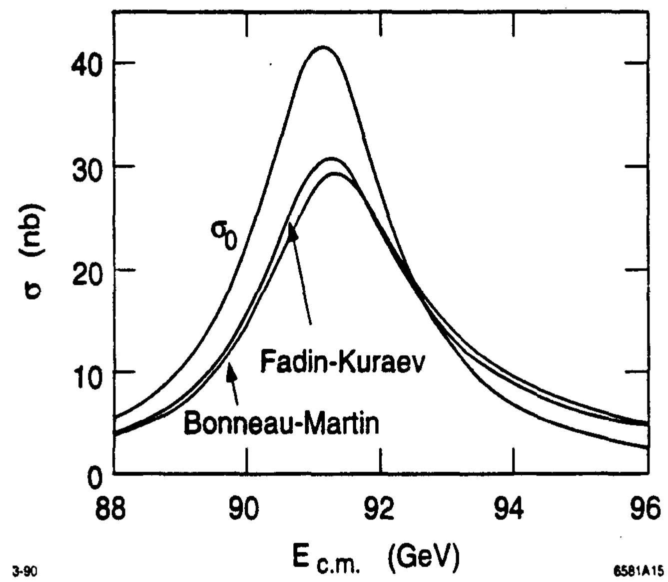

Figure 1.6: Corrections to the Z^0 lineshape from ISR. The uncorrected cross section is denoted σ_0. From reference [52].

addition to the fractional charge on the quark. Initial-state radiation photons travel predominantly down the beampipe and escape undetected. The effect of initial-state radiation on the collision is largely to reduce the center-of-mass energy and to boost the Z^0 decay products in the laboratory frame. The width of the Z^0 resonance is broadened by ISR, and the peak cross-section is shifted up in energy, owing to an average energy loss of the beam. The cross-section above resonance is also enhanced over the cross-section an equal energy below resonance owing to the ease with which the excess energy may be lost due to ISR.

The corrections to the measurement of A_b due to ISR, photon exchange, and vertex corrections have been calculated using ZFITTER [51], and by Renard, Blondel, and Verzegnassi [40] using EXPOSTAR [53]. QED radiative effects account for a downward relative shift of $\sim$0.17% in A_b and the measurements in this thesis will be corrected for this.

The other bremsstrahlung contribution, final-state gluon radiation, does not affect the production of the Z^0, but only its decay. It therefore does not move the energy of the peak cross-section, but it does, however, change the width. This is because hard gluon radiation opens more final quantum states into which the Z^0 may decay and thus reduces the lifetime. But the correction is only realized for $q\overline{q}$ final states, and it thus affects the partial widths of Z^0 decay. The magnitude of the effect is given by

$$\Gamma_{Z^0 \to q\overline{q}} \to \Gamma_{Z^0 \to q\overline{q}} \left(1 + \frac{\alpha_s}{\pi}\right). \tag{1.73}$$

Measurements of R_b and A_b are fortunately insensitive to this shift in the overall scale of the cross-section induced by hard gluon radiation, due to cancelation in the numerators and denominators of the measurements. Final-state radiation has an additional effect on the observed distributions, though — it smears the quark axis in the detector. Because asymmetry measurements rely on knowing the decay axis of the Z^0, final-state radiation may modify the measured asymmetry by rescattering quarks from one polar angle to another. These corrections have been calculated to second order for the case of A^b_{FB} [54][55], and the same corrections apply to the polarized forward-backward asymmetry [56]. Other calculations of the dependence of this correction on polar angle and on m_b are given in References [58] and [57].

1.5.2 Vertex and Propagator Corrections

The discussion of bremsstrahlung above would be incomplete without vertex corrections in QED and QCD, owing to the fact that the diagrams of Figure 1.5 have an infrared divergence and lack gauge invariance. The contributions from the diagrams of Figure 1.7 complete the leading-order picture of bremsstrahlung, although they are vertex corrections. Other vertex corrections due to new physics will be dealt with in Section 1.6.

Hard vacuum polarization corrections in the propagator modify the structure of the reaction $e^+e^- \to f\overline{f}$. These are shown schematically in Figure 1.8. The first and third lines of Figure 1.8 are simply self-energy renormalizations of the γ and Z^0 propagators, although they affect the relative strengths of their contributions and their interference term. The first set of corrections causes the electromagnetic coupling α to run with energy [59]. The second line of Figure 1.8 alters the helicity structure of the interaction, because the Zff coupling violates parity while the γff coupling does not. It is these diagrams that lend the measurements of A_e via A_{LR} and

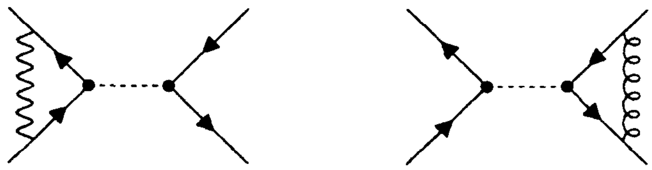

Figure 1.7: Leading order QED and QCD vertex corrections.

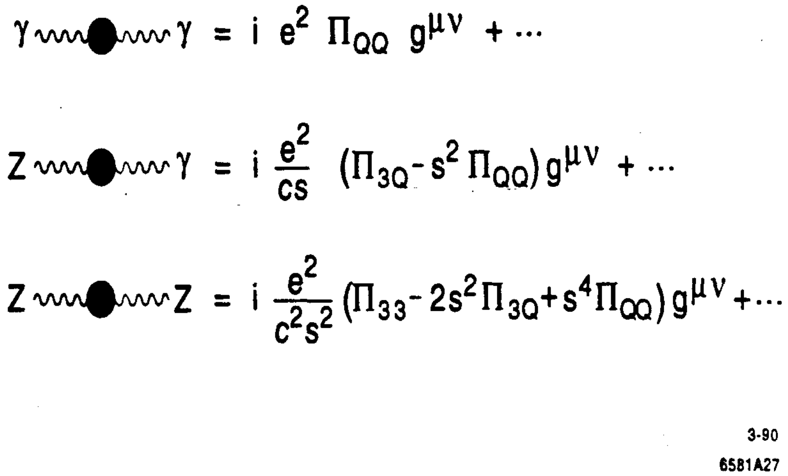

Figure 1.8: Propagator corrections to the electroweak neutral current. Here, $s^2 \equiv \sin^2\theta_W$, and $c^2 \equiv \cos^2\theta_W$.

other asymmetries their interest, because the propagator loops may contain t quarks or Higgs particles. The effect of oblique corrections is mostly to modify $\sin^2\theta_W$, although Peskin and Takeuchi have parameterized their possible effects in a model independent manner using three independent variables S, T, and U [60],[61]. The b quark couples much less strongly to the photon, and so A_b is less sensitive to the propagator corrections than A_e or A_c.

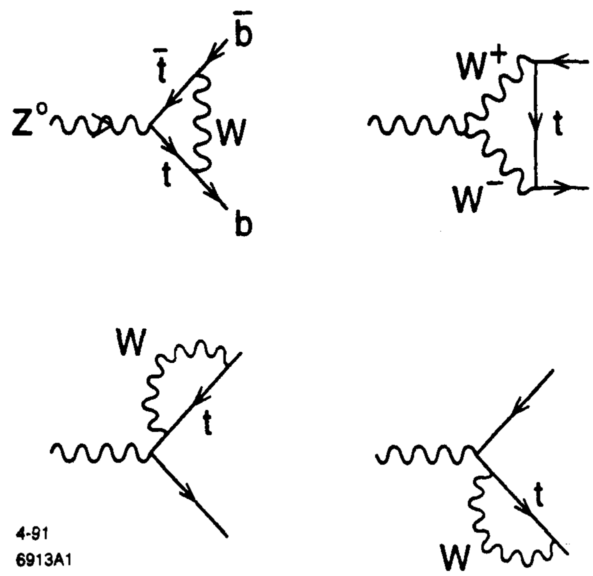

Figure 1.9: Vertex corrections to $Z^0 \rightarrow b\bar{b}$ within the Standard Model

1.6 Sensitivity of A_b to New Phenomena

The two observables R_b and A_b are enough to determine fully the couplings of the b quark to the Z^0. There are two parameters in the $Z^0 \rightarrow b\bar{b}$ coupling in the Standard Model; v_b and a_b, or alternatively $\sigma_L(b)$ and $\sigma_R(b)$, or a strength and an asymmetry. To measure both R_b and A_b is to define the Zbb vertex and measure corrections to it.

The observable A_b is quite remarkable in that it is insensitive to the collision energy, mostly insensitive to $\sin^2\theta_W$, and experimentally a very clean number to measure. The Standard Model has a prediction of its value that is very rigid with respect to variations of the model parameters. In particular, A_b is insensitive to standard one-loop vertex corrections, shown in Figure 1.9. The reason for this insensitivity is that the $W^\pm$ couples exclusively to left-handed fermions, and so the corrections affect only the left-handed coupling of the b to the Z^0. The sensitivity in A_b, though, is to the right-handed coupling, as small changes to the left-handed coupling are diluted by the large value of the left-handed coupling. It is for these reasons that A_b is an ideal probe of physics beyond the Standard Model, because it is only such new physics that can cause deviations from its expected value.

1.6.1 Additional Z Bosons

Several models involving extended gauge groups propose the existence of additional Z bosons. The effect of such a Z' on the value of A_b could be profound, if the energy of the interaction were tuned to the Z' resonance, and the Z' coupled strongly to both the initial state e^+e^- and to the $b\bar{b}$ final state.

For the same reason that the $\gamma - Z^0$ interference vanishes on the Z^0 pole for this asymmetry, (see Equations 1.50 and 1.51), the effect of an interference term with a Z' also vanishes on the Z^0 pole at tree level. Experiments far from the poles of resonances are more sensitive to Z' interactions. However, if the Z' mixed with the Z^0 at the one-loop level, it may have a visible effect on the Z^0 resonance via a propagator correction. This would have a different effect on $\sin^2\theta_W$ for the b quark than it would for the electron, and a measurement of both A_e and A_b would be valuable in disentangling it.

1.6.2 Minimal Supersymmetric Model

The Minimal Supersymmetric Model (MSSM) is an extension to the Minimal Standard Model with "superpartners" for each observed particle. The superpartner of each Fermion is a Boson, and vice versa. In the MSSM, two separate Higgs doublets are required, in order to give masses to the top and bottom quarks. Corrections to both R_b and A_b have been calculated in the MSSM by Boulware and Finnell [62]. They have noted that A_b receives negligible corrections from the supersymmetric sector unless the Higgs doublets have very different vacuum expectation values. If v_1 and v_2 are the vacuum expectation values of the two Higgs doublets, and

$$\tan\beta \equiv v_2/v_1, \tag{1.74}$$

then the bottom Yukawa coupling constant $\lambda_b \propto m_b/\cos\beta \simeq m_b \tan\beta$ becomes large in the large $\tan\beta$ limit. Supersymmetric contributions from loops with charginos, shown in Figure 1.10, which have right-handed components proportional to λ_b, become significant.

In addition, loops containing neutralinos, neutral gauginos, and Higgsinos have

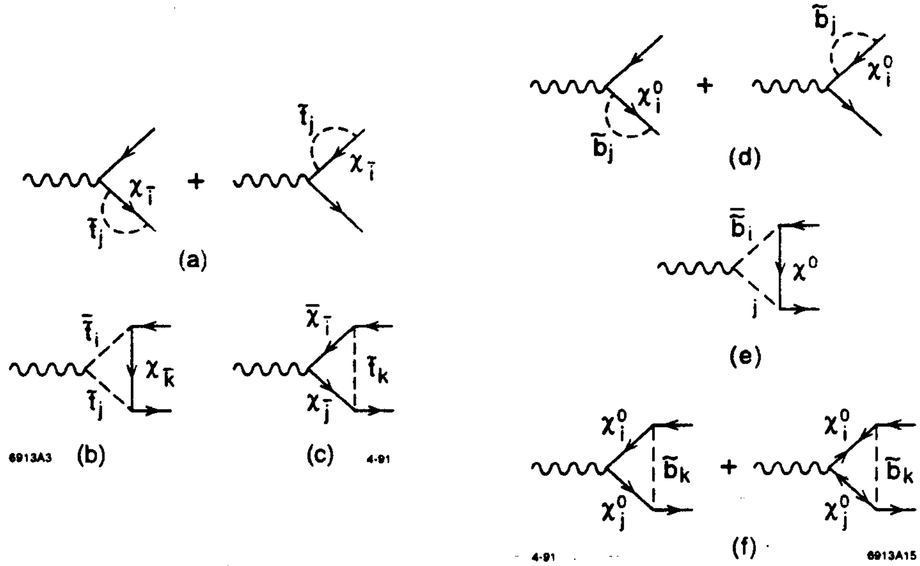

Figure 1.10: Chargino diagrams (a–c) and neutralino diagrams (d–f) contributing to $Z^0 \rightarrow b\bar{b}$ in the Minimal Supersymmetric Model.

left-handed and right-handed couplings to the b proportional to λ_b: the relevant diagrams are shown in Figure 1.10. Two additional parameters of the MSSM are relevant as the corrections to A_b depend strongly on their values. These are the coupling μ between the two Higgs fields and a supersymmetry breaking Wino mass parameter M. The corrections to A_b are shown in Figure 1.11 as functions of these two variables. These corrections have been calculated at $\tan\beta = 70$, and scale proportionally with $\tan^2\beta$.

1.6.3 Anomalous Couplings

Recently, T. Rizzo [63] has parameterized the effects of anomalous electric and magnetic dipole moment couplings between the b quark and the Z^0. An electric dipole moment of the b quark would violate CP symmetry. While this experiment does not observe a CP-violating asymmetry, nonetheless it is able to put limits on the electric dipole moment of the b quark.

Two additional parameters are added to the Standard Model Lagrangian, κ and $\tilde{\kappa}$, which are the real parts of the magnetic and electric dipole form factors evaluated

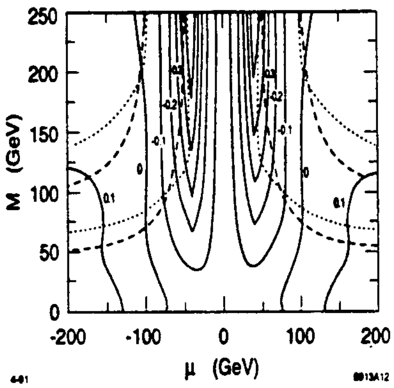

Figure 1.11: Contours showing 100 times the contribution to A_b from neutralinos, for $\tan\beta$=70. From Boulware and Finnell [62].

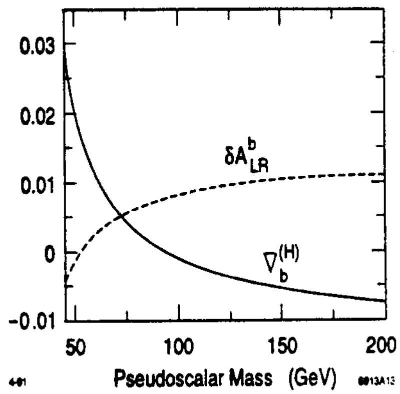

Figure 1.12: Corrections to R_b and A_b from charged and neutral scalars for $\tan\beta = 70$. From Boulware and Finnell [62].

at $q^2 = M_z^2$. The Lagrangian expressing the interaction of a fermion f to the Z^0 gains an additional term containing these

$$\mathcal{L}_{int} = \frac{g}{2\cos\theta_W}\overline{f}\left[\gamma_\mu(v_f - a_f\gamma_5) + \frac{i}{2m_f}\sigma_{\mu\nu}q^\nu(\kappa_f - i\tilde{\kappa}_f\gamma_5)\right] f Z^\mu, \tag{1.75}$$

where g is the weak coupling constant, m_f is the mass of the final-state fermion. and q is the four-momentum of the Z^0. The polarized differential cross-section can then be derived in the limit that $m_f \ll m_Z$.

$$\frac{d\sigma}{d\cos\theta} \propto (1 - A_e P_e)\left[1 + \cos^2\theta + 2(A_e - P_e)\left(A_f + \frac{2\kappa_f a_f}{v_f^2 + a_f^2}\right)\cos\theta + \right.$$
$$\left. \frac{1}{v_f^2 + a_f^2}\left(\frac{m_Z^2}{4m_f^2}(\kappa_f^2 + \tilde{\kappa}_f^2) sin^2\theta + \kappa_f^2 + \tilde{\kappa}_f^2 + 4v_f\kappa_f\right)\right], \tag{1.76}$$

which can be compared with Equation 1.61. The modified value of A_b measured by the left-right forward-backward asymmetry is then

$$A_b = \frac{2(v_f a_f + \kappa_f a_f)}{v_f^2 + a_f^2 + \frac{3}{4}\left(\frac{m_Z^2}{4m_f^2}(\kappa_f^2 + \tilde{\kappa}_f^2) + \kappa_f^2 - \tilde{\kappa}_f^2 + 4v_f\kappa_f\right)}. \tag{1.77}$$

Chapter 2

Current Experimental State

There is an intense worldwide program to investigate the parity-violating couplings of fermions to the Z^0. Information about the asymmetry of the b quark coupling has been obtained at the four LEP experiments at CERN. The LEP accelerator has unpolarized electron and positron beams, so the measurable asymmetry A_{FB}^b is proportional to the product of the electron coupling asymmetry and the b coupling asymmetry. This chapter presents extractions of A_b from the LEP measurements, using an average A_e derived from LEP and SLD measurements. Other information on A_b comes from SLD itself, taking advantage of the semileptonic decays of the B hadrons.

Lower energy experiments also measure parity-violating couplings, largely by virtue of the interference between the photon and Z^0-exchange diagrams. While not direct measurements of A_b, these are provided for comparison.

2.1 Measurements of A_b With Leptons

Of the measurements using the semileptonic decay modes of B hadrons, SLD's contribution is the most direct. The left-right forward-backward asymmetry is formed in a similar fashion to the one employed in this thesis. This measurement and similar ones at LEP use hadronic events containing high momentum leptons with a large component of that momentum transverse to their respective jet axes. These measurements usually extract both A_b and A_c using a maximum-likelihood technique, where each lepton is assigned a probability of having originated at a B decay vertex, a cascade charm decay, a charm decay vertex in a $Z^0 \rightarrow c\bar{c}$ event, and also the probability the lepton was a misidentified charged hadron. The SLD measurements are described in detail in References [45], [46] and [47].

The measured values for SLD are

$$\begin{aligned} A_b &= 0.83 \pm 0.12\ (\text{stat.}) \pm 0.07\ (\text{syst.}) & &\text{muons} \\ A_b &= 0.87 \pm 0.12\ (\text{stat.}) \pm 0.10\ (\text{syst.}) & &\text{electrons} \\ A_b &= 0.85 \pm 0.09\ (\text{stat.}) \pm 0.08\ (\text{syst.}) & &\text{combined.} \end{aligned} \tag{2.1}$$

and

$$\begin{aligned} A_c &= 0.43 \pm 0.15\ (\text{stat.}) \pm 0.12\ (\text{syst.}) & &\text{muons} \\ A_c &= 0.46 \pm 0.20\ (\text{stat.}) \pm 0.18\ (\text{syst.}) & &\text{electrons} \\ A_c &= 0.44 \pm 0.12\ (\text{stat.}) \pm 0.14\ (\text{syst.}) & &\text{combined.} \end{aligned} \tag{2.2}$$

The current measurements from the four LEP experiments of A^b_{FB} using semileptonic B decays are given in Table 2.2. The LEP experiments do not correct separately for gluon radiation, photon radiation, γ-Z^0 interference, or the γ-exchange contributions. Instead, they report raw asymmetry values at the LEP ring energy, which are averaged and then corrected for those effects to arrive at an average A^0_{FB}. In order to extract a per-experiment measurement of A_b, then, one must apply these corrections and also divide by $\frac{3}{4}A_e$.

The A_e to be used must be chosen judiciously. As described in Chapter 1, the lepton forward-backward asymmetries, the tau polarization asymmetry, A_{LR}, and the quark forward-backward asymmetries all are sensitive to $\sin^2\theta_W$. It is common to form an average $\sin^2\theta_W$ with the assumption that the Minimal Standard Model holds, and then to extract a prediction of A_e. To use this A_e to extract A_b from A^b_{FB} would be circular, in that A^b_{FB} is one of the most important contributions to the determination of $\sin^2\theta_W$ and therefore of A_e, and its inclusion in the fit assumes A_b takes its standard value.

The prescription is to average the A_e values only from purely leptonic measurements — SLD's A_{LR}, the forward-backward lepton asymmetries from LEP (assuming

Table 2.1: Current leptonic measurements of A_e used to extract A_b from A_{FB}^b. From Reference [64].

Measurement	A_e
SLD A_{LR}	0.1551 ± 0.0040
LEP A_{FB}^l	0.1514 ± 0.0053
LEP P_τ	0.1406 ± 0.0057
Average	0.1506 ± 0.0028

Table 2.2: Measurements from the four LEP experiments of A_{FB}^b from semileptonic B decays, given in Reference [65], uncorrected for QCD, QED, and $\gamma - Z$ interference. The values of A_b are extracted using the value of A_e from Table 2.1, and are also corrected for radiative effects and photon exchange.

Experiment	Data Sample	A_{FB}^b	A_b
ALEPH	1990–1993	$0.0846 \pm 0.0068 \pm 0.0022$	0.800 ± 0.065
DELPHI	1991–1994	$0.1049 \pm 0.0076 \pm 0.0035$	0.980 ± 0.077
L3	1990–1993	$0.103 \pm 0.010 \pm 0.004$	0.963 ± 0.097
OPAL	1990–1994	$0.1030 \pm 0.0090 \pm 0.0040$	0.963 ± 0.089

lepton universality), and A_e from the tau polarization asymmetry. These are shown in Table 2.1, using data from Reference [64].

2.2 Measurements of A_b With Momentum-Weighted Charge

The second technique of measuring A_b at the Z^0 also involves forming the forward-backward asymmetry and dividing by $\frac{3}{4}A_e$, but the asymmetry is found using momentum-weighted track charge to distinguish the b direction from the $\bar{b}$ direction. The

Table 2.3: Measurements from three of the four LEP experiments of A^b_{FB} using momentum-weighted charge in lifetime-tagged $Z^0 \to b\bar{b}$ samples, as reported at the 1995 Europhysics Conference [65]. The values of A_b extracted assume $A_e = 0.1506 \pm 0.0028$.

Experiment	Data Sample	A^b_{FB}	A_b
ALEPH	1991–93	$0.0992 \pm 0.0084 \pm 0.0046$	0.930 ± 0.087
DELPHI	1991–1994	$0.0999 \pm 0.0072 \pm 0.0038$	0.936 ± 0.074
OPAL	1991–1994	$0.0963 \pm 0.0067 \pm 0.0038$	0.904 ± 0.071

sample of $Z^0 \to b\bar{b}$ decays is identified with the aid of precision silicon microvertex detectors. The details of the SLD approach to this technique are presented in Chapters 6 and 7.

Because of systematic errors inherent in using Monte Carlo simulations to determine the effectiveness of the momentum-weighted track charge technique, the three LEP experiments that contribute these measurements use distributions from data to calibrate the technique. Two of the LEP experiments, ALEPH and OPAL, follow a prescription similar to, but less sophisticated than, the one presented in Chapter 7. The differences are that the SLD technique takes into account the $\cos\theta$ dependence of the asymmetry and the correct-sign probability, as well as parameterizing the correct-sign probability as a function of the momentum-weighted charge. The SLD technique also accounts for the QCD correction in a $\cos\theta$-dependent manner, while the OPAL technique [66] applies an overall correction, and the ALEPH technique [67] ignores it altogether. The measurement from DELPHI [68] takes a different approach by tagging a high-$(p, p_\perp)$ lepton in one hemisphere and examining the momentum-weighted charge in the opposite hemisphere. This distribution is then used in the inclusive lifetime-tagged sample to measure A^b_{FB}.

2.3 Combined LEP A_b

The combined value of $A^{0,b}_{FB}$, corrected for radiation and γ-exchange and reported at the 1995 Europhysics Conference [65] is 0.0997 ± 0.0031, resulting in an inferred A_b

Table 2.4: Measurements of A^b_{FB} at $\sqrt{s} = 57.8$ GeV from the three TRISTAN experiments. Correction for B meson mixing is not included in these measurements, but would enlarge the values by a factor of ~1.3 if it were.

Experiment	A^b_{FB}	Reference
AMY	$-0.59 \pm 0.09 \pm 0.09$	[69]
VENUS	$-0.55 \pm 0.15 \pm 0.08$	[70]
TOPAZ	$-0.55 \pm 0.27 \pm 0.07$	[71]

of 0.883 ± 0.032. This value can be compared with the Standard Model prediction of 0.935. The measurement presented in this thesis compares favorably with individual measurements from the four LEP experiments, although the total error on the combined value is much less than that on any one contribution.

2.4 A^b_{FB} at Other Energies

A compilation of measurements of A^b_{FB} at energies up to the Z^0 pole energy can be found in Reference [69]. The energy dependence of A_{FB} follows the general behavior that is expected from the Standard Model predictions, outlined in Chapter 1. The value of A_{FB}, as measured off the Z^0 pole, is not strictly proportional to A_b, due to the presence of parity violation in both the direct Z^0 exchange term and the interference term, and the lack of it in the photon exchange term.

The measurements of A^b_{FB}, as measured at $\sqrt{s} = 57.8$ GeV at TRISTAN, are given in Table 2.4. They are also are displayed with the Standard Model predictions. and data from PEP, PETRA, and LEP, in Figure 2.1. These measurements were made with the high-$(p, p_\perp)$ lepton technique.

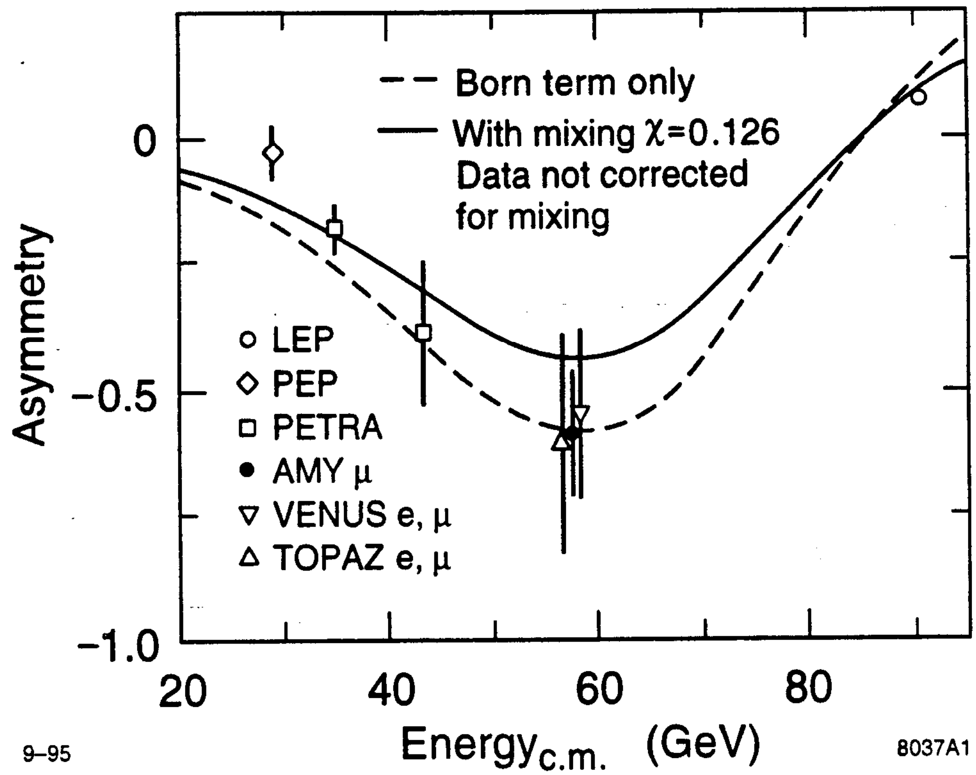

Figure 2.1: Measurements of A_{FB}^{b} as a function of E_{CM}, measured at PEP, PETRA, TRISTAN, and LEP, as compiled in Reference [69]. The data are uncorrected for B meson mixing, and can be compared with the model incorporating mixing (solid line).

Chapter 3

Experimental Apparatus: SLC and the Compton Polarimeter

To perform a measurement of A_b on the Z^0 resonance, the initial quantum state of the e^+ and e^- must be carefully prepared and characterized. The SLAC Linear Collider (SLC), comprised of a polarized electron gun, a linear accelerator, a positron source, damping rings, collider arcs, and final focus optics has been commissioned and has been operating since 1989 producing Z^0 bosons. To measure the properties of the beam, the SLC itself has diagnostic tools at every stage, but the most important physical quantities must be measured as close to the detector as possible. The relevant beam parameters are energy, energy spread, luminosity, and polarization.

3.1 The SLAC Linear Collider

The need to accelerate an electron beam and a positron beam to an energy sufficient to collide them at the Z^0 resonance, and the need to focus them tightly enough to produce enough luminosity to carry out sensitive studies of the electroweak interaction, together govern the design of the SLC [72]. Several innovations in accelerator technology were crucial in making SLC a successful machine for particle physics studies. SLC is the first e^+e^- linear collider, and at the moment shares with LEP the distinction of being the highest energy e^+e^- accelerator yet built.

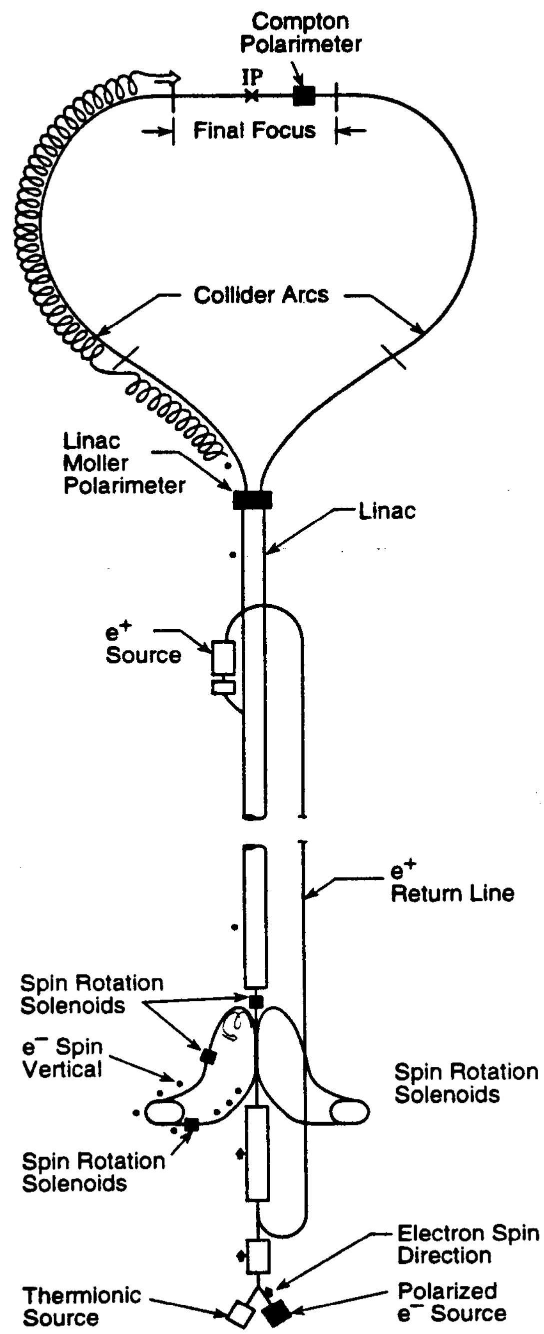

Figure 3.1: Layout of the spin-polarized SLC, showing the beam transport lines and polarization orientation.

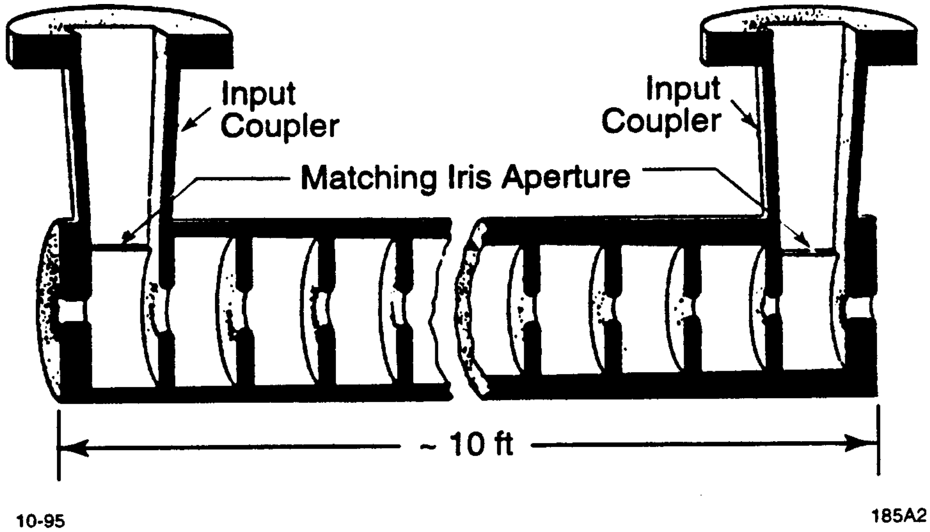

Figure 3.2: A 10-foot longitudinal section of the disk-loaded waveguide accelerator structure. The longitudinal period of the structure is 1.378 inches, with a disk thickness of 0.230 inches, so the phase shift in the RF per cavity is $2\pi/3$. The cavity diameter varies from 3.286 inches in the first cavity to 3.220 inches the last. The diameter of the aperture in the disks varies from 1.032 inches in the first cavity to 0.752 inch in the last. The taper in the dimensions is required to maintain a constant gradient across the section, after accounting for attenuation and beam loading. From Reference [74].

The electron beam starts at an electron gun containing a strained-lattice gallium-arsenide cathode, which photoemits longitudinally polarized electrons when illuminated by circularly polarized laser light [73]. The details of polarized beam production and transport will be given in Section 3.4.

The accelerator consists of two miles of copper disk-loaded waveguide, shown in Figure 3.2. The resonant structure of the accelerator pipe allows a standing wave to exist with a component of the electric field along the direction of the beam. If electrons are introduced at the appropriate phase of the oscillating field, they will receive an acceleration along the beam tube. Positrons injected on the opposite phase can be accelerated in the same direction to the same energy.

The microwave energy for the accelerator is supplied by pulsed 38 MW, 2.856 GHz klystrons. Each second, the klystrons produce 120 pulses of RF 5.0μs long. The RF pulses are nearly doubled in power by the SLED-II cavities [75]*, which shorten the effective pulse duration to 800 ns while increasing the amplitude. With the SLED-II cavities operating, the electron beam receives ~14.5 MV of energy for every meter of accelerator structure traversed.

Both electrons and positrons must accelerate down the tube on the same pulse. To accomplish this, the electron gun produces two bunches of electrons in quick succession. Both bunches are accelerated to 1.19 GeV in the first section of the accelerator and are shunted into the North Damping Ring (NDR), where they remain until the next RF pulse from the klystrons. The South Damping Ring (SDR) is built to damp positrons made on the previous machine cycle.

The damping rings enable SLC to focus its beams tightly. The electron beam emerges from the gun with a large width and a large angular divergence. Liouville's theorem demands that the total volume of a bunch in position/momentum phase space be conserved by a non-dissipative accelerator. The damping rings introduce a dissipative element — synchrotron radiation — to reduce the phase space volume of the bunches. Short accelerating sections in the rings compensate for radiative losses, and the electrons settle into a stable orbits determined by the damping ring parameters, having lost all knowledge of their prior trajectories before entering the ring. The bunches shorten and reduce their angular divergence in the rings.

It is in the damping rings that the beams are made flat. In the absence of coupling between oscillations in the two transverse directions, the stable orbits of a horizontal ring occupy a region of space that is larger in the horizontal direction than the vertical. SLC typically runs an aspect ratio at the interaction point of 4.6:1 [78].

The damping rings were upgraded between the 1993 and 1994–1995 runs [79]. The main upgrade was to redesign the vacuum chamber to reduce the impedance. This improvement delays the onset of bunch-lengthening instabilities as the bunch population is increased, allowing higher luminosity.

On the next pulse of RF from the klystrons, both bunches of electrons from the NDR and a bunch of positrons from the SDR are extracted and accelerated in the linac. The positron bunch leads the two electron bunches in the linac. The

* "SLED" stands for SLAC Energy Doubler.

Table 3.1: Parameters of the SLC damping rings [76][77].

Energy	1.19 GeV
Circumference	35.270 m
Revolution Frequency	8500.411 kHz
RF Frequency	714.000 MHz
Bending Radius	2.0372 m
Energy Loss/turn	93 KeV
Damping Time τ_x	3.32±0.28 ms (e^-)
	3.60±0.15 ms (e^+)
Damping Time τ_y	4.11±0.31 ms (e^-)
	4.17±0.14 ms (e^+)

trailing bunch of electrons, called the "scavenger bunch," is sent to the positron source, roughly 1.33 miles down the accelerator. After receiving 31 GeV of energy, this bunch strikes a tungsten target, producing an electromagnetic shower. A pulsed solenoid focuses the produced positrons so they may be accepted by a short booster which accelerates them to 200 MeV. The positrons are then guided back through the positron return line to the injector, accelerated to 1.19 GeV, and steered into the SDR, to provide the positrons for the next machine cycle.

The other two bunches extracted from the damping rings, one each of electrons and positrons, are the luminosity-producing bunches. The short bunch length produced by the damping rings is crucial in reducing the energy spread — a long bunch will sample a larger portion of the accelerating wave, increasing the magnitude of longitudinal oscillations about equilibrium. A technique termed "overcompression," introduced for the 1994–1995 run [80], shortens the bunches further in the transfer line between the damping rings and the accelerator, reducing the energy spread.

A lattice of quadrupole magnets interleaved with the accelerating sections keeps the beam focused within the accelerating field given its finite angular divergence.

Within each quadrupole magnet, a beam position monitor (BPM) provides information for feedback control [81] of accelerator parameters such magnet strengths and klystron phase, as well as providing information for online diagnostics. Each BPM also produces a measurement of the beam current.

The beams gain energy from the 1.19 GeV of the damping rings to 46.6 GeV by the time they reach the Beam Switchyard (BSY).

The BSY contains dipole magnets which direct the electrons into the North SLC arc (NARC), and the positrons into the South arc (SARC). The arcs contain a lattice of dipole and quadrupole magnets to keep the beams focused while steering them into collision. The arc tunnels were dug following the local terrain and passing underneath the PEP tunnel. The configuration of magnets needed to guide the beams through the arcs has important consequences on the transport of the electron spin, to be discussed in Section 3.4.5

Collimators at the end of the LINAC and at different places in the arcs remove portions of the bunch that have the wrong energy or have strayed too far from the bunch core. Synchrotron radiation losses in the arcs amount to ~1 GeV per electron.

The last section of beampipe before the interaction point (IP) is nearly straight. in order to reduce the beam-related backgrounds in the detector. These straight sections contain magnets designed to bring the beams into focused spots at the IP. Superconducting quadrupoles form the final triplets in order to provide a higher field strength than conventional iron-yoke magnets, and allow operation within the SLD solenoidal field [82].

The final focus optics were upgraded for the 1994-1995 run in order to reduce the chromatic effects on the focal length of the system [83].

A Compton polarimeter, to be described in Section 3.5, continuously measures the electron beam polarization in the South Final Focus (SFF). Energy spectrometers, to be described in Section 3.5.3, measure the energy of the two beams.

Constant feedback keeps the beams in collision at the IP in the face of thermal motion and upstream adjustments. Additionally, every five minutes, horizontal and vertical scans of one beam across the other are made to determine the transverse beam dimensions. The deflection of one beam from the other is measured by BPM's downstream of the IP on each pulse of the scan, and fits are performed to deconvolute the dimensions of the two beams. The slope of the deflection as a function of corrector strength is used to tune the feedback system.

Another detector, the radiative Bhabha counter, detects electrons that have lost a portion of their energy by scattering off of the particles in the other bunch. These lower-energy electrons are overbent in the first bending magnet of the final focus, and are steered into this detector. It provides a fast estimate of beam luminosity for accelerator tuning purposes, although backgrounds preclude its use for precision luminosity measurements.

A Møller polarimeter was installed briefly in the electron extraction line at the end of the 1993 run to cross-check the polarization measured by the Compton polarimeter. Its installation precludes the use of the energy spectrometer and the positron beam, so it can only be used as a check. It has larger systematic errors than the Compton polarimeter and will not be used in this analysis. Another Møller polarimeter, situated in the beam switchyard, can be used more easily — no hardware needs to be moved to switch between physics running and Møller measurements — although it lies on the other side of the NARC, which can precess the electron spin in an arbitrary direction, and also partially depolarize the beam.

3.2 Performance

SLC has constantly improved its luminosity since it started producing Z^0 bosons in 1989, by a combination of shrinking the beam waists at the collision point, increasing the electron and positron bunch populations, and increasing the reliability of operation. This reliability factor includes not only the fraction of the time the accelerator is on and delivering bunches to the IP, but also the the fraction of the time it is optimally tuned. Feedback mechanisms have greatly reduced the need to dedicate time to tuning the beams [81]. In addition, reduced deadtime from SLD increased the effective luminosity. This was achieved by pipelining the data acquisition, suppressing readout on beam crossings for which the detector was saturated with noise, buffering the logging stream, and streamlining the run switchover procedure. During

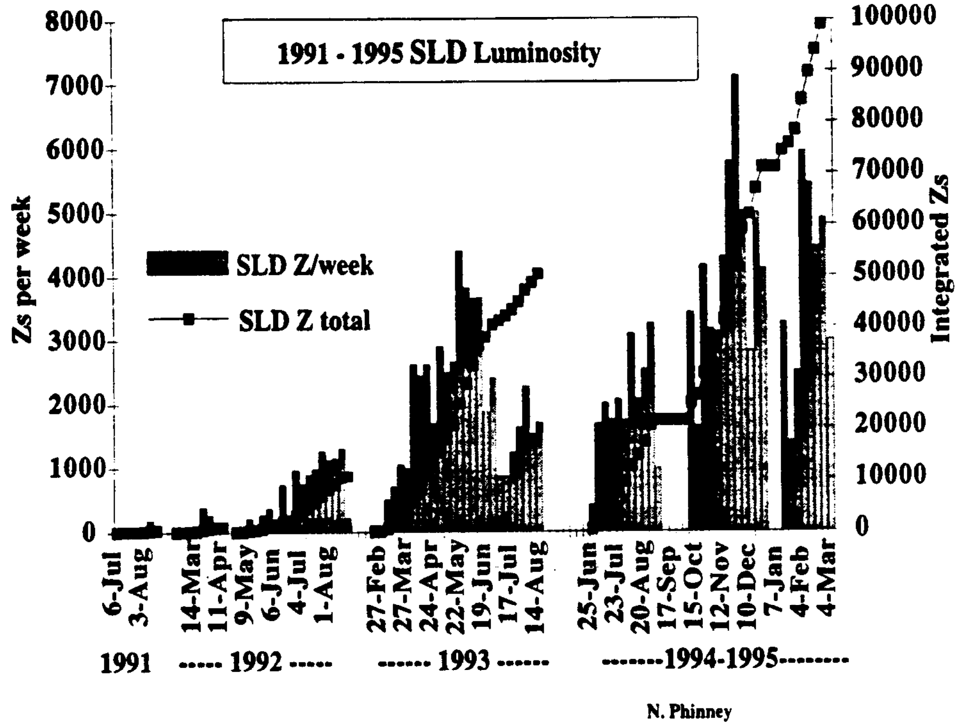

Figure 3.3: Integrated and differential luminosity histories of the SLC.

the 1994–1995 run, typical luminosities achieved were 50–60 Z^0/hour, while in 1992, 30 Z^0/hour was more common. A history of the SLC luminosity for the time SLD was running is given in Figure 3.3.

The polarization plays a crucial role in the ability of SLD to measure asymmetries, as the error on A_b and A_{LR} scales inversely with $P_e\sqrt{\mathcal{L}}$. A bulk GaAs photocathode provided the electron source in 1992, with a realized polarization of 22%. For 1993, a strained GaAs crystal was installed, and in 1994, a thinner strained GaAs crystal took its place. The history of the polarization as a function of the count of collected Z^0 bosons is shown in Figure 3.4

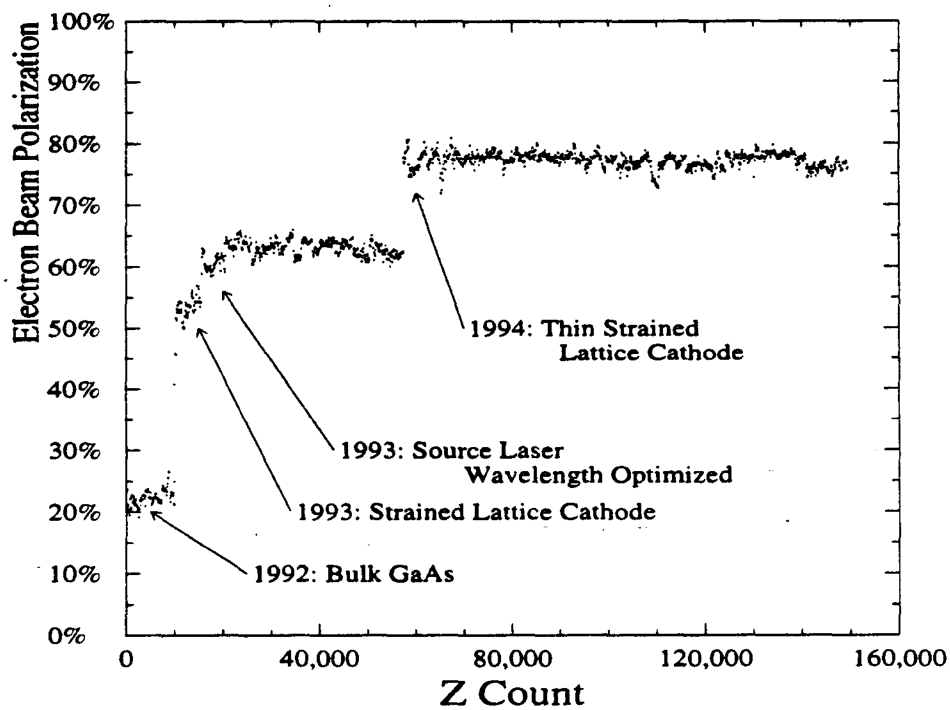

Figure 3.4: History of the electron beam polarization as a function of the count of collected Z^0s. Large discontinuities correspond to cathode changes for the different running years.

3.3 Linear Colliders and Synchrotrons

The competing experiments at the Z^0 are at CERN on the LEP ring, a synchrotron 26.66 km in circumference with four interaction halls. This device has several advantages over the linear collider at SLAC, and several shortcomings. The colliding-beam synchrotron has had a long history as a successful accelerator design since its introduction with the ADONE ring in Italy and the construction of the SPEAR ring at SLAC. The SPEAR ring is small (234 meters in circumference) and operates each beam at energies up to 3.5 GeV. The physical phenomenon that dominates the design of these accelerators is energy loss through synchrotron radiation, which dissipates the beam's energy at a rate of

$$\Delta E \simeq \frac{6 \times 10^{-18}}{r} \left(\frac{E_{beam}}{mc^2}\right)^4 \text{ GeV/Turn}, \tag{3.1}$$

where r is the bending radius of curvature of the ring, measured in meters, and m is the mass of the accelerated particles. This energy must be replenished constantly by RF cavities. Assuming constant unit prices for land, tunnels, accelerator components, and electrical power, the optimal size of a synchrotron must increase in proportion to the beam energy squared. The circumference of LEP verifies this relation.

The accelerating portion of a linear collider, on the other hand, dissipates energy to synchrotron radiation only in proportion to the energy to the first power. Furthermore, the accelerator energy is proportional to its length, so all costs scale with energy to the first power. The required bend strength for the SLC arcs is modest†. At the Z^0 resonance and above, linear colliders are smaller and less expensive than synchrotrons of the same energy.

The rate at which new pulses are injected into the SLC is limited to 120 Hz for two reasons. The first is that the power consumption of the linac scales with the repetition rate as the accelerator structure is re-filled with RF on every pulse. The second is that the pulses require an ~8 ms damping time in the damping rings. and placing more bunches in the damping rings has been shown to introduce bunch-lengthening instabilities [85]. This contrasts with the 90 KHz bunch-crossing rate at LEP, assuming eight bunches for each beam are stored in the ring simultaneously.

What SLC loses in bunch-crossing frequency it must make up for in beam spot size to produce enough collisions for physics analysis. Current performance of the LEP accelerator's spot sizes is 10 μm vertically by 150 μm horizontally. SLC has a spot size of 0.5 μm by 2.3 μm.

The small spot size of SLC also allows for higher precision measurements of decay lengths near the IP. When the beams are large, the point of decay of the Z^0 must be measured on each event, subject to detector resolution. Owing to the fact that all of the charged decay products in many events travel in paths nearly parallel to the thrust axis, information about the location of primary vertex along that axis may be very poor. With spots that are small in two dimensions, the primary vertex measurements of many events may be found and averaged [86], providing excellent knowledge of

†The size of the SLC arcs was determined by the need to keep the emittance growth due to synchrotron radiation down, while fitting on SLAC property.

the location of the Z^0 decay on each event. Care must be taken to average events only over times when the beam did not move significantly. The beam motion is usually very small at SLC — large jumps are infrequent and have identifiable causes. Knowledge of the beam position for each event allows determination of the impact parameters of tracks relative to the beams with high accuracy, a necessary ingredient for the analysis presented in this thesis.

The most significant advantage SLC has over LEP for electroweak asymmetry measurements is its ability to polarize its electron beam, to be described in the next section. The positron beam can not be polarized readily because it is produced by an electromagnetic shower in a tungsten target. Furthermore, the positron transport system is not designed to preserve any polarization of the positron beam. The Sokolov-Ternov polarization buildup time [87] in the positron damping ring is ~960 s, while the positrons only spend 16.7 ms in the ring.

Backgrounds from stray particles tend to be different at linear colliders and synchrotrons. Each sensitive component near the interaction region is susceptible to particular types of backgrounds and not to others. For example, the tracking chambers are sensitive to the presence of synchrotron radiation produced in the final focus optics because high-energy photons scatter on the atomic electrons in the beampipe and detector material. Some electrons are freed with enough energy to travel through the tracking volume and leave an ionization trail. Because their energy is typically very low, the tracks left by these particles are small helices that stay close to the point at which the electron was liberated, predominantly in the inner layers of the chamber. If enough of these electrons are liberated each beam crossing, the chamber will not be able to hold its design voltage. The linear collider design increases the presence of synchrotron radiation near the experiment by demanding that the focusing of the last set of magnets be very strong, in order to reduce the beam widths. This background is present also in synchrotrons, and its magnitude is proportional to the beam current, but the focusing angles are smaller.

Another background found at both types of machines is the presence of muons traveling roughly parallel to the beam. These are produced by the Bethe-Heitler mechanism [88] when an electron passes close to a nucleus in some material far upstream from the detector. These muons penetrate the material of the beamline optics, tunnel walls, shielding blocks, and pass through the detector's calorimeter. This background is controlled by minimizing the population of the wide tails of the bunches as they pass by apertures in the beam transport system. Early collimation in the accelerator, as well as control of the energy spread and bunch-to-bunch position and energy jitter help to reduce this background, and it is much less prevalent since SLC first began operation. At a synchrotron, one needs to maintain a large aperture in regions of high dispersion, but the beam tails are clipped soon after injection.

In response to the different operating environment of a linear collider, techniques were developed to optimize the luminosity and reduce accelerator backgrounds. Feedback mechanisms were installed along the accelerator, in the damping rings, in the arcs, and in the final focus region. The SLD detector forms a summary of the signal in each of its major sensitive systems on each pulse of the accelerator and sends this information to the accelerator control center in a useful display on a storage oscilloscope. This allows the accelerator operators to see immediately the impact of every action they take to reduce the backgrounds in the detector, and background reduction has become a routine task that can be performed rapidly and effectively. During the 1993 run, approximately 0.3 muons per beam crossing passed through the calorimeter, and approximately 6% of the sensitive wires in the drift chamber registered a background pulse. The effect of these backgrounds on physics analysis is very small and will be discussed in Chapters 5 and 6.

3.4 Spin Production and Transport

3.4.1 Electron gun

The electron gun, shown in Figure 3.5, consists of a cathode of gallium arsenide on a substrate of gallium arsenide phosphide, to provide lattice strain [73]. It is held at a potential of -120 kV, while the surrounding metal structure in the electron gun

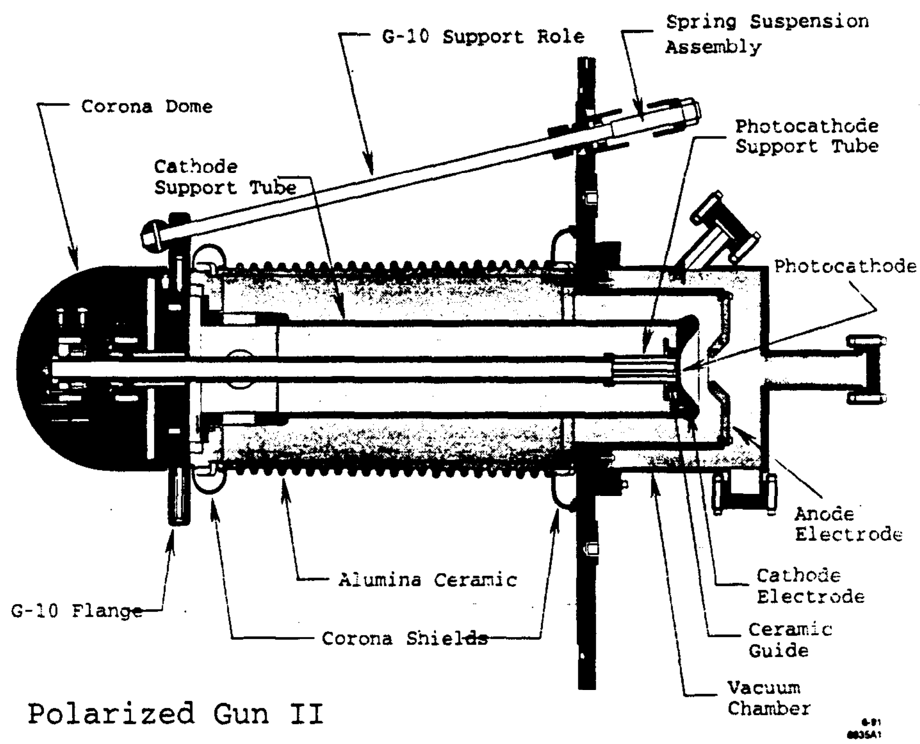

Figure 3.5: The polarized gun used on SLC in 1993. The photocathode used was a strained-lattice GaAs cathode.

nearly the full 120 kV of acceleration so they may be accepted by the first section of the accelerator. With time, the quantum efficiency of the cathode degrades. Roughly every four days during running, a thin layer of cesium, moderated with fluorine, is added to the surface of the cathode to restore optimal quantum efficiency. Every few months, the lifetime of the quantum efficiency after each addition of cesium gets shorter, and the cathode must be baked at high temperature to clean the surface of impurities.

3.4.2 Photocathode

The need to reach high electron beam polarizations drove the choice to develop thin, strained GaAs cathodes for SLC [73]. A GaAs cathode will emit polarized electrons if it is illuminated with circularly polarized light, but the magnitude of the polarization

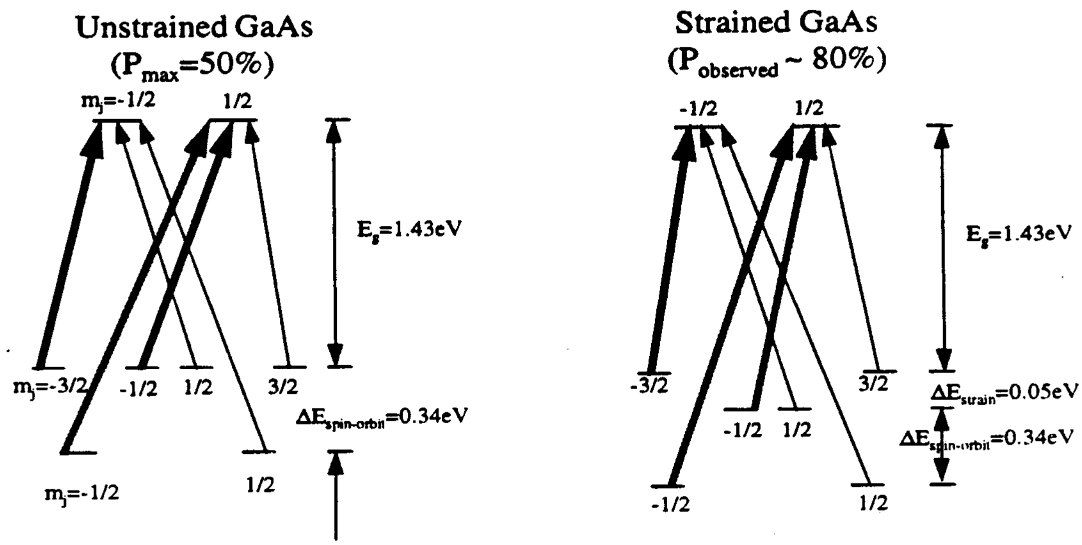

Figure 3.6: Energy levels in unstrained and strained GaAs. The dominant $\Delta L = 1$ transitions are shown in bold. The strain breaks the degeneracy between the $m_j = -3/2$ and $m_j = -1/2$ levels in this figure, suppressing transitions from the latter levels.

obtainable is determined by the energy states within the crystal, shown in Figure 3.6. The electrons which emerge from the crystal first have to be elevated from the valence band to the conduction band before they may escape the work function of the material. A bulk crystal of GaAs has an important degeneracy between the spin states in the valence band, which is brought about by the crystal symmetry. If circularly polarized light impinges upon the crystal, two transitions of equal splittings are excited. These transitions have a strength ratio of 3:1, owing to a difference in their Clebsch-Gordan coefficients. With no other bias between these two transitions, the maximum available polarization obtainable is 50%.

The energy degeneracy of the different spin states in the valence band can be lifted by breaking the crystal symmetry with a mechanical strain. Placing the GaAs in compression favors the already strong transition over the weaker one. The strain is induced by growing a thin layer of GaAs on a crystal of GaAsP, which has a slightly smaller lattice constant. Because the splitting due to the strain is only 0.05 eV while the transition energy is 1.52 eV, the additional gain in polarization is dependent on

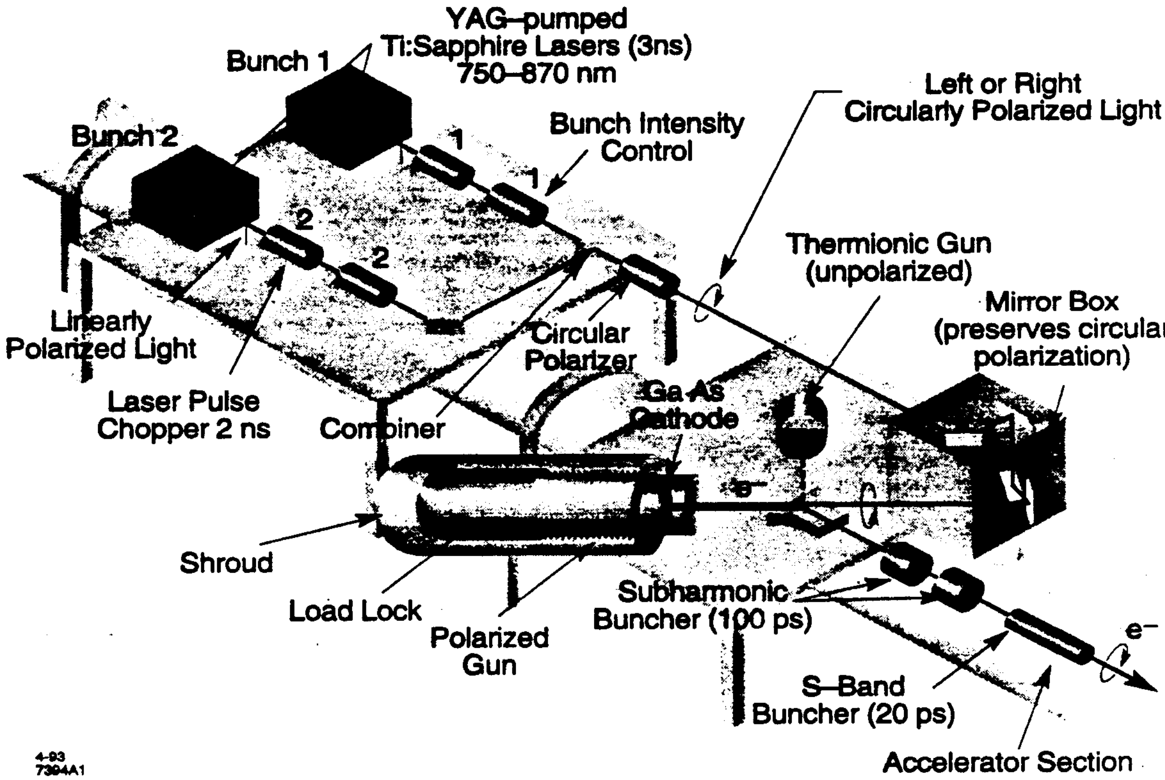

Figure 3.7: Optical layout of the polarized source.

the energy of the photons used. To optimize the polarization, photons of the lowest possible energy are used, consistent with the requirement that the quantum efficiency be high enough to extract sufficient current from the gun. The quantum efficiency can be improved by adding cesium, but also at the cost of lowering the polarization slightly.

The thickness of the strained GaAs layer strongly affects the achievable polarization because the GaAs lattice relaxes with increasing distance from the GaAsP interface [73]. The cathode used in the 1993 run had a thickness of 0.3μm and delivered a beam polarization of $\approx$63%, while the cathode used for 1994–1995 had a thickness of 0.10μm and delivered a polarization of $\approx$77%.

3.4.3 Electron source optics

This cathode emits photoelectrons when light of a wavelength shorter than ~900 nm impinges on it. Reversing the helicity of the circularly polarized light reverses the helicity of the electron beam. The pulses of light need to be short, intense, and of a controllable wavelength, so YAG-pumped Ti:Sapphire lasers are used. The light is circularly polarized by first linearly polarizing it, and then passing the beam through a Pockels cell. The sign of the voltage on the Pockels cell determines the orientation of its fast axis and slow axis. If these axes are arranged to be at 45° to the plane of polarization of the laser light, and the phase advance difference between the two axes is 90°, then the resulting light emerges circularly polarized. The sign of the voltage on the Pockels cell, and thus the helicity of the light from the apparatus, is chosen pseudo-randomly[‡] on each beam pulse in order to minimize systematic effects from periodic behavior of the accelerator.

Two 60 Hz YAG lasers pump both Ti:Sapphire cavities; their pulses are interlaced so the Ti:Sapphire cavities pulse at 120 Hz. One cavity produces the pulse for the polarized electrons, and is tuned to a frequency of 845 nm for the 1994-1995 run[§]. The other Ti:Sapphire cavity produces 765 nm pulses for the scavenger bunch. The wavelength is shorter in order to increase the cathode quantum efficiency, as the polarization is not required for the scavenger pulse.

3.4.4 Damping Ring Spin Transport

From the injector, the electron bunch passes into the North Damping Ring (NDR). To preserve the spin in the damping ring, the average electron spin must be vertical on injection. Part of the NLTR serves to precess the spin from its original longitudinal orientation to a horizontal direction perpendicular to the electron's path. A superconducting solenoid in the NLTR then precesses the spin to a vertical orientation.

[‡]The pseudo-random number generator chosen for SLC is a 33-bit feedback shift register, described in [89]. Some of its properties germane to SLC are given in [90].

[§]The operating wavelength for the bulk of the 1993 run was 865 nm, after being optimized from 850 nm at the very beginning of 1993. The wavelength was re-tuned for the thinner strained cathode used in 1994-1995.

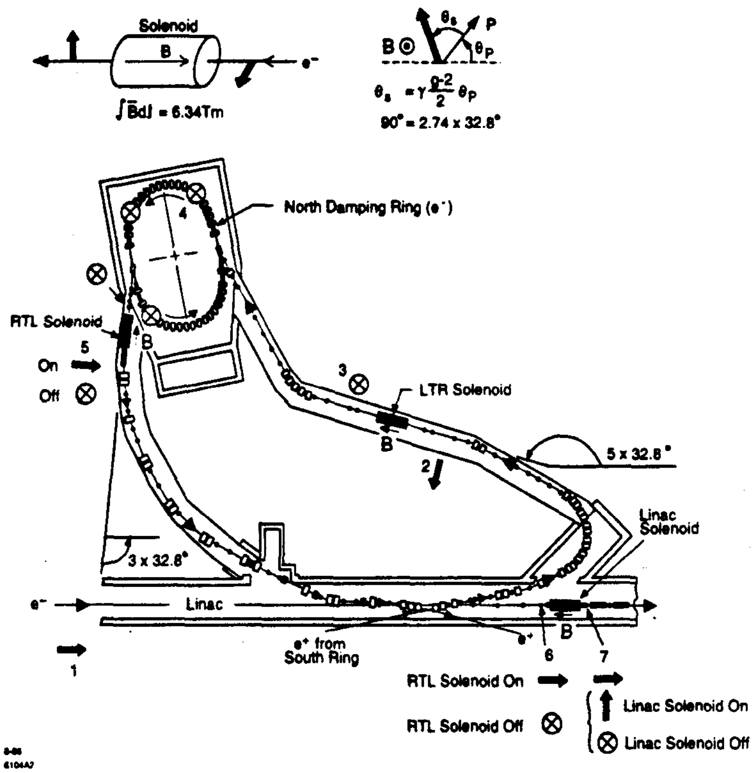

Figure 3.8: Spin transport in the North Damping Ring

The spin remains vertical in the damping ring, where the magnetic field is predominantly vertical. Any residual horizontal components to the spin quickly randomize away, as energy spread in the beam cause some electrons to precess faster than others. Upon extraction back into the Linac, the electron bunch passes through the NRTL (Ring-To-Linac) transfer line, which contains another spin-rotating solenoid. A third superconducting solenoid in the Linac shortly after the reinjection region provides a second degree of freedom in orienting the spin. The LTR solenoid's purpose is orient the spin vertically before the damping ring, so it cannot be used as a free parameter to orient the spin at the IP. The RTL and linac solenoids provide two independent adjustable spin parameters to orient the spin in any desired direction. This is necessary because the arc may introduce an arbitrary spin rotation, and the longitudinal component of the spin needs to be optimized at the IP for physics purposes.

3.4.5 Arc Spin Transport

The transport of the spin vector in the North SLC arc has yielded some surprises and has supplied some valuable techniques for optimizing the operation of the accelerator. If the arc were built in a flat plane, then the spin would precess about an axis parallel to the dipole field in each magnet, and the magnitude of this precession would be given by

$$\frac{d\theta_{spin}}{d\theta_{bend}} = \gamma\frac{g-2}{2}, \tag{3.2}$$

where $\gamma = E/m$ for the accelerated particles, and $(g-2)/2 \approx 1.163 \times 10^{-3}$ is the anomalous magnetic moment of the electron. A pure Dirac particle's spin vector precesses at the same rate the velocity vector rotates, keeping them parallel. It is this extra precession that enables electron synchrotrons such as LEP to measure their energies with extreme precision by scanning the beam energy over a spin tune resonance, which quickly depolarizes the beam.

The SLC arcs are not constructed in a plane, so the bending dipole fields are not all vertical. Thus the electron spins do not precess about a single axis as they travel around the arc. Because rotations about different axes do not commute, the cumulative effect of the precession in each bend of the arc is not a simple function of the total bending angle, as is predicted for a flat arc. In particular, the dependence of the spin orientation at the end of the arc on the path the electron beam takes through the magnets is rather strong, and this was noticed in the 1992 run. Detailed computer simulations of the spin transport in the arc predict qualitatively, but not quantitatively, the properties of the precession in the arc. The reason the spin orientation is as sensitive as it is to the arc orbit is because the spin tune and the betatron tune of the arc are unintentionally matched, and with each oscillation in the orbit, spin precession offsets added constructively [91][92].

Fortunately, these properties of the arc may be used to the advantage of the experiment. Because the spin orientation at the IP depends on the orbit, an orbit may be chosen to maximize the longitudinal component of the spin there [91]. Such orbit modifications were named "spin bumps," because they involved introducing small deviations from the ideal orbit.

To verify that optimal spin bumps are chosen, the measured longitudinal component of the polarization can be compared against the known total magnitude of the spin. This upper limit to available longitudinal polarization may be determined in two ways. The longitudinal polarization at the IP is measured with the Compton polarimeter for a variety of orbits, and the polarization is found as a function of orbit parameters such as the position and angle of launch into the arc. A more rigorous method is to adjust the RTL and Linac spin rotators so that three mutually orthogonal polarization states are produced. The longitudinal component of each of these is measured at the IP, and the sum in quadrature of the longitudinal components from each of these measurements is the absolute magnitude of available polarization. If the total available polarization is known, then it is a quick procedure to adjust the orbit in the arc to maximize the longitudinal component of the spin at the IP.

An advantage of introducing spin bumps is that the energy dependence of the spin orientation may be minimized. Because the section of the North Arc before the reverse bend (see Figure 3.9) bends the beam in the opposite direction than the rest of the arc, the precessions in the two sections partially cancel. An orbit may be chosen to decrease the effective number of precession turns in the second portion of the arc, which dominates the total precession. This may be done by choosing an orbit that orients the spin parallel to the local dipole fields for a longer section of the arc. Reducing the effective number of precession turns is important for optimizing the polarization and keeping it stable. Spin diffusion in the arcs is proportional to the energy spread and the number of effective turns, so reducing both improves the polarization.

Another benefit of being able to optimize the spin orientation using spin bumps in the arc is that the spin rotators in the RTL and the Linac may be switched off (the LTR rotator still has to be on in order to preserve polarization transmission through the NDR). Use of the RTL and Linac solenoids interferes with running flat beams, because they couple horizontal and vertical orbit deviations. Running the LTR solenoid is not a problem because the beams are flattened by the damping rings. Flat beams were commissioned in April of 1993 after the procedure for optimizing spin bumps became routine [78]. The final focus optics were originally optimized for

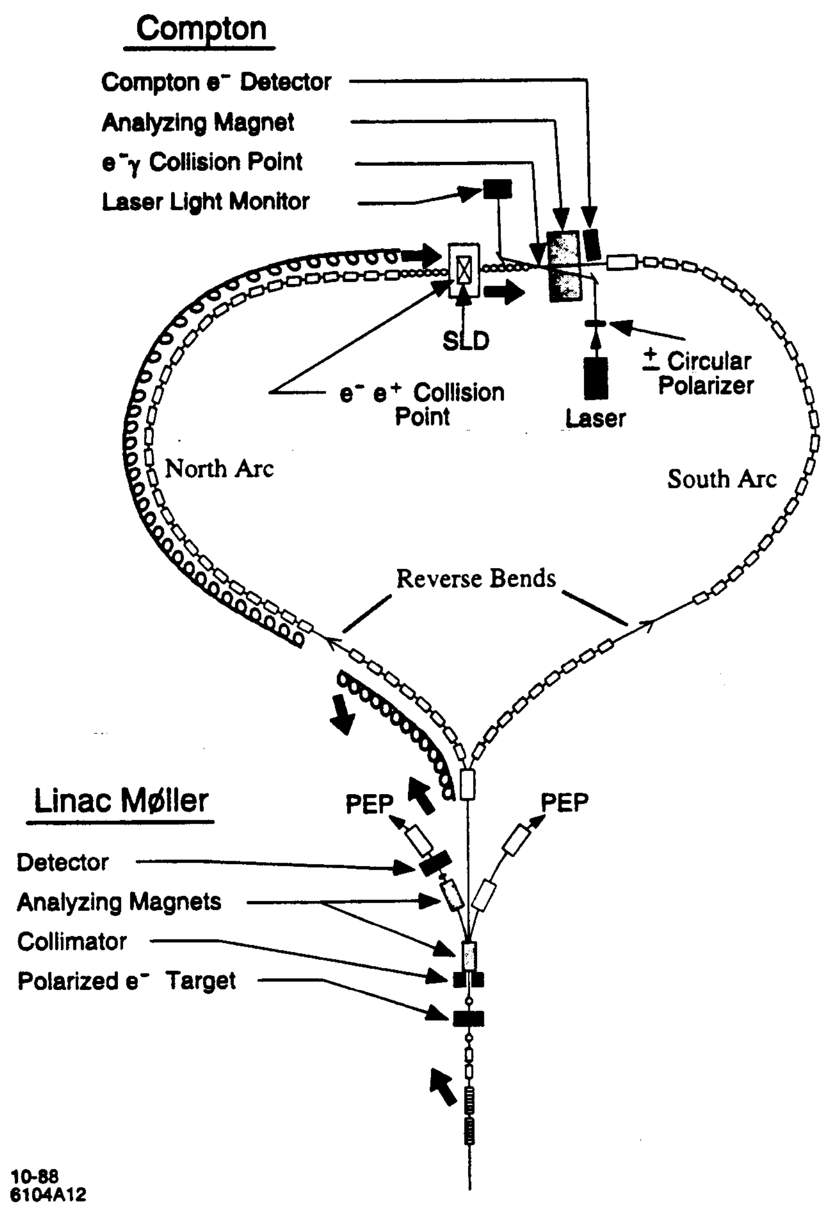

Figure 3.9: Spin transport and polarimeters at SLC.

round beams, and reduced the aspect ratio of the flat beams. An upgrade to the optics [83], installed for 1994–1995 running, reduces the chromatic distortions and better preserves the aspect ratio.

3.5 Spin Measurement

The polarization dependence of the cross sections of $e^+e^- \rightarrow Z^\circ \rightarrow f\overline{f}$ arises in this experiment entirely from the longitudinal component of the electron spin. It is important to measure this quantity as close to the interaction region as possible to reduce systematic error on asymmetry measurements, and to measure it continuously, so that a luminosity-weighted average may be performed.

To measure the polarization accurately enough for the SLD A_{LR} measurement, and to provide cross-checks, several polarimeters were put to use. A Compton polarimeter [93] provided the main measurement of the polarization during the run. A Møller polarimeter at the end of the Linac was used at selected times as a cross-check. In addition, a Mott polarimeter was used to test the cathode polarization, and that polarization was cross-checked independently by several polarimeters at other institutions. To check the polarization calibration of the Compton polarimeter, a second Møller polarimeter was installed in the electron extraction line at the end of the 1993 run, and also run briefly at the beginning of the 1994–1995 run.

3.5.1 Compton Polarimeter

The Compton polarimeter brings circularly polarized photons into collision with the SLC electron beam and measures the rate of Compton scattered electrons as a function of their energy. The electron beam arrives with randomly alternating helicity, and the helicity of the photons may also be chosen on a pulse-to-pulse basis. By comparing the asymmetries of the scattering rates in each of the four spin combinations, the polarization of the left-handed and right-handed electron bunches may be measured independently with high precision.

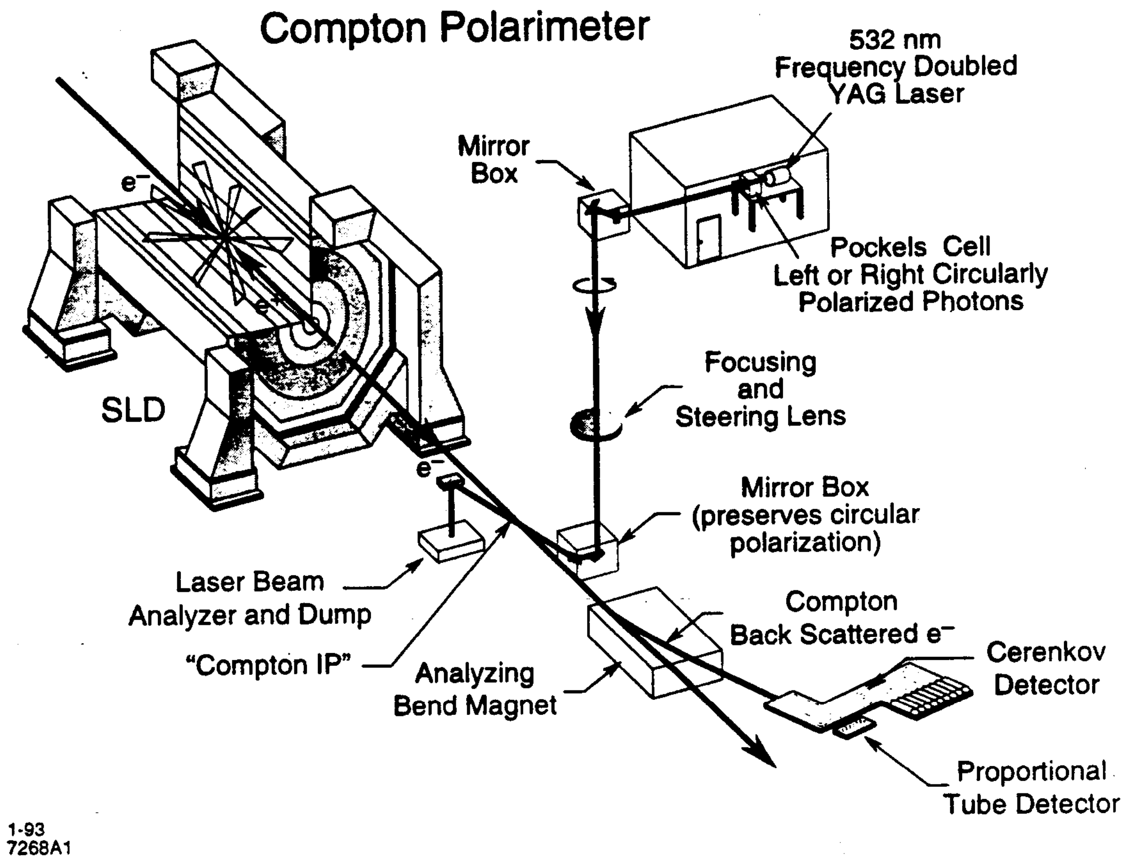

Figure 3.10: The Compton Polarimeter in the South Final Focus

Compton Layout

The Compton polarimeter is designed to measure the electron beam polarization with a minimum of bias, and to allow what biases there are to be measured. The polarimeter consists of a laser, polarizing optics, a beam transport tube, analyzing optics, an energy-analyzing bend magnet, and a detector for scattered high-energy electrons. In contrast to polarimeters at storage rings, the scattered photons are not used in the measurement.

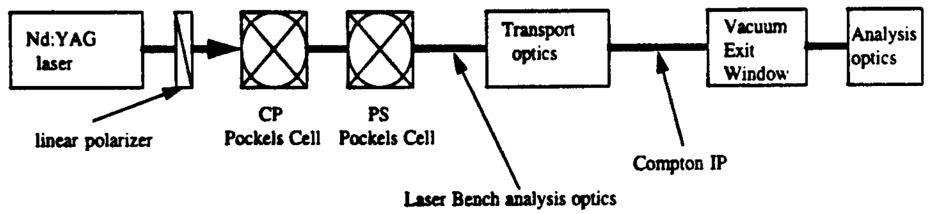

Figure 3.11: Schematic diagram of the Compton polarimeter optical layout.

Compton Laser

A Q-switched Nd-YAG laser, frequency-doubled to a wavelength of 532 nm (2.33 eV/photon, green), supplies the light for the Compton measurement. To obtain adequate scattering, the laser must produce a short, intense pulse — long pulses would not fully overlap with the electron beam if the crossing angle is finite, and the scattering must be localized to a region of the electron beampipe free of bending magnetic fields. The energy delivered to the Compton interaction region per pulse was 50 mJ and the pulse duration was 7 ns. The laser only fired on a fraction of available electron beam-crossings; the electron bunches arrive at 120 Hz, and the laser pulsed on average at 11 Hz (1993) and 17 Hz (1994-5). The frequency was chosen to keep the laser pulses from being synchronized with periodic behavior of the collider[¶].

Polarizing Optics

The most important optical elements immediately after the laser are a linear polarizer and two Pockels cells [95]. The first Pockels cell's optical axis is oriented at 45° to the plane of linear polarization of the incoming light, and can circularly polarize the laser beam with either handedness. Typical voltages applied to the first Pockels cell are $\pm$1200V. The optimal voltages for the two helicities are not exactly negatives of one another due to residual optical activity in the Pockels cell crystal even at zero applied voltage. The helicity is chosen pseudorandomly to explore all spin combinations with

[¶]This strategy was not entirely successful in 1994, as an energy feedforward device in the north damping ring caused every seventh SLC pulse to be off-energy, and the Compton laser pulsed every seventh SLC cycle. Fortunately, this did not cause a significant problem for analyses because the relative phase of the off-energy pulse constantly drifted. See Reference [94] for details.

the electrons with equal weight.

The second Pockels cell's optical axis is aligned at 90° to the first one, and together with the first cell, allows for the separate manipulation of the Stokes parameters of the laser light[‖]. In particular, components of the light transport system can incur phase shifts in the left- and right-handed components of the light, transforming circularly polarized light into elliptical light by the time it gets to the Compton interaction region. These phase shifts can be measured by opening the vacuum chamber of the electron beampipe and measuring the polarization components at the interaction region itself. Care must be taken because mechanical stress on vacuum windows may affect the phase shifts they induce.

The transport line phase shifts are also affected by the temperature of the optical elements and their coatings, and by their alignment. It is necessary to measure these phase shifts continuously throughout the run to minimize systematic uncertainties. A procedure to scan the voltages of the two Pockels cells, described later, was instituted to perform this task.

Transport Line

The laser light, after being appropriately polarized, is then guided from the optical bench to the Compton interaction region in the SLC tunnel. The total length of the laser transport system is 40 meters. Four compound mirrors are needed to bring the light from the laser shack to the SLC beampipe. Each compound mirror consists of two matched mirrors in order to compensate for phase shifts incurred by reflection and passage through optical coatings. A remotely movable lens in the transport system serves the dual purposes of focusing the light in the interaction region and steering the laser beam into collision if the alignment is disturbed, usually by diurnal temperature variations. The transport tube itself was evacuated for the majority of the 1993 run. but filled with helium at low pressure later in the run to help control damage to the optics, which was suspected to arise from electrical breakdown in the residual gas

[‖]There are four Stokes parameters, but two degrees of freedom are taken by the total light intensity and the fraction of unpolarized light, leaving two degrees of freedom for the polarization, which may be manipulated by the voltages on two Pockels cells.

near the optical elements. After exiting the laser transport tube, the light passes through a vacuum-tight quartz window to the SLC vacuum chamber. The crossing angle of the laser light and electron beam is 10 mrad, and the Compton interaction point is 32 meters south of the SLC interaction point.

Analysis Box

After colliding with the electron beam, the remaining laser light is brought out of the SLC beampipe through another quartz window and its polarization is measured by breaking it into its left- and right- handed components with a quarter-wave plate and a calcite prism [95]. The measurement of the light polarization after the Compton interaction point is critical for determining the unpolarized fraction of the laser light. By adjusting the voltages on the two Pockels cells, one may explore all possible polarization states at the end of the light transport system. If the maximum attainable polarization in the analysis optics falls short of unity, then a component of unpolarized light may be inferred. For the 1993 run, the unpolarized fraction has been determined in this manner to be less than 1.0%, and for the 1994–5 run, it is less than 0.6%.

Compton Spectrometer and Detectors

The electrons which undergo Compton scattering are deflected away from the beamline by two arc bending magnets. The integral of $B \cdot dl$ in these magnets is 1.67 kGauss-meters. A detector is placed 355 cm downstream from the bend point of the spectrometer, covering the region from $\simeq 5$ cm from the beam to $\simeq 14$ cm. This latter coverage can be adjusted by pivoting the detector table, maintaining the projectivity of the Cherenkov radiator tubes to the Compton IP. The detector assembly consists of one inch of lead as a shower preradiator and nine Cherenkov radiator tubes filled with a propane for the majority of the 1994-1995 run (β-butylene was used as a radiator previously, with the switch to propane made in order to reduce buildup of residue on the optical surfaces). Behind the tubes, but offset away from the beamline so as to reduce background from the showering electrons, are Hamamatsu R1398 phototubes to record Cherenkov radiation. Set behind the Cherenkov radiator tubes is an array

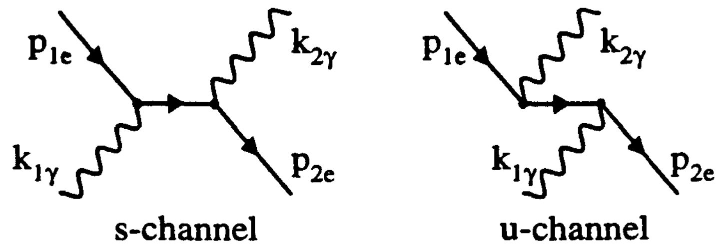

Figure 3.12: Lowest-order contributions to Compton scattering. In the totally backscattered case at high energy, the s-channel process is highly suppressed. The kinematic variables labeled are SLC laboratory frame variables.

of 16 proportional tubes in a block of tungsten. The signal from the proportional tubes is correlated with that from the Cherenkov tubes on a pulse-to-pulse basis, so the measured polarization is expected to be the same. The purpose of having two detectors is to provide cross-checks on them both.

Compton Measurement

The differential cross-section for Compton scattering is given to lowest order by computing the two diagrams of Figure 3.12. For unpolarized scattering, the differential cross-section is given by the Klein-Nishina formula [96] in the rest frame of the electron:

$$\frac{d\sigma}{d\cos\theta} = \frac{\pi\alpha^2}{m_e^2}\left(\frac{k'}{k}\right)^2\left[\frac{k'}{k} + \frac{k}{k'} - \sin^2\theta\right], \tag{3.3}$$

where k is the initial energy of the photon, k' is the final energy, and θ is scattering angle of the photon. The electromagnetic coupling constant α takes nearly its $Q^2 = 0$ value due to the small center-of-mass energy of the e-γ collision. The scattering angle and energies are related by the relativistic kinematic constraint:

$$k' = \frac{k}{1 + \frac{k}{m_e}(1 - \cos\theta)}. \tag{3.4}$$

Boosting this result into the SLC frame, one obtains:

$$\frac{d\sigma}{dE_2} = \frac{\pi\alpha^2}{mk^2}\left(\frac{k'}{k} + \frac{k}{k'} + 1 - \left(1 + \frac{m_e}{k} - \frac{m_e}{k'}\right)^2\right). \tag{3.5}$$

Expressed in terms of SLC laboratory frame variables, k and k' become

$$k = \frac{E_{1\gamma}E_1}{2m_e}, \tag{3.6}$$

and

$$k' = \frac{E_{1\gamma}E_1}{2m_e}\left(1 - \frac{(E_1 - E_2)}{E_1}\right), \tag{3.7}$$

where E_1 is the electron beam energy (45.6 GeV), $E_{1\gamma}$ is the incident laser beam energy (2.33 eV), and E_2 is the scattered electron's energy.

Equations 3.3 and 3.5 are averages over the incident electron and photon spin states. The full polarization-dependent formula can be expressed as two terms — one symmetric in the initial longitudinal spin state configuration, and one antisymmetric in it. It is the product of the electron and photon spins that appears because the process obeys parity symmetry. The two $J = 3/2$ initial state combinations have the same scattering cross section, which is larger in the backscattered case than the cross section of the two $J = 1/2$ initial states.

$$\frac{d\sigma}{dE_2} = \frac{d\sigma_{unpolarized}}{dE_2}[1 + \mathcal{P}_e\mathcal{P}_\gamma A_{Compton}(E_2)] \tag{3.8}$$

The quantity $A_{Compton}$ is defined to be the "analyzing power" for Compton scattering, the dilution of the polarization asymmetry when the asymmetry of the scattering is formed:

$$A_{Compton}\mathcal{P}_e\mathcal{P}_\gamma = \frac{\sigma_{3/2}(E) - \sigma_{1/2}(E)}{\sigma_{3/2}(E) + \sigma_{1/2}(E)}. \tag{3.9}$$

This asymmetry can be expressed in terms of SLC variables [97]:

$$A_{Compton} = \frac{(AB^3 - A^3B) + m_e^2(AB^2 + A^2B - A^3 - B^3)}{(AB^3 + A^3B) + m_e^2(2A^2B - 2AB^2) + m_e^4(A^2 + B^2 - 2AB)}, \tag{3.10}$$

where

$$A = -E_1E_{1\gamma} - |p_1|E_{1\gamma} = -p^\mu_{1e}k_{1\gamma\mu} \tag{3.11}$$

is the dot product of the initial electron's four-momentum into the initial photon's, and

$$B = -E_2E_{1\gamma} - |p_2|E_{1\gamma}\cos\theta_p = -p^\mu_{2e}k_{1\gamma\mu} \tag{3.12}$$

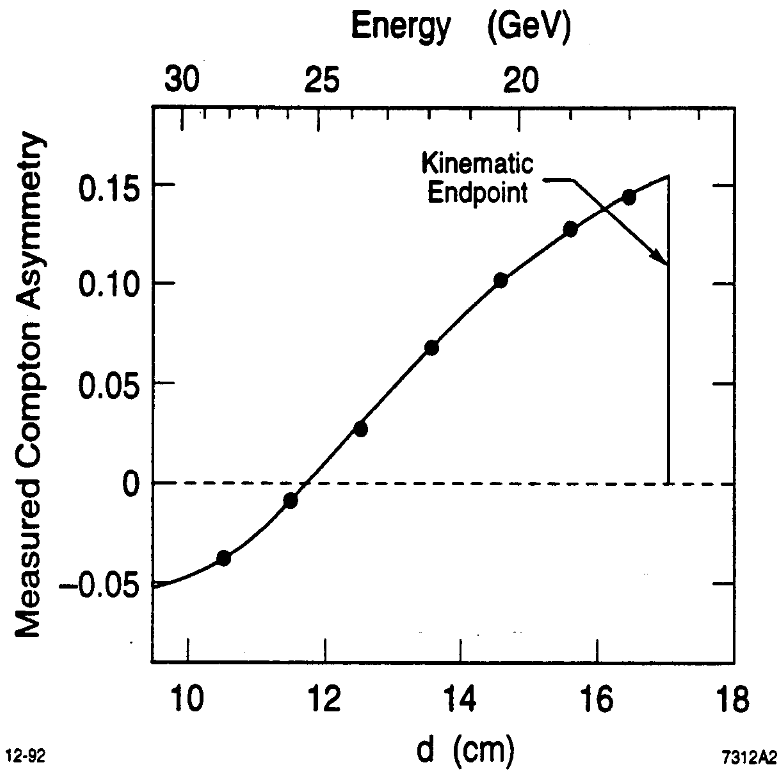

Figure 3.13: The asymmetry between the $J = 3/2$ and $J = 1/2$ states of Compton scattering as a function of the energy lost by the electron, compared against the measured asymmetry for $P_e = 63\%$. The distance scale is the deflection of the scattered electrons at the front of the Cherenkov detector.

is the dot product of the outgoing electron's four-momentum and the initial photon's. The electron's scattering angle θ_p is given by the following kinematic constraint:

$$\cos\theta_p = \frac{E_1E_2 + E_{1\gamma}E_2 - E_{1\gamma}E_1 - E_{1\gamma}|p_1| - m_e^2}{|p_2|(|p_1| - E_{1\gamma})}, \qquad (3.13)$$

where $|p_1|$ and $|p_2|$ are the momenta of the incoming and outgoing electron, respectively.

Because the Compton polarimeter detects only the scattered electrons, a higher-order QED calculation needs to be performed in terms of the energy of the scattered electron. Such a calculation has been performed to one loop, including bremsstrahlung [97]. The derived $A_{Compton}$ is shown in Figure 3.13.

To measure the asymmetry as a function of energy, the signal in each Cherenkov channel is accumulated separately for each combination of electron and laser helicity states, and also for those beam crossings on which the laser did not fire. Let s^i_{jk} be the average of the signal in channel i when the electrons are in state $j = (L, R)$ and the photons are in state $k = (L, R, off)$, and let σ^i_{jk} be the statistical error on s^i_{jk}. Then the raw asymmetry for the left-handed electron beam is given for each channel by

$$A^{L,i}_{raw} = \frac{s^i_{LR} - s^i_{LL}}{s^i_{LR} + s^i_{LL} - 2s^i_{Loff}}, \tag{3.14}$$

and for the right-handed electron beam it is

$$A^{R,i}_{raw} = \frac{s^i_{RR} - s^i_{RL}}{s^i_{RR} + s^i_{RL} - 2s^i_{Roff}}. \tag{3.15}$$

In this way the polarization of both helicity states of the electron beam may be measured independently, even if the backgrounds and beam currents are systematically different for the two beam states. The statistical error on $A^{L,i}_{raw}$ is given by

$$\delta A^{L,i}_{raw} = \frac{2((s^i_{LL} - s^i_{Loff})^2(\sigma^i_{LR})^2 + (s^i_{LR} - s^i_{Loff})^2(\sigma^i_{LL})^2 + (s^i_{LR} - s^i_{LL})^2(\sigma^i_{Loff})^2)^{1/2}}{s^i_{LR} + s^I_{LL} - 2s^i_{Loff}}. \tag{3.16}$$

with a similar expression holding for the right-handed case.

Two features of Compton scattering serve to provide absolute reference points in the scattering spectrum. The first of these is the kinematic scattering limit. Electrons of energy E_1 may lose a maximum energy of

$$\Delta(E)_{max} = E_1 \left[1 - \left(1 - \frac{4E_1E_{1\gamma}}{m_e^2}\right)^{-1}\right] \tag{3.17}$$

when they strike photons of energy $E_{1\gamma}$, corresponding to backscattering in the Compton CM frame. For E_1 = 45.6 GeV and $E_{1\gamma}$=2.33 eV, backscattered electrons have an energy of 17.37 GeV in the laboratory frame. These electrons are deflected 52.7 mrad by the spectrometer magnets and are intercepted by the Compton detector 355 cm downstream from the bend point. Unscattered electrons are bent by 20 mrad, so the displacement of fully backscattered electrons from the beampipe at the detector is 11.6 cm.

The other landmark on the Compton spectrum is the zero asymmetry point, corresponding to a scattering angle of $\pi/2$ in the Compton CM frame. This corresponds to an angle of 36.2 mrad after the bend spectrometer. Together, these two points on the Compton spectrum serve to locate its image on the Cherenkov tubes, and to determine its distance scale. The Cherenkov detector was positioned so that the kinematic endpoint lay in the acceptance of the seventh channel from the beampipe, while the zero asymmetry point lay in the acceptance of the second channel. Studies with the EGS shower simulation program [98] were done to evaluate the effects of signal sharing between channels and the resulting expected asymmetry fit to the data is shown in Figure 3.13.

The Compton measurements are statistically powerful because they sample a large fraction of the beam crossings from SLC. Only the signal from the channel closest to the Compton endpoint is used to minimize systematic errors. The signal in the other channels of the detector are correlated with one another not only because of the width of the electromagnetic showers, but because the luminosity of the e-γ collision depends on the temporal details of the laser pulse, which fluctuate significantly from pulse to pulse.

Systematic Errors

Linearity

One of the systematic errors on the polarization measurement arises from nonlinearities in the responses of the detector, phototubes, and electronics. The emission of Cherenkov radiation in the detector is an inherently linear process – there is no saturation effect as additional shower electrons travel through the same radiator. The signal may be degraded by coatings and contamination on the reflective surfaces on the channel walls and mirrors, but this has no effect on the asymmetries. Phototubes, on the other hand, saturate easily and care must be taken to keep the voltage on the different stages from sagging under the load of a large signal. A special phototube base was designed [99] to improve linearity. The linearity of the digitizers was measured with an external pulse generator [100].

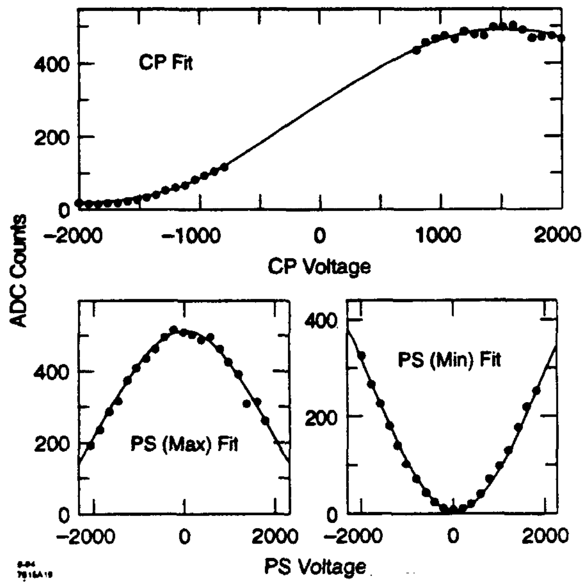

Figure 3.14: A scan over the voltages of the CP and PS Pockels cells to determine the quarter-wave voltage and the unpolarized fraction.

The linearity of the entire system may be measured in several ways. One is to adjust the voltage on a single phototube until it starts to saturate. The beam polarization is monitored by the other phototubes in the system and the test phototube's asymmetry is compared against the others. It is then estimated how far the normal operating point is from the nonlinear region.

A second method is to adjust the laser power until the signal gets large enough to affect the system's linearity. Because the phototube gains vary significantly, some channels will enter their nonlinear regions before others. Testing consistency between the polarizations derived from the raw asymmetries in each channel also provides an estimate of the reliability of the measurement. The estimated error from detector linearity for the 1994-1995 run is 0.5%.

Laser Polarization

Another systematic error arises from the need to know the laser polarization to compute the electron polarization. Because the transport line contains many optical elements which can introduce relative phase shifts between the linear components

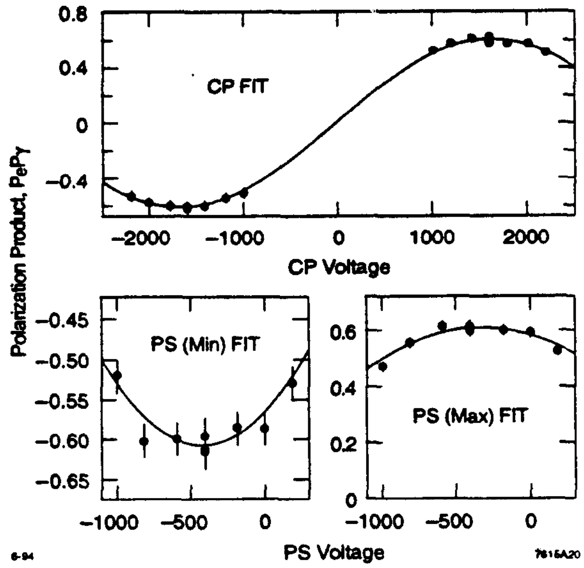

Figure 3.15: A scan over the voltages of the CP and PS Pockels cells to determine the optimal phase of the light to measure the electron beam polarization.

of the light, the absolute magnitude of the laser polarization at the scattering point must be treated carefully in order to reduce its uncertainty. The voltages on both Pockels cells are routinely scanned and the Compton asymmetry measured on each scan point. The asymmetry is then fit to a function sinusoidal in the voltages of both of the Pockels cells:

$$P_e^{meas} = P_e^0 \cos(V_{CP} - V_{CP}^0) \cos(V_{PS} - V_{PS}^0). \tag{3.18}$$

Here, V_{CP} is the voltage on the circularly polarizing Pockels cell, and V_{PS} is the voltage on the phase shift Pockels cell. The parameters P_e^0, V_{CP}^0, and V_{PS}^0 are allowed to float in the fit, and P_e^0 is the measured value of the polarization. A sample of a complete scan is shown in Figure 3.15. To determine the unpolarized fraction of laser light, every hour a fast scan over the two Pockels cell voltages was done and the photon polarization measured in the analysis box. A sample scan is shown in Figure 3.14, where the unpolarized fraction is $< 1\%$. The total estimated systematic error on the electron polarization arising from uncertainties in the laser polarization is 0.2% (1994–1995) and 1.0% (1993).

To monitor the electron polarization during the run, the measurements are alternated between those near $V_{CP} = V^0_{CP}, V_{PS} = V^0_{PS}$, and measurements at other voltages. These measurements are less sensitive to fluctuations in the transport line's phase shift, owing to the zero derivative of the cosine function at its maximum, and are reported to the experiment and accelerator operators during the run.

3.5.2 Møller Polarimeter

Because the SLD measurement of A_{LR} is the most precise single measurement of $\sin^2\theta_W$, and because the main systematic error on that measurement arises from uncertainties in the electron polarization measurement, it was determined that a second measurement of the electron polarization needed to be done with a polarimeter with systematic uncertainties as independent as possible from those of the Compton polarimeter.

A second polarimeter [101], taking advantage of the unequal Møller cross-sections for aligned and antialigned incident and target electron spins, had already been installed in the SLAC beam switchyard for use with the fixed-target program. The target, a thin, magnetizable foil, is inserted in the beam in the switchyard. The dipole necessary for shunting electrons into the PEP injection line is then used as a momentum-analyzing magnet. A detector is then located at such a place that 46.6 GeV electrons scattering elastically on target electrons in the foil will be steered into it by the analyzing magnet. The detector consists of 64 silicon strips with a pitch of 600 μm, oriented perpendicular to the swath of electrons swept out by the analyzing magnet so as to form an energy spectrometer. Collimators and shields reduce backgrounds from electrons scattering on the nuclei in the target. The target is surrounded by three pairs of Helmholtz coils, which may magnetize the target in any direction. By using these three axes of target polarization, the three components of the beam polarization may be measured.

The scattering of high-energy polarized electrons and a stationary polarized electron target allows the measurement of the initial beam's polarization [101]. Typical targets are made of an iron-cobalt-vanadium alloy (Vanadium-Permendur: 49% Fe, 49% Co, and 2% V). The observed asymmetry, however, is diluted by the fact that at

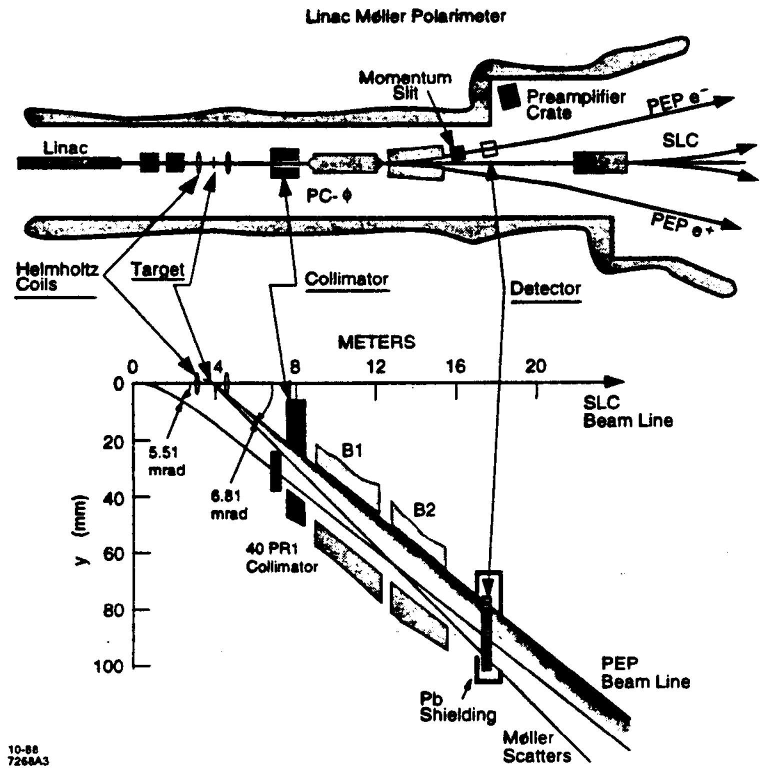

most one electron per atom participates in the magnetic ordering, while all electrons contribute to Møller scattering.

The analysis of Møller polarimeter data mainly consists of understanding the signal shape, estimating the background contribution, and fitting the asymmetry as a function of scattered electron energy. A naïve fit of the data from this polarimeter is shown in Figure 3.16 and yields a polarization value of (82.4±2.7)%, whereas the Compton measured (65.7±0.9)%, after correcting for expected depolarization in the North SLC arc. It was originally believed that the arc depolarization was poorly modeled. When the energy spread was reduced to minimize spin diffusion, and the number of effective turns reduced, the discrepancy between the Compton and Linac Møller remained.

A more complete analysis [101] of the data from the Møller polarimeter was performed shortly after a paper by M. Levchuk [102] was found that described the effect of the motion of atomically bound electrons on the spectrum from a Møller polarimeter. The effect arises from the fact that the inner shell electrons in iron are unpolarized,

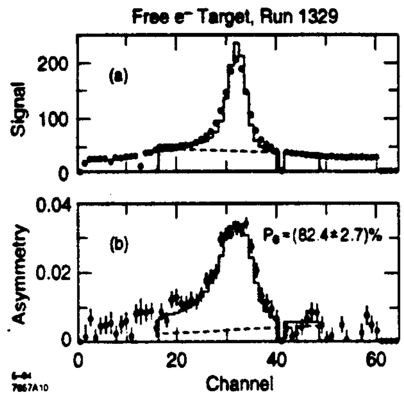

Figure 3.16: A fit to the measured signal and asymmetry (points) using the unbound electron hypothesis (histogram). Dashed lines indicate estimated background signal and asymmetry. From Reference [101].

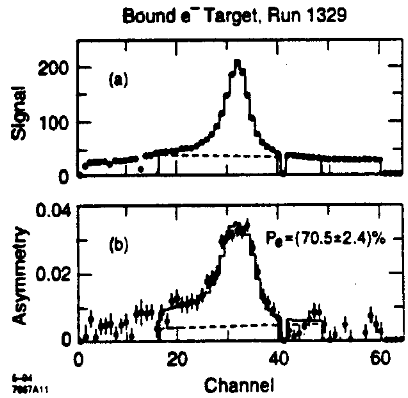

Figure 3.17: A fit to the measured signal and asymmetry (points) using the bound electron hypothesis (histogram). Dashed lines indicate estimated background signal and asymmetry. From Reference [101].

but they have a higher expectation value for their speed in the laboratory frame. While their energy is still much less than that of the incident beam, it greatly affects the energy in the collision's center of mass. This atomic motion serves to broaden the energy spectrum of the scattered electrons. Nonetheless, the very outermost electrons, which carry all of the atom's magnetization, have relatively little kinetic energy before they are struck. Their contribution to the energy spectrum of scattered electrons is narrower, and carries all of the asymmetry. If the analysis is performed assuming that the expectation value of the electron's spin is independent of its kinetic energy, then the extracted polarization may be a mismeasurement by as much as 15%. A more complete fit is shown also in Figure 3.17, and the extracted polarization is (70.0±2.4)%, consistent with the Compton measurement.

A third polarimeter was installed at the end of the 1993 SLD run as a further cross-check before the reanalysis of the Linac Møller data was performed. This polarimeter was another Møller installed in the south electron extraction line. In 1993, approximately 3/4 of the scattered electrons were shadowed by a vacuum fitting and did not travel to the detector. It was left in place to be re-run at the beginning of the 1994 run with several different target materials to test the intra-atomic electron motion assumptions, and to remove the occlusions. Its polarization measurements are also consistent with those of the Compton.

The main systematic error in Møller polarimetry is the uncertainty on the polarization of the target. The magnetization of a thin foil in an applied field is expected to be non-uniform — the magnetization in the center of the target foil is expected to exceed that near the edges. The estimated error is roughly 4% of the measured value. Other errors arise from the assumptions made in the analysis of the asymmetry of the background. If a Møller scattered electron scatters again in the field of a nucleus of another target atom, it will contribute to another portion of the energy spectrum, carrying its original asymmetry with it. This effect can be mitigated by using a thinner target foil. The total systematic error from Møller polarimetry is expected to be irreducible beyond 4%, and therefore no plans are made to use it in the future as a measurement or as a cross-check.

As a further cross-check on the absolute scale of the electron beam polarization, a sample of unstrained cathode material was measured in the laboratory, and similar samples cut from the same wafer were sent to Rice University and the University of California, Irvine, where existing Mott polarimeters, with a nominal 1% precision, measured polarizations consistent with those measured in the SLC gun cathode test laboratory. This test bench measured the polarization of the strained cathode used in the 1993 run to be 65%, also confirming the scale of the Compton polarimeter. Not all of the data were conclusive, though — samples tested at Nagoya and also the PEGGY polarimeter [103] at SLAC reported higher polarizations than those measured on the cathode test bench.

3.5.3 Energy Spectrometer

The WIre Synchrotron Radiation Detector (WISRD) performs the absolute energy measurement for the SLD experiments [104]. It is located in the electron extraction line shortly before the beam dump. A second unit is located in the corresponding location of the positron extraction line. Each spectrometer consists of two strong horizontal bend magnets and a weaker vertical bend magnet, shown in Figure 3.18.

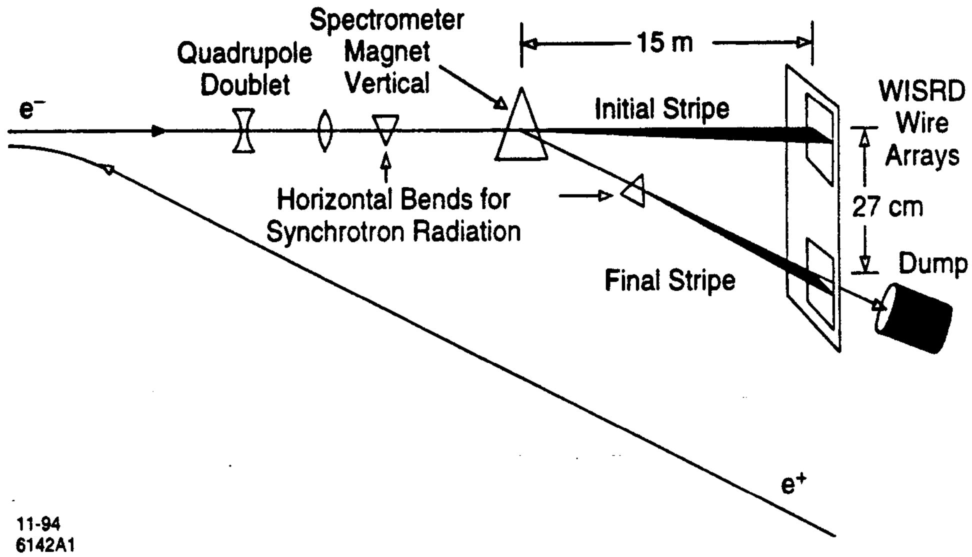

Figure 3.18: The Wire Imaging Synchrotron Radiation Detector (WISRD)

The first horizontal bend causes the electron beam to emit a horizontal swath of synchrotron radiation. It is immediately followed by a softer vertical bend, which deflects the beam downwards and serves as the energy analyzing magnet. The second hard horizontal bend deflects the electrons in the opposite direction as the first horizontal bend, and creates a second swath of synchrotron radiation. The vertical separation between these two swaths of radiation is inversely proportional to the energy of the beam. The difference in widths of the two swaths provides information about the energy spread of the beam.

The locations of the two swaths of synchrotron radiation are measured by proportional wire chambers located 15 m downstream from the magnets. The wire spacing is 100 μm and they provide a resolution on the beam energy of 22 MeV. The energy spread resolution is less well known, and is best estimated with wire scans in high-dispersion locations in the arcs. Typical values of the energy spread are in the range of 50-100 MeV. Because the analysis presented in this thesis is only minimally dependent on the beam energies, errors from their measurement may be neglected.

Table 3.2: SLC performance parameters for 1993–1995.

Parameter	1993	1994–1995
e^+/bunch	3.0×10^{10}	3.5×10^{10}
e^-/bunch	3.0×10^{10}	3.5×10^{10}
σ_x	2.6 μm	2.3 μm
σ_y	0.8 μm	0.5 μm
E_{CM} (GeV)	91.26	91.26
Energy Spread (%)	0.25	0.12
P_e	63.0 ± 1.1	77.3 ± 0.6
$\mathcal{L}$ (cm^2s^{-1})	3.8×10^{29}	6×10^{29}
Integrated Z^0's	5.0×10^4	1.0×10^5

3.6 Summary

SLC's luminosity and polarization improve with every run. New cathodes for higher polarization, more feedback mechanisms for stability and increased collision time, rebuilt damping rings for higher current, and improved final focus optics for better chromatic behavior, have all contributed to SLC's recent successes. Many of the lessons learned at SLC will be valuable in designing and operating linear colliders of the future.

The Compton polarimeter is the highest-precision electron polarimeter operating at the beam energies of SLC, allowing precision tests of the Standard Model to be made.

Chapter 4

Experimental Apparatus: SLD

The SLC Large Detector (SLD) [105] is a multi-purpose device for measuring the properties of the decay products of the Z^0 boson. It consists of subystems which do tracking and precision vertex measurement, particle identification, calorimetry, muon identification, and luminosity measurement. The main goals of the detector elements are to provide signatures for as many of the different fermions the Z^0 may decay into, and also to provide measurements of the decay properties of those particles into which the Z^0 decays. Particular attention to the tracking subsystems will be paid in this chapter because they are the most important for the analysis presented in this thesis.

4.1 Luminosity Monitor

The SLD luminosity monitor [106] consists of two distinct subsections: the Luminosity Monitor and Small Angle Tagger (LMSAT), which covers the angular region from 23 mrad from the electron beam to 68 mrad, and the Medium Angle Silicon Calorimeter (MASiC), which covers the region from 68 mrad to 190 mrad.

The LMSAT is used primarily to detect e^+e^- pairs that have undergone Bhabha scattering at the SLC interaction point (IP). At low angles, the Bhabha cross-section is dominated by t-channel photon exchange and grows proportional to θ^{-4}, where θ is the scattering angle. As Bhabha scattering is easily calculable to high precision

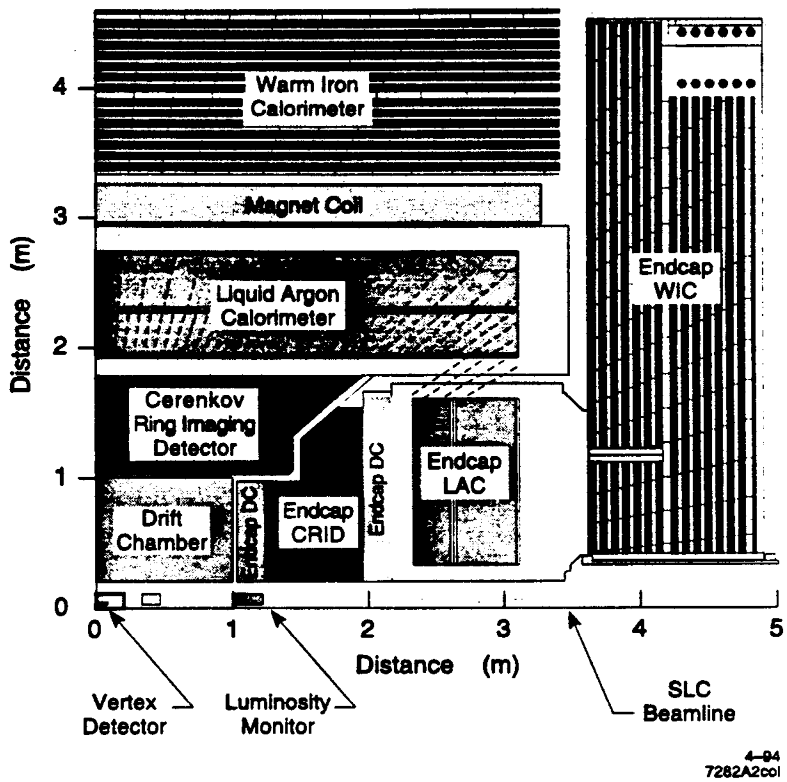

Figure 4.1: Quadrant view of SLD, showing the precision tracking, particle identification. calorimetry, and muon identification subsystems.

in QED, and because it occurs much more often than Z^0 production, it provides a precise measurement of the accelerator luminosity.

The LMSAT detectors are segmented into 32 sections in ϕ and 6 sections in θ (LMSAT). It is segmented into two longitudinal segments of 5.5 and 15.6 radiation lengths. The detectors are composed of tungsten radiator plates interleaved with silicon junction devices maintained in reverse bias. The energy resolution of the detector has been measured [107] to be 6% at 50 GeV.

4.2 Tracking: Central Drift Chamber

The bulk of the work of identifying and tracking the charged decay products of the Z^0 is performed by the Central Drift Chamber (CDC) [108]. Combined with the Vertex

Detector, it provides precision tracking necessary for heavy-quark physics at SLD.

4.2.1 Mechanical Design

The CDC consists of eighty layers of sense wires in a low-mass aluminum/Hexcel shell with an inner radius of 20 cm and an outer radius of 1 m. The total length of the chamber is 2 m, although dishing of the endplates causes the length of the wires to vary slightly from layer to layer. The CDC, as well as the particle identification system and the liquid argon calorimeter, lie inside a solenoidal magnet supplying a uniform 0.6 T field parallel to the beam direction. The drift gas is a mixture of 75% CO_2, 21% Argon, 4% Isobutane, and 0.2% H_2O and is maintained at a constant temperature of 20 °C by a precisely controlled water cooling system. The pressure is allowed to equalize with the ambient atmospheric pressure. The drift velocity is 7.9 μm/ns in the mean drift field of 0.9 kV/cm. The estimated Lorentz angle is a very small 49 mrad*.

The eighty layers of sense wires are grouped into ten "superlayers" of eight wires apiece†. The first eight of these are arranged to be parallel to the beam ("axial layers"), while the next eight are tilted at an angle of 42 mrad to provide stereo information ("U layers"). The next eight are tilted also, but at an angle of -42 mrad ("V" layers). The pattern is repeated, with the last eight wires forming an axial layer, and the overall layout is shown in Figure 4.2. The construction of the basic cell consists of a drift region with a nearly uniform field set up by the field and guard wires, and a nonlinear region between the guard wires and sense wires. Each cell measures roughly 6 cm wide by 5 cm high. A field map for a single cell is shown in Figure 4.3, illustrating the effects of the two ends of the cell on the electric field. The sense wires and guard wires of each cell are mounted on feedthroughs in a single block of Lexan on each end of the chamber. The field wires are supported by Celanex feedthroughs cold pressed into the chamber endplate. The sense wires are made of 25 μm gold-coated tungsten and are held at 100 gm tension, while the guard and field

*It is the cosine of the Lorentz angle which corrects the drift distance, so the total effect is on the order of 0.1%. Nonetheless, it is incorporated in both the simulation and reconstruction.

†There are actually ten "sense" wires in a superlayer, but the outer two are not digitized. They serve to enhance the field uniformity for the other wires in the cell.

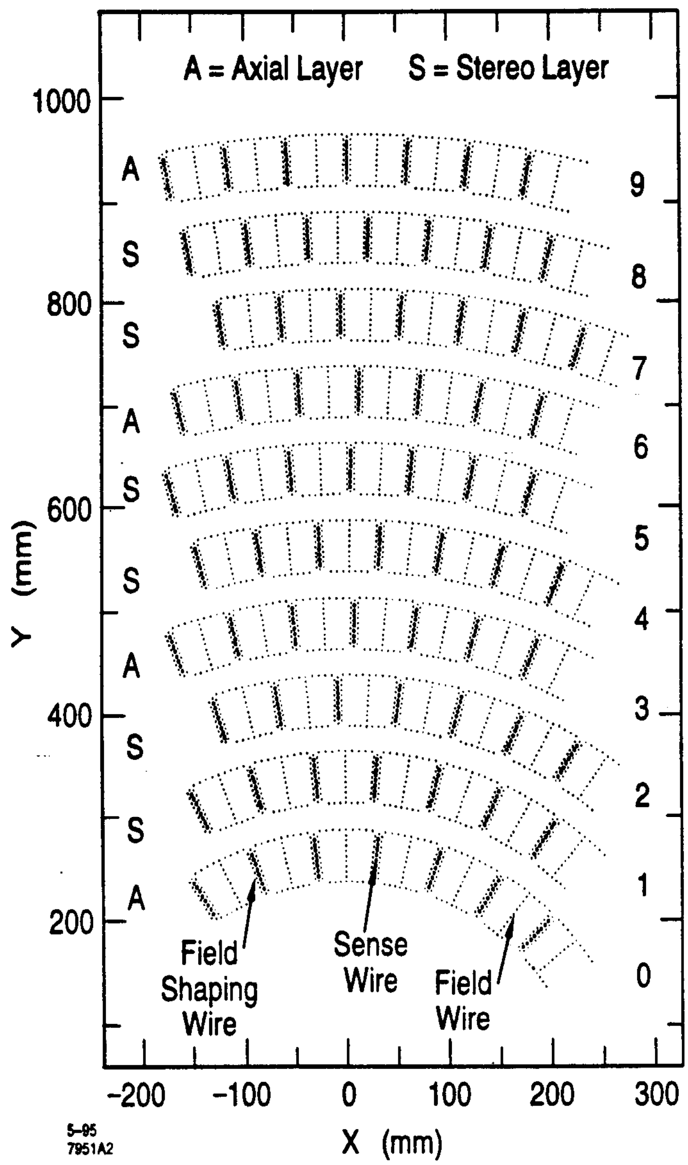

Figure 4.2: Cross-section of a portion of the CDC in the plane perpendicular to the beam axis. There are 540 projective drift cells in the chamber, each containing eight sense wires.

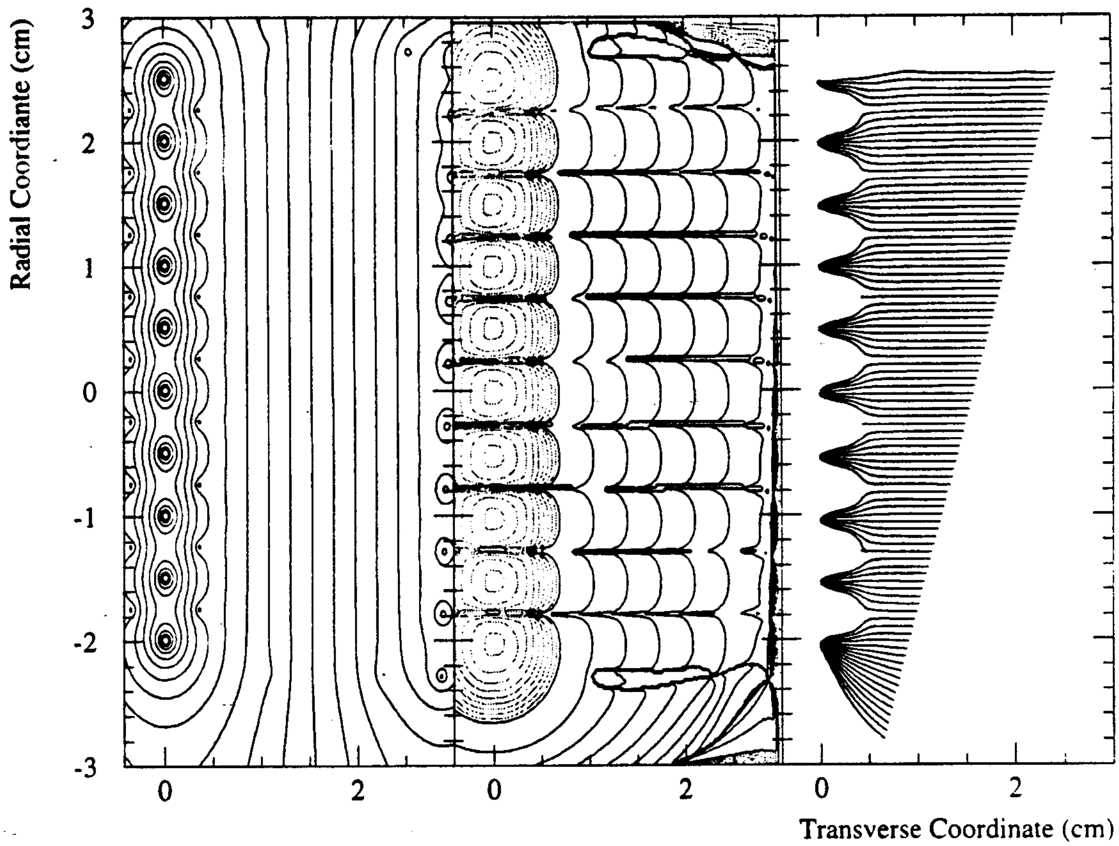

Figure 4.3: Diagrams showing the field in a half cell of the CDC. The leftmost figure displays the equipotentials of the electric field. Visible are four radially aligned layers of wires — the guard wires for the left half-cell, the sense wire plane, the right half-cell's guard wires, and the field wires to the right. The middle figure shows the drift-time isochrones for the same region. Isochrones near the sense wires are shown with 1/10 the spacing as those outside. The rightmost figure shows the drift paths of representative electrons in the field of the drift cell for a sample track. The top and bottom sense wires are not read out.

wires are made of 150 μm gold-coated aluminum and held at 500 gm of tension for the guard wires and 400 gm of tension for the field wires.

Electrical pulses on the sense wires are read out on both ends by high-speed sampling electronics mounted directly on the endplates of the chamber. Signals are sampled at 119 MHz and held in Hybrid Analog Memory Units (HAMUs), and digitized after the trigger decision has been made. Because the digitizers are mounted on the endplates, only digital information needs to travel to the data assembly electronics. Fiber optic transmission cables were chosen so as not to induce or receive electrical noise or create unintentional ground loops, and to reduce the total mass of cables on the detector.

Digitized signal values are then analyzed online by Waveform Sampling Modules (WSMs), located in Fastbus racks atop the detector. These modules apply a piecewise linear calibration correction to the incoming signals on a wire-by-wire basis. Pulses are found in the digitized waveforms by applying thresholds to the pulse height above baseline and the derivative of the pulse shape [109]. The found pulses are then analyzed to extract the pulse beginning time, end time, pulse height, width, and total charge. The signals on each end of the wire are analyzed separately for all wires on which a pulse is found. It is these quantities which are written to the SLD raw data tape in order to save space. A small fraction of randomly selected raw pulse data is also written for diagnostic purposes.

4.2.2 CDC Reconstruction

Tracks are found and fit in four stages — raw hit filtering, vector hit finding, pattern recognition, and track fitting. The first of these stages combines information for each pulse from both ends of the sense wire on which it arrived. The double-ended readout enables the position along the wire for that pulse to be estimated by calculating the charge division asymmetry for that pulse. The resolution on this estimate is approximately 2% of the wire length. Simple cuts are applied to the raw data pulses to remove common noise sources, such as synchrotron radiation and beam halo directly striking the amplifiers and HAMUs on the detector. These pulses are characterized by proximity in time to the beam crossing (no drift through the gas is involved), and small pulse height and total charge.

The second stage of reconstruction combines hits within superlayers which lie on straight lines or origin-constrained circles to form vector hits (VHs), which contain position and direction information for the track segments to which they correspond. Hit positions are then corrected for the effects of the relative angle between the track and the sense wire plane. The z location of each vector hit is estimated from charge-division information. The vector hit finder is described in more detail in Appendix C.

Pattern recognition [110] proceeds by analyzing the input VHs to form candidate tracks. Combinations of VHs on the axial layers of the chamber are formed by fitting them to circles. Discrimination between axial combinations is provided by attempting to add VHs from stereo layers. Because the z resolution of each VH is poor, and in some cases nonexistent due to malfunctioning electronics on one end of the chamber for a group of cells, it is easy to assign nearly any plausible stereo VH to any axial combination. The z position and dip angle provide enough freedom to match the position and angle of the VH to nearly any circle desired. The discriminating power comes from requiring that the derived z positions and dip angles be consistent for all stereo VH's added to the axial combination. Axial combinations with 10 consistent VH's are considered first, and the one with the best χ^2 is taken as a candidate track. Its VHs are removed from the input list and the process is repeated. Once all possible 10-VH tracks are exhausted, the algorithm searches for 9-VH tracks, and continues until all tracks with at least 3 VHs are found. No origin constraining bias is applied anywhere in the algorithm.

The fourth stage of track reconstruction is performed by the track fitter. The fitter starts with the estimated track parameters from the pattern recognition. It then swims a helical trajectory through the detector material, modifying it to take into account the effects of energy loss, multiple scattering, and local variations in the magnetic field. A χ^2 is formed, and its derivatives with respect to each of the five track parameters (the curvature, the dip angle, the azimuthal angle, and two position parameters) are estimated. In addition, the matrix of second derivatives, $\partial^2\chi^2/\partial x_i \partial x_j$ where x_i and x_j are the i^{th} and j^{th} track parameters, is formed. The local minimum of χ^2 is sought iteratively using these derivatives. On each iteration, the fitter is allowed to add or delete hits to improve the hit finding rate and χ^2. When the iterations have converged, the matrix of second derivatives is inverted to form the error matrix for the track parameters.

4.2.3 CDC Performance

The performance of the CDC is quantified by the fraction of tracks reconstructed, and how well those tracks' reconstructed parameters match the properties of the particles that created them.

Tracking Efficiency

The reconstruction efficiency can be estimated by comparing the number of tracks found in data against those found in a Monte Carlo simulation. The JETSET 7.4 generator [30], with SLD adjusted heavy flavor decays, described in Chapter 5, is used in this comparison.

Figure 4.4 shows the reconstructed track multiplicity for selected hadronic events in data and Monte Carlo, after track and event selection described in Section 6.2.3. The effect of this discrepancy in the observed number of tracks can also be seen in Figures 4.6 and 4.5, and its effects on the analysis of this thesis will be discussed in Section 6.3.

Comparisons of the number of tracks in data and Monte Carlo as functions of momentum and polar angle ($\cos\theta$) appear in Figures 4.6 and 4.5. The observed momentum dependence of the discrepancy between data and Monte Carlo could be a mismodeling of the momentum spectrum of charged tracks from Z^0 decay, or it could be the result of finding extra "fake" tracks in the fast, collimated cores of jets, where confusion between hits on neighboring tracks is greatest.

A related quantity to the tracking efficiency is the hit-finding efficiency. Most tracks selected within the angular acceptance of the CDC are expected to have a hit in each layer of the chamber. Figure 4.8 is the hit-finding efficiency of tracks with expected hits in a wire layer, as a function of the layer. The slow dip towards the inner layers is caused by the finite two-hit resolution as the tracks become closer

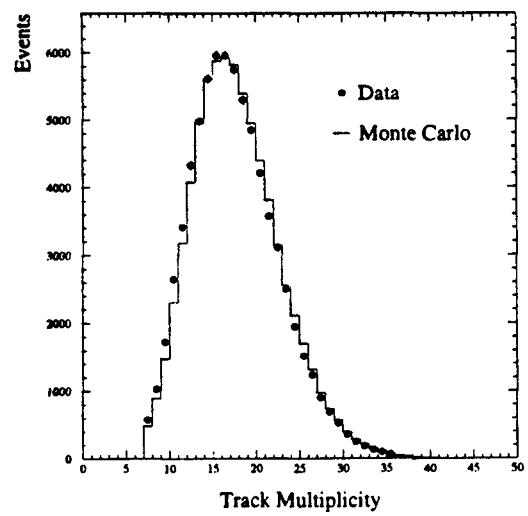

Figure 4.4: Charged track multiplicity distribution for data and Monte Carlo. On average. the data has 0.4 tracks less than the Monte Carlo, which is a 2.3% discrepancy. The effect of this on the present analysis will be discussed in Chapters 6 and 7.

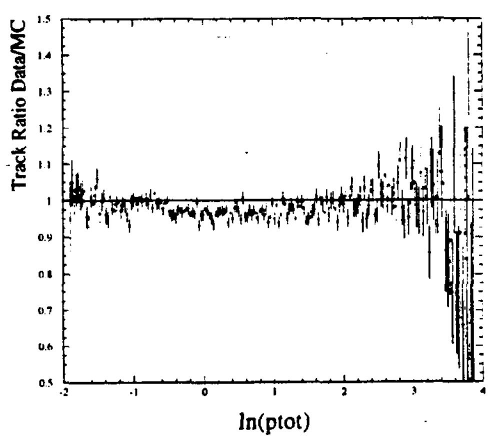

Figure 4.5: Ratio of tracks in Data to Monte Carlo as a function of $\ln(P_{tot})$, showing an overall inefficiency, but also an excess at high momentum.

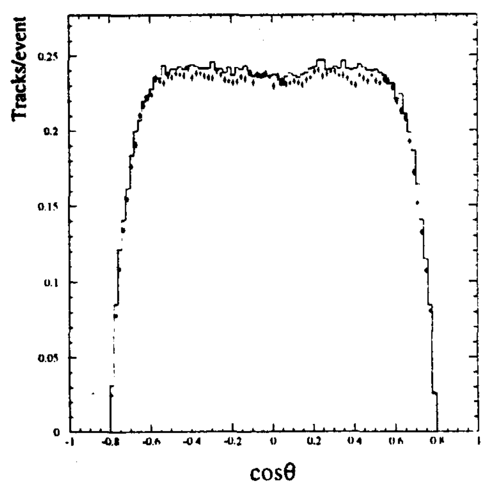

Figure 4.6: Tracking distribution as a function of $\cos\theta$ for data (points) and simulation (histogram), showing a uniform discrepancy across the angular region.

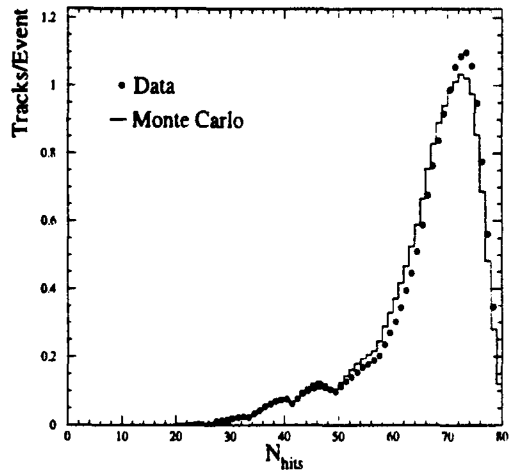

Figure 4.7: Number of hits found on selected tracks.

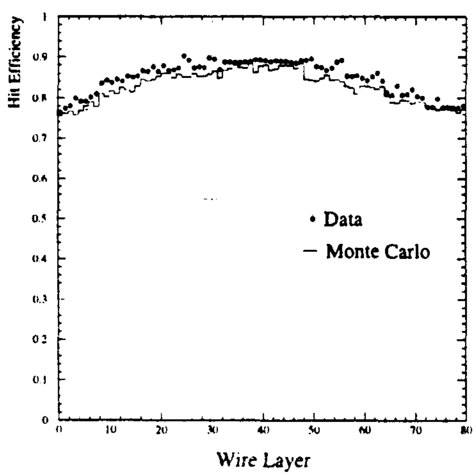

Figure 4.8: Hit-finding efficiency as a function of wire layer. The tracks are closer together in the inner layers, and the two-hit resolution reduces the hit-finding efficiency there. In addition, electromagnetic backgrounds are more prevalent in the inner layers.

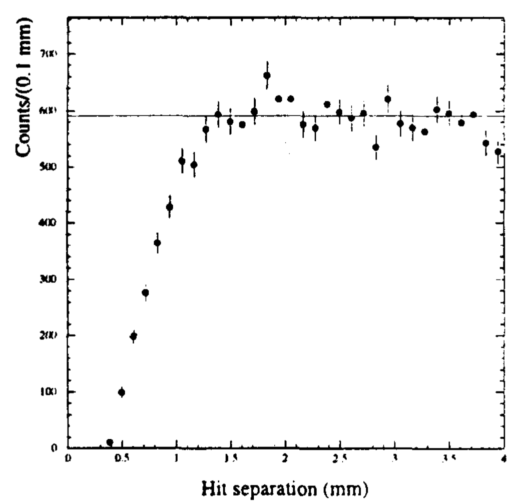

Figure 4.9: Two-hit resolution of the CDC as measured from the rate of second hits on wires.

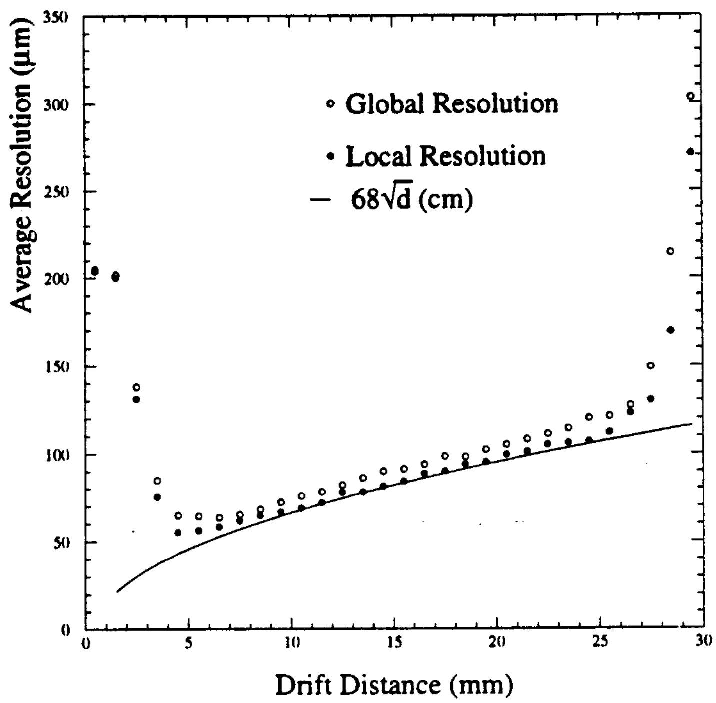

Figure 4.10: Drift distance resolution as a function of drift distance. The resolution worsens at the edges of the cell due to the larger electric fields near the field wires and sense wires, the non-uniformity of the field near the wires, and ionization statistics. The resolution in the central portion of the cell is governed by diffusion.

and more nearly parallel. The two-hit resolution itself may be measured by finding the fraction of the time a hit is found on a track if another track passed close by. Figure 4.9 shows the measured hit-finding probability for closely spaced hits. The distribution of the number of hits on tracks compared with its simulation in Figure 4.7, supports the claim that the detector's hit recording efficiency and the CDC track finding is simulated well by the Monte Carlo.

Resolution

Whereas the tracking efficiency is difficult to estimate because the proper number of tracks is unknown, the resolution of the track parameters is straightforward to measure. The main ingredients to the position and momentum resolutions of the CDC are the drift distance resolution, the radius of the chamber, the magnetic field strength, and the number of wire layers. The choices of a slow gas and a fast clock on the readout greatly enhance the drift distance resolution, shown in Figure 4.10.

The resolution on the drift distance worsens near the sense wires and the field wires because of the variable strength and direction of the electric field in those regions. The drift velocity increases near the wires, magnifying position errors for finite drift time measurement errors. The resolution in the central region of the cell is dominated by charge diffusion in the drift gas. The slow drift gas also has a small diffusion constant to minimize the drift distance errors in the bulk of the cell.

Two resolutions are shown in Figure 4.10, a global resolution, and a local resolution. The global resolution is found by finding the width of the distributions of track fit residuals as a function of drift distance. The local resolution is obtained by comparing the fit residuals between neighboring hits in a cell. The local resolution is slightly better than the global resolution owing to residual alignment effects arising from the locations of the feedthrough holes in the endplate within their machining tolerances, and tilting of the Lexan blocks within their holes. Alignment corrections cannot be made infinitely precisely, because the equilibrium sag of the wires in the combined electrostatic and gravitational fields within the chamber vary each time the voltage trips off and is restored.

The resolution on most hits in the chamber is better than 100 μm, with an average around 70 μm. These errors are incorporated into smearing the hit locations in the tracking simulation and are consistent with the observed momentum resolution.

The momentum resolution of the CDC may be estimated from the individual resolutions on the hits, and it may also be measured from $Z^0 \rightarrow \mu^+\mu^-$ decays. In the absence of hard photon radiation, the momenta of the muons are constrained to be equal and opposite at 45.6 GeV. Figure 4.11 shows the distribution of Q/P for $Z^0 \rightarrow \mu^+\mu^-$ decays. This technique probes the momentum resolution the central region of the CDC ($|\cos\theta| < 0.75$), owing to acceptance of the SLD trigger for dimuon events. Tracks which exit the chamber before leaving hits in all layers are expected to have degraded momentum resolution. A fit of two Gaussians to Figure 4.11 yields

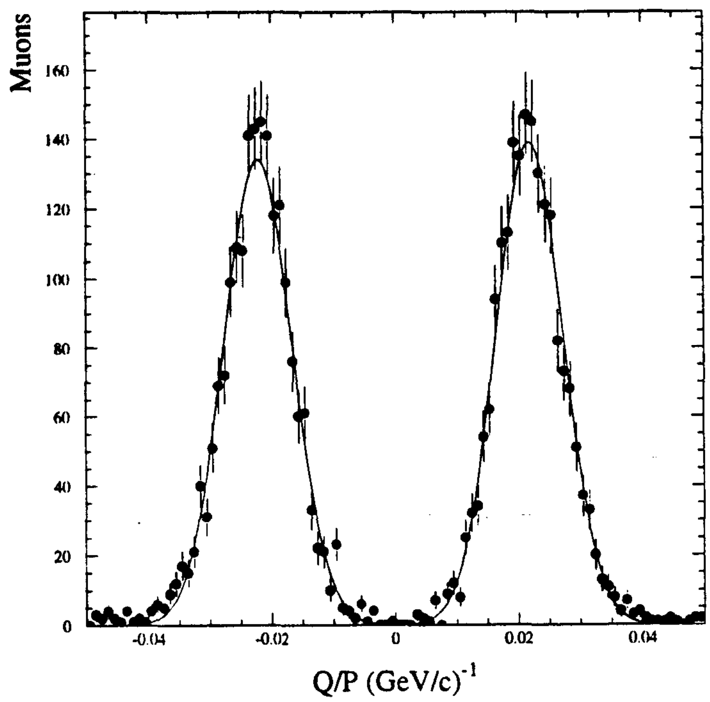

Figure 4.11: Drift chamber curvature measurements for tracks in $Z^0 \rightarrow \mu^+\mu^-$ events.

the constant term in the error of the curvature measurement. It is also seen that the probability of misassigning the sign of a charged track when it is isolated from other tracks is negligible. On the other hand, tracks may be assigned incorrect hits within dense jets, and charge misassignment becomes possible.

Cosmic ray tracks passing near the center of the CDC provide information about the momentum resolution as a function of momentum by comparing the momenta of the two halves of the track. The derived momentum resolution from these distributions is

$$dp_\perp/p_\perp^2 = \sqrt{0.0050^2 + (0.010/p_\perp)^2}, \tag{4.1}$$

where $p_\perp$ is the momentum of the particle perpendicular to the beam, measured in GeV [108].

As an independent verification of the momentum resolution of the chamber and of the absolute scales of the magnetic field within the CDC and its physical dimensions,

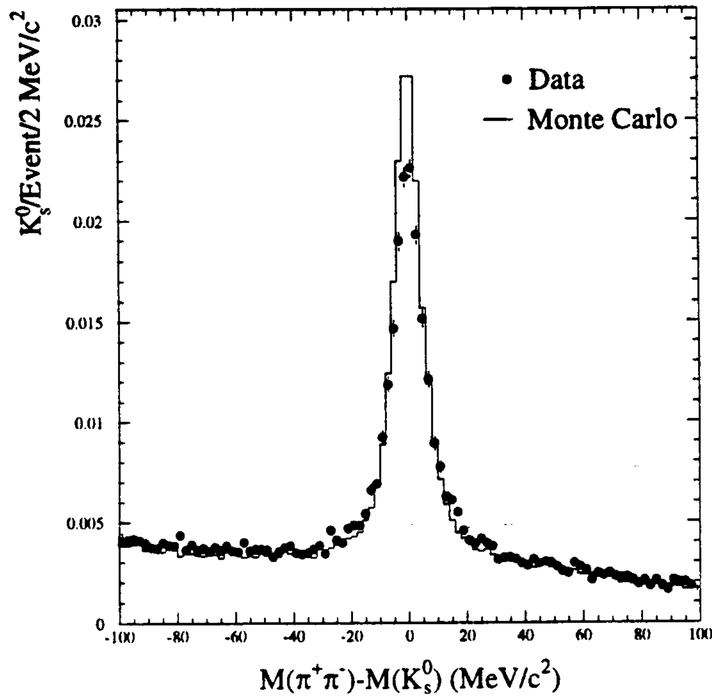

Figure 4.12: Comparison of the K_s^0 mass resolution in data and Monte Carlo. The kaon was required to start at least 10 cm from the beam axis. The Monte Carlo has a slightly more optimistic momentum resolution than the data.

the invariant mass of $K_s^0 \to \pi^+\pi^-$ decays may be calculated, as shown in Figure 4.12. The position and width of the peak, as compared with the Monte Carlo, indicate that the simulation accurately reproduces the momentum measurement.

4.3 Tracking: Vertex Detector

The SLD vertex detector (VXD) [111][112] greatly improves the measurements of the trajectories of charged particles using silicon CCD pixel detectors.

4.3.1 Mechanical Design

The individual CCD chips are mounted on alumina motherboards, nicknamed

Table 4.1: Vertex detector design parameters.

CCD count	480
Pixels/CCD	400 × 600
Pixel size	22μm× 22μm
Active area per CCD	8.5 mm × 12.7 mm
Readout time	160 ms (19 beam crossings)
Operating temperature	170 K
Layer 1 radius	29.5 mm
Layer 2 radius	33.5 mm
Layer 3 radius	37.5 mm
Layer 4 radius	41.5 mm
Radiation thickness per layer	$L/L_R = 1.064\%$
Expected hits/track	2.3
Two-hit coverage	$\|\cos\theta\| < 0.75$
One-hit coverage	$\|\cos\theta\| < 0.82$

"ladders," with eight chips per board. The CCD's alternately face towards and away from the beampipe along a ladder. The geometrical layout of 60 ladders is shown in Figure 4.14, and the salient parameters of the VXD construction are listed in Tables 4.1. There are gaps in the azimuthal coverage of each layer, but the arrangement of the ladders in the other layers guarantees two-hit coverage everywhere in φ.

The VXD provides ~120 million pieces of analog information on every event, which takes 160 ms to read out, allowing 19 beam crossings of background to accumulate. The analog signals are digitized and processed in the VXD data acquisition fastbus modules atop the detector. The first stage is to examine a 3×3 kernel around each pixel of the detector store the addresses of kernels whose signal passes a threshold criterion[‡]. A Motorola 68020 processor then examines these selected 3×3 kernels

[‡]The chip that examines these 3×3 kernels, an ASIC called a CAP chip, incorporates an "extended row filter." This filter forms the differences between neighboring pixels and compares it with the difference between the neighbors of those pixels. Because the charge accumulates on a CCD row readout, the task is to look for steps. This filter is effective in removing oscillatory background.

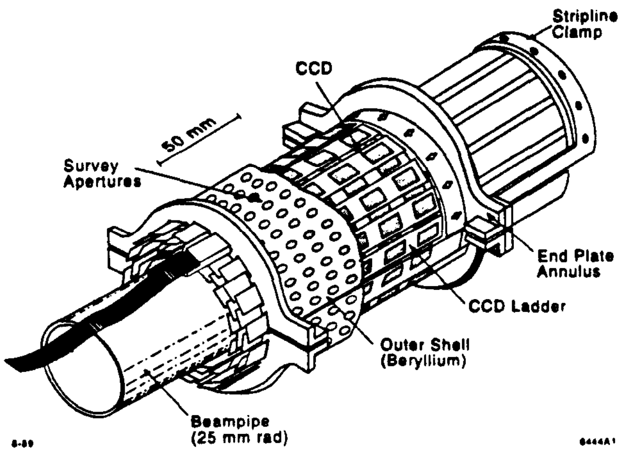

Figure 4.13: Perspective view of the VXD showing support structures and electronic attachments. The gaps between the CCD's showing on the ladders are covered by CCD's on the opposing faces of the ladders.

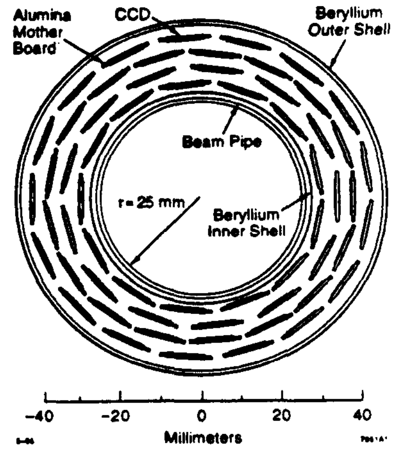

Figure 4.14: Cross-section of the VXD geometry viewed along the beam axis. Each of the 60 ladders shown has four CCD's facing the beampipe and four facing away.

to remove redundantly triggered kernels and to remove additional background. An effective filter it runs is to remove kernels in which every pixel falls below a threshold. reducing the noise while keeping the kernel threshold low.

The granularity of the VXD makes it particularly insensitive to background hits, because the occupancy, the ratio of hit pixels to all pixels, is low even in a high-noise environment. Because each hit has three space coordinates, the probability of misassociating CDC tracks with hits in the detector is small.

The VXD reduces dark current and spurious noise by operating at 180 K, maintained by cold nitrogen gas from liquid boiloff. One ladder with a broken connection was discovered after installation, and two individual CCD chips have ceased to function. Future vertex detector plans (VXD3) [181] will incorporate more robust connections to the devices to avoid these problems. There is no evidence for significant degradation of performance due to radiation damage after three years of exposure.

4.3.2 VXD Reconstruction

The first procedure applied to VXD data is to remove noise hits by identifying clusters which form long streaks in the CCD's. These are created by charged particles produced upstream of the interaction point in e-N scattering with the masks and beam walls.

The reconstruction of tracks in the VXD has two stages – finding track links and fitting the combined VXD/CDC track. The first stage has two parts to it: single hit finding and the attaching of a second hit. To find the first VXD hit, each CDC track is extrapolated to the planes of the VXD. A search ellipse is projected onto the CCD plane, with its axes determined by the CDC track error matrix and the angle of incidence. Multiple scattering in the material between the CDC and the VXD layers is taken into account when propagating this error matrix to the CCD plane. If a cluster is found, then the track parameters are adjusted so as to force the track to pass through the cluster. The errors are then recalculated with the cluster's location providing extra location information. The major source of error at this point is the ability of the track to pivot in angle around the linked cluster. A new error ellipse is projected onto the second VXD layer in which a hit is expected. If a second cluster is found, then the track is fully linked, and a search is made for more clusters because CCD chips overlap partially. Tracks with more than one hit per layer enable an accurate local alignment of the detector.

In case the two-hit finding algorithm fails for a particular track, or in case a second cluster is not expected for a track owing to non-functional detector elements. a second approach is taken. Here, the CDC track parameters are recalculated to force the track through the nominal beam position while minimizing χ^2. Then an error ellipse is projected onto a CCD plane where a hit might be expected. If a cluster is found within this ellipse, the track is allowed to pass with only one linked cluster. This technique allows high vertexing efficiency at steeper dip angles and lower momenta. It also improves the uniformity of the azimuthal coverage even with a non-functional ladder.

Adding VXD information to existing CDC tracks is accomplished after the CDC tracks have been fit and the track parameters and full CDC error matrix found.

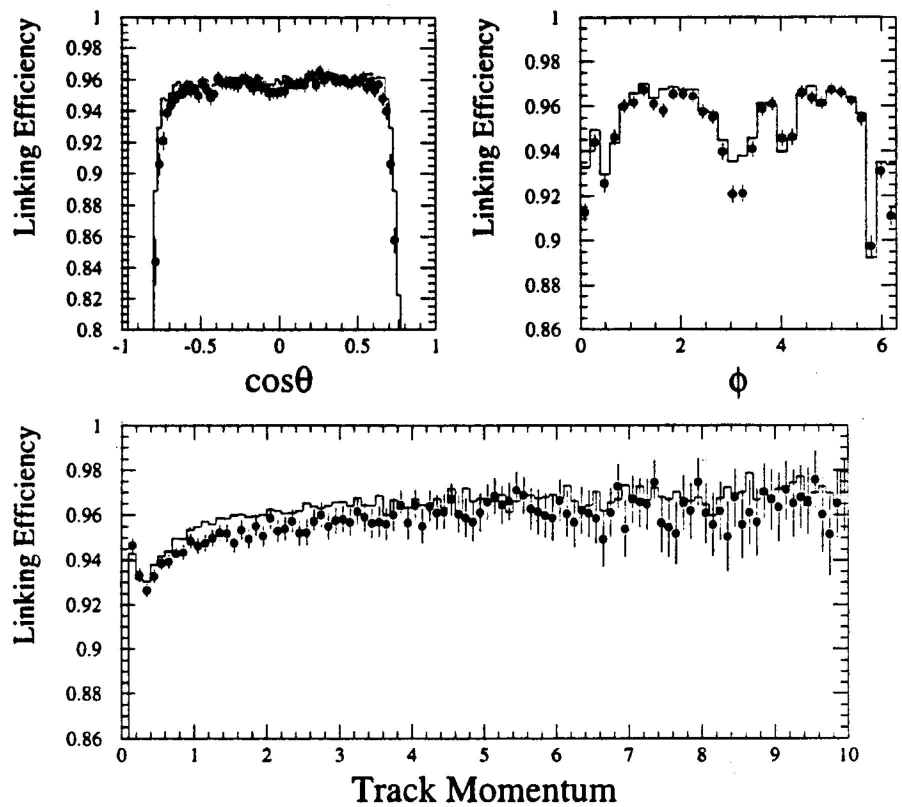

Figure 4.15: A comparison of VXD linking efficiency between data (points) and Monte Carlo (histogram), for good tracks as a function of cosθ, ϕ, and total track momentum.

Multiple scattering is taken into account using the technique of P. Billoir [113] when performing a combined fit to the CDC track and VXD hits.

4.3.3 VXD Performance

The efficiency of the VXD is measured by the fraction of tracks linked and by how well the track parameters are improved by the addition of the three-dimensional information from each VXD hit. The VXD track-linking efficiencies are shown in Figure 4.15. The structure in phi is due to the missing ladder and the nonfunctional

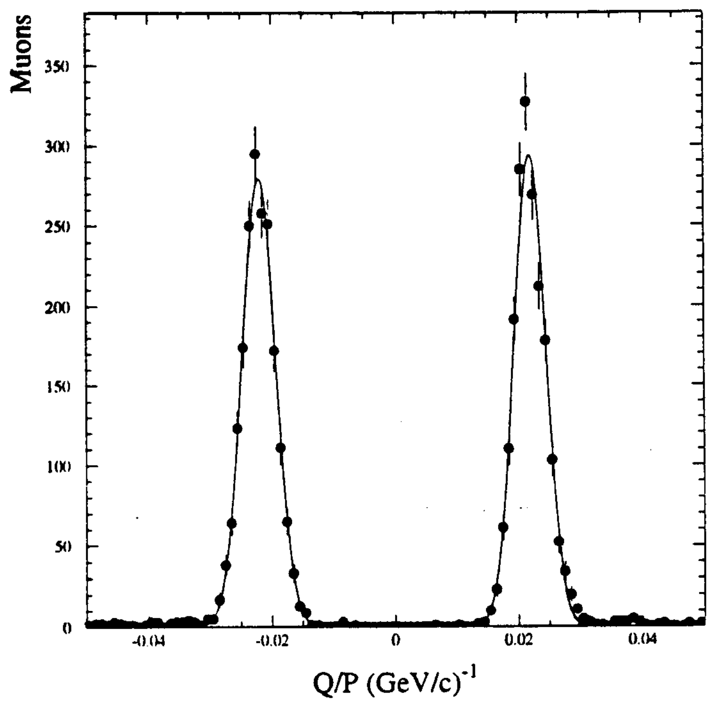

Figure 4.16: Measurement of the curvature of tracks in $Z^0 \rightarrow \mu^+\mu^-$ events using a combined fit to CDC and VXD data, fit to a sum of two Gaussians.

CCDs.

The precise position measurements from the VXD enhance the curvature measurement from the CDC because the measurement errors are small, the dip angle is constrained, and the lever arm to the VXD is large. The improvement in the curvature measurements of tracks in $Z^0 \rightarrow \mu^+\mu^-$ events can be seen by comparing the curvature resolution of Figure 4.11 (CDC alone) with those of the combined CDC-VXD fit in Figure 4.16.

The extra spatial information added by the VXD enhances the resolution of the track impact parameters more than it enhances the curvature measurement of the CDC. The achieved impact parameter resolution can be measured with the help of the two-track miss distance in dilepton events, which measures the resolution in the limit of low multiple scattering. Shown in Figure 4.17, though, is the distance of

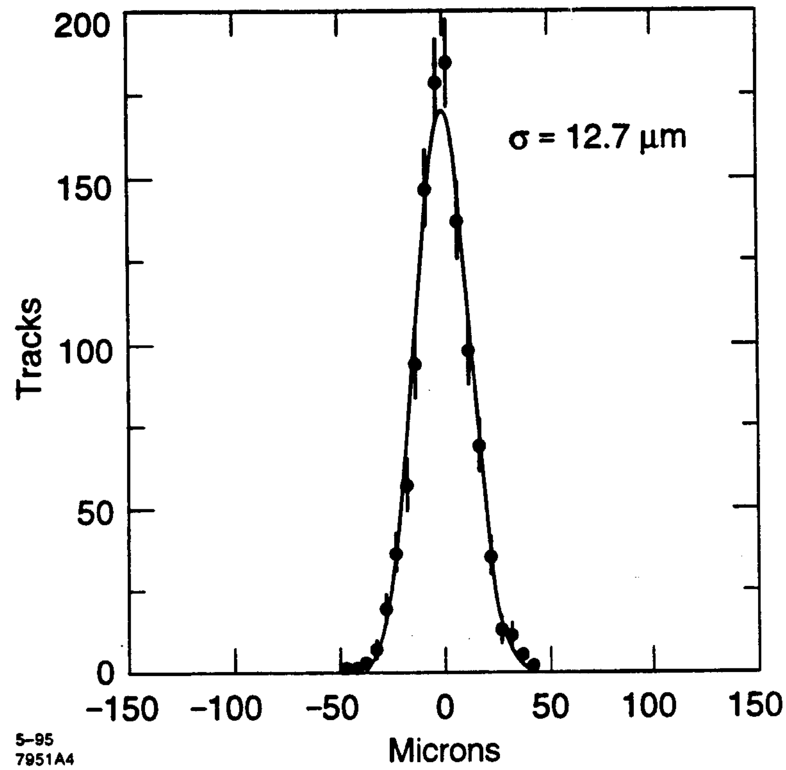

Figure 4.17: Impact parameter of tracks in $Z^0 \rightarrow \mu^+\mu^-$ events with respect to the average IP position determined from hadronic events, shown fit to a Gaussian of width 12.7μm.

closest approach of muons to the fit SLC beam spot, which provides information about the resolution of the fit IP as well. The position of the beam spot is precisely measured by averaging the primary vertices of 30 hadronic Z^0 decays.

The impact parameter resolution for tracks of arbitrary momenta may be simulated in the Monte Carlo and compared with the data. distributions of the impact parameter, its error, and the impact parameter normalized by its error are shown in Figures 6.7 and 6.8. The agreement between the data and simulation on these variables indicates that the errors are being modeled properly by the Monte Carlo.

The x-y impact parameter error from the track measurement can be roughly parameterized by

$$\delta b \simeq \sqrt{(11\mu\mathrm{m})^2 + 70\mu\mathrm{m}/\left(p|\sin\theta|^{3/2}\right)}, \tag{4.2}$$

where P is the momentum of the track and θ is its polar angle. The second term is the contribution from multiple scattering. An additional error of $6\mu m$ on the average IP position must be added in quadrature to get the true impact parameter error. This parameterization is only approximate, because hard scattering in the detector material introduces tails in the impact parameter distribution, and because the resolution of the VXD is not uniform in ϕ due to a variable lever arm between the hits on the track.

4.4 Particle ID: Cherenkov Ring Imaging Detector

The Cherenkov Ring Imaging Detector (CRID) is the particle identification system for the SLD [114]. Although it is not used in the analysis presented in this thesis, it has much to offer that will help future measurements of A_b with SLD. The CRID operates by measuring the opening angle of the cone of Cherenkov light emitted as a charged particle passes through a transparent medium in which the index of refraction retards the speed of light below the speed of the particle. This opening angle is given by

$$\theta_C = \cos^{-1}\left(\frac{1}{\beta\eta}\right), \tag{4.3}$$

where β is the speed of the particle divided by the vacuum speed of light, and η is the index of refraction in the material.

The CRID has a dual radiator structure – a liquid radiator for better resolution of lower energy particles, and a gaseous radiator for distinguishing the identities of higher energy particles. The average number of photons emitted in the Cherenkov cones of a typical particle is about 17 (liquid) and 8 (gas), so the photon detection efficiency must be very high, and the positions of the photons must be recorded very accurately. To achieve this, three-dimensional time-projection chamber (TPC) drift boxes are installed between the two radiators, separated by transparent quartz windows. The liquid radiator is a thin layer of C_6F_{12}, and the TPC box is located very close to it. The angular resolution is supplied entirely by "proximity focusing," owing to the thinness of the Cherenkov cone and the closeness of the TPC. The TPC has a second role of detecting photons emitted in the gas radiator, C_5F_{12} mixed with N_2. Because the path length the track must have in the gas required for it to emit sufficient photons is long (30 cm), the Cherenkov cones cannot be as thin as in the case of the liquid radiator. The Cherenkov light therefore needs to be focused back on the TPC sensitive planes by an array of 400 spherical mirrors mounted on the periphery of the CRID.

The TPCs are filled with a gas containing ethane, argon, and Tetrakis Dimethyl Amino Ethylene (TMAE). Of easily available substances, TMAE has the best quantum efficiency for photoionization. It also has a low energy threshold for photoionization, so the bandwidth of the system is increased. The upper edge of the bandwidth is fixed by the absorption edges of the quartz windows. A different material would have to be chosen for the windows if the sensitive material allowed less bandwidth. TMAE can also be cleaned, and the control on the O_2 levels necessary to preserve the electron lifetime is manageable. Ionization drifts towards the sense wires mounted at the ends of the drift boxes. These sense wires are shielded by opaque baffles, owing to the fact that as the ionization avalanche progresses in the high field region near the sense wires, the TMAE fluoresces, and the signal would be picked up on neighboring wires if not shielded. TPC alignment fiducials are supplied by ultraviolet laser light directed along a known trajectory through the detector.

The $K - \pi$ separation can be estimated from the Monte Carlo simulation and checked against data using samples of known composition from $K_s \rightarrow \pi^+\pi^-$ decays and $\Lambda \rightarrow p\pi^-$ decays. In addition, low multiplicity decays of the τ consist mostly of pions with a well-measured K contribution, and therefore can be used to estimate the $K - \pi$ separation in higher momentum ranges.

An interesting feature of the CRID is that its identification becomes very good when using the Cherenkov threshold region. For the gas, charged kaons do not radiate at all below ~10 GeV, while the pion threshold is near ~2.5 GeV. The particles can be identified by the lack of a ring. Recently Su Dong has performed an analysis of A_b using kaons identified with the CRID [50], estimating an efficiency for tagging kaons in $Z^0 \rightarrow b\bar{b}$ decays to be 30% with a background fraction from misidentified pions of 7.2%.

Using the Cherenkov threshold is also important for separating electrons from pions below 4 GeV and could double the electron identification efficiency. In the future,

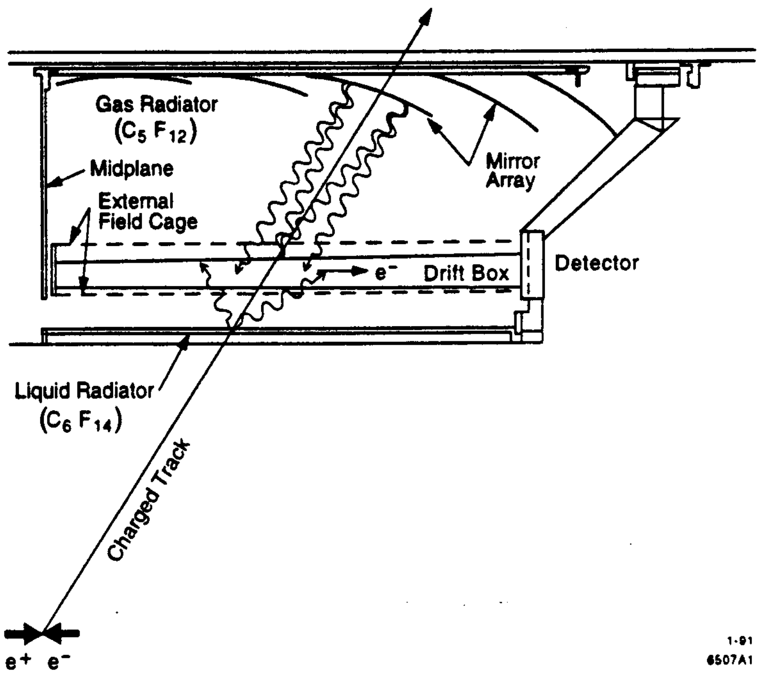

Figure 4.18: Mechanical layout of the barrel CRID

when exclusive reconstruction of B hadrons is attempted, particle identification from the CRID will most likely play a central role.

4.5 Calorimetry: Liquid Argon and WIC Pads

The SLD measures particle energy deposition in a Liquid Argon Calorimeter (LAC) [115] and a Warm Iron Calorimeter (WIC) [116]. The majority of particles produced in Z^0 decay are stopped completely by the LAC, with very little shower leakage. The cylindrical barrel section of the LAC occupies the radial region between 177 cm and 291 cm, including its cryostat, and it has a full length of 620 cm, again including the cryostat.

The LAC is segmented longitudinally into four layers, EM1, EM2, HAD1, and HAD2. Their thicknesses in radiation lengths and interaction lengths are listed in Table 4.2. The electromagnetic thickness is chosen so that roughly half of the electromagnetic shower energy is deposited in EM1 and half in EM2, with almost no leakage

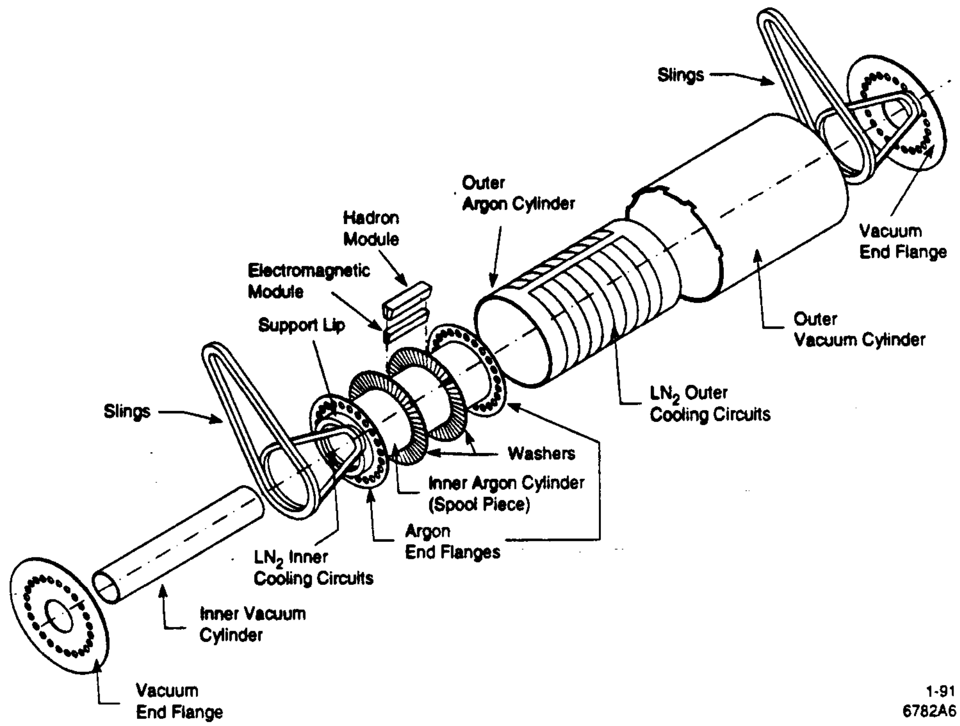

Figure 4.19: Construction of the barrel LAC

into the hadronic layers. The whole LAC is contained within the magnet coil so as not to degrade its energy resolution.

The LAC is finely segmented in polar and azimuthal angles as well. Each angular segment of lead plates is called a "tower," with argon interspersed. The tower dimensions in the electromagnetic layers are 33×36 mrad in θ and ϕ respectively in the middle of the detector, while the hadronic segmentation is twice as coarse in both directions. The towers are arranged in a projective geometry, allowing for better transverse shower shape measurements.

In addition to the barrel section of the LAC, two endcap LAC sections fill in the coverage at high $\cos\theta$. These are also formed of projective towers of lead and liquid argon, segmented nearly identically to the barrel LAC. It extends the coverage of the LAC out to $|\cos\theta| < 0.98$, although there is a region between the barrel and endcap at $|\cos\theta| = 0.84$ 70 mrad wide, with degraded energy resolution due to the

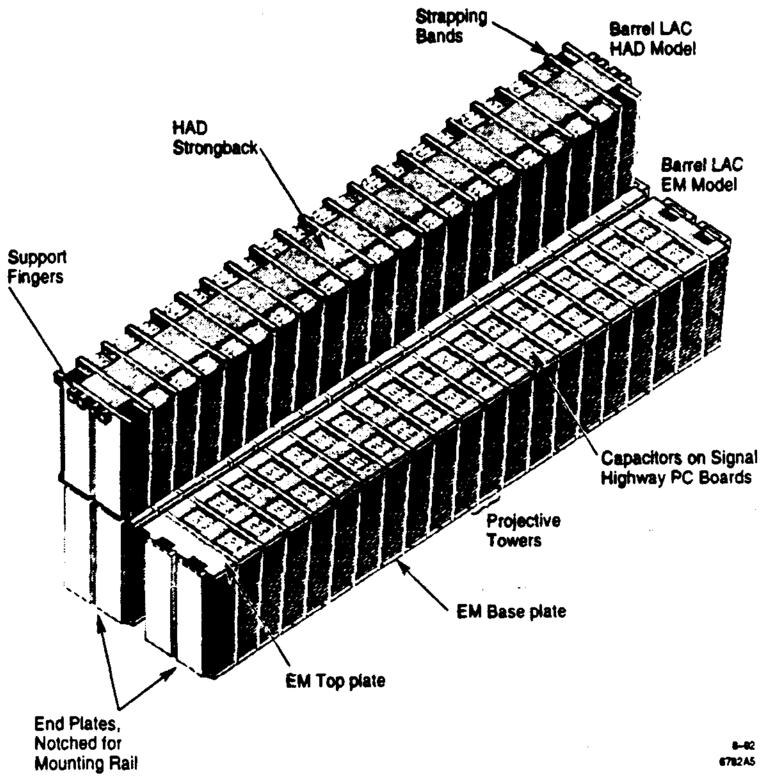

Figure 4.20: A single module of the barrel LAC

Table 4.2: Geometrical properties of the LAC and WIC pads. The thicknesses are reported at normal incidence.

Layer	Radiation Lengths	Interaction Lengths	Angular Segmentation
EM1	6.0	0.24	33 mr
EM2	15.0	0.60	33 mr
HAD1	25	1.00	66 mr
HAD2	25	1.00	66 mr
WIC1	50	2.0	66 mr
WIC2	50	2.0	66 mr
Total	171	6.84	

overlapping cryostats and the loss of hadronic coverage, as can be seen best in the SLD quadrant view (Figure 4.1).

The energy resolution of the LAC has several contributing components. The material between the LAC and the beamline degrades the resolution somewhat in an angle-dependent way. The intrinsic resolution of the calorimeter depends on the statistics of individual showers, the sampling fraction, and the ability of the calorimeter to respond to the electromagnetic and hadronic components of a hadronic shower with comparable energy scales. The LAC is an uncompensated sampling calorimeter, so its electromagnetic resolution is much better than its hadronic resolution. Material in front of the calorimeter, more prevalent in the endcap regions, affects the electromagnetic resolution more than the hadronic resolution, owing to the fact that it takes more material to start a hadronic shower on average. The average electromagnetic resolution is $\delta E_{em}/E_{em} \simeq 15\%/\sqrt{E_{em}}$, where E_{em} is the electromagnetic energy in GeV. The hadronic energy is roughly parameterized by $\delta E_{had}/E_{had} \simeq 65\%/\sqrt{E_{had}}$. In the endcap LAC, the electromagnetic energy resolution degrades to $\delta E_{em}/E_{em} \simeq 25\%/\sqrt{E_{em}}$. It is the fine segmentation and good electromagnetic resolution that enables the LAC to be used, in conjunction with tracking in the CDC, to identify electrons among the decay products of the Z^0.

Hadronic showers that fluctuate to longer lengths are contained in a secondary calorimetric device, the Warm Iron Calorimeter (WIC). Located outside of the magnet coil, the WIC also functions as a muon identifier, mechanical support, and magnetic flux return for the SLD. It consists of 18 layers of 2" thick steel plates, with plastic streamer tubes ("Iarocci tubes") [117] in between, accounting for 4 interaction lengths of material. The Iarocci tubes are instrumented with long copper pickup strips for muon tracking and broad pads which record a signal proportional to the ionization count in the neighboring tubes. The segmentation of the pads is in the form of projective towers with the same angular segmentation as the HAD section of the LAC, and divided into two layers longitudinally. Monte Carlo estimates of the energy punchthrough to the WIC are 5% for typical hadronic showers. The WIC Pads are not used in this analysis.

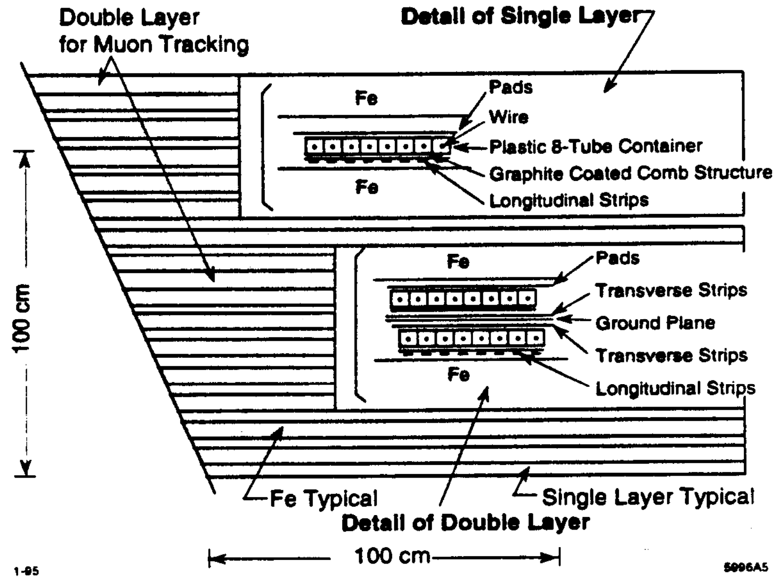

Figure 4.21: Mechanical layout of the Warm Iron Calorimeter.

4.6 Muon Identification: WIC Strips

The WIC provides information, though, which aids the study of the forward-backward left-right asymmetries [45][46]. Muons leave a characteristic signal in the WIC, as they are the only charged particles which can penetrate the steel and leave an ionization trail§. The WIC is arranged so that most of the Iarocci tubes, operated in limited streamer mode, are oriented parallel to the beamline. The WIC is organized into eight octants and two endcaps. The support arches are instrumented for coverage in the gap between the barrel octants and the endcaps. Copper strips are mounted along the lengths of the Iarocci tubes, and voltage is applied to the central wire in the tube, while the graphite coating on the tube is maintained at ground.

When a charged track passes through a tube, it ionizes the gas inside. As the oppositely charged ions travel to the field wire and to the graphite coating, an image charge builds up on the copper strip outside, producing a signal, which may be detected with sensitive amplifiers on the ends of the strips. The only information recorded by the WIC strips, though, is whether a strip was struck, not the magnitude

§Except for a small amount of pion punchthrough.

of the charge deposited. Because the ionization signal saturates the tube in limited streamer mode, no more information need be recorded. The tube size is 1 cm x 1 cm, so the fine segmentation of the system allows muon tracking with a positional resolution of 1.0 cm/hit.

Chapter 5

The SLD Monte Carlo

5.1 Introduction

Many analyses at the Z^0 rely on Monte Carlo models of both the detector and the underlying physical processes involved in the hard scattering under study. These models are indispensable for determining precisely measurement biases induced by real detectors with finite acceptances, efficiencies, and resolutions. If an analysis uses several subsystems of the detector, the modeling of the interplay between the efficiencies and acceptances of the different subsystems can become critical.

Analyses also need to correct for physical processes that are not directly under study. In particular, the analysis of measuring A_b with momentum-weighted track charge is sensitive to the details of B hadron fragmentation and decay, the properties of which have been measured at other experiments more accurately than they can be determined by SLD alone. These properties are incorporated into the physical model used, and uncertainties in them propagate into systematic errors in the final result.

The SLD Monte Carlo consists of two separate functional units: an event generator, which models the underlying physics of Z^0 decay and the physics of its unstable products, and a detector simulation model.

5.2 The Event Generator

The event generator chosen for this analysis is the JETSET 7.4 model [30], incorporating LUND string fragmentation. The electroweak processes have been checked against the forms of Chapter 1, including the effects of γ-Z^0 interference. The SLD Monte Carlo generates half of its events with an electron beam polarization of +100%, and half with −100%, with the positron beam unpolarized in both cases. In order to simulate properly the left-right asymmetry, a fraction of the right-handed events must be eliminated from the analysis, given by

$$f_{R,toss} = \frac{2|P_e|A_e}{1+|P_e|A_e}, \tag{5.1}$$

where in this case $|P_e| = 1.0$. Once the requisite balance of left-handed and right-handed events is achieved, the polarization in the Monte Carlo may be diluted by re-signing the polarization of a fraction of events.

$$f_{re-sign} = \frac{|P_e| - P_{des}}{2|P_e|}, \tag{5.2}$$

where again $|P_e|$ is the generated polarization of 100%, and P_{des} is the desired polarization.

JETSET implicitly includes initial- and final-state photon radiation, and uses a parton shower model [31] for final-state gluon radiation. Jetset also offers matrix element calculations of gluon emission to first- and second-order in α_s, and then uses the parton shower model for the higher-order effects. Rather than used a mixed approach, the SLD event generation uses a pure parton shower. This also has the advantage of the fact that JETSET retains the direction of the quark as it is emitted from the Z^0 decay, which may be compared against the quark direction after the parton shower, in order to calculate the QCD correction to asymmetry measurements.

The fragmentation functions for light-flavored hadrons* is governed by the Lund symmetric function [30] of Equation 1.42, while that for heavy-flavored hadrons is the Peterson formula [118], given in Equation 1.44. These functions can be seen in Figure 1.2.

*hadrons containing only u, d, and s quarks

Table 5.1: Mixing parameters of the SLD Monte Carlo.

Species	Fraction	x	χ
B^0	40.6%	0.75	0.180
B_s	11.5%	10.0	0.495
Average B hadron	100%	-	0.130
Charmed Hadrons		0	0

5.3 Mixing and Decay of B Mesons

The SLD Monte Carlo models the mixing of heavy mesons separately for each species. The decay distribution for a particle which starts as a B^0 at time $t = 0$ is

$$P_{B^0} = \frac{1}{2}e^{-\Gamma t}\left[1 + \cos\Delta m t\right], \quad \text{and} \tag{5.3}$$

$$P_{\overline{B}^0} = \frac{1}{2}e^{-\Gamma t}\left[1 - \cos\Delta m t\right], \tag{5.4}$$

where Γ is the reciprocal of the B^0 lifetime, and Δm is the splitting between the mass eigenstates of the B^0 system. The time-integrated mixing parameter χ_{B^0} can be expressed in terms of these quantities:

$$\chi_{B^0} = \frac{N_{\overline{B}^0}}{N_{\overline{B}^0} + N_{B^0}} = \frac{1}{2}\frac{x^2}{1+x^2}, \tag{5.5}$$

where

$$x = \frac{\Delta m}{\Gamma} \tag{5.6}$$

is the parameter most often used in measurements of the time dependence of mixing. The values used in the SLD Monte Carlo are species dependent,and are listed in Table 5.1. The species-averaged mixing parameter for B hadrons is denoted χ_B.

JETSET 7.4 is used in the SLD generator to decay all unstable† particles except the B^0, the B^-, and the B_s, and their antiparticles. This strategy was chosen because the decay particle spectra of JETSET decays of those mesons disagree with available data from CLEO and ARGUS. The previous SLD event generator was based on

†The K^0_s and the Λ are also not decayed. This point will be brought up in Section 5.5.1.

Table 5.2: SLD semileptonic B meson decay branching modes, after Reference [120]. The individual D^{**} fractions are broken down in Table 5.3. There is no simulation of $B \to D^{**}\tau\bar{\nu}_\tau$ as there is for the other leptons. The quantity for that column represents the non-resonant $B \to D^{(*)}\pi\tau\bar{\nu}_\tau$ modes present in the simulation.

Decay Mode	Branching Fraction (e,μ)	Branching Fraction (τ)
$B \to Dl\nu$	2.554%	0.4%
$B \to D^{*}l\nu$	5.874	1.1
$B \to D^{**}l\nu$	2.532	1.0%
Total	10.96%	2.5%

JETSET 6.3, which had even worse disagreements with the available data and thus had to be extensively tuned [119]. Rather than re-tune every upgraded version, it is simpler and more correct to divert the decays of B mesons to an alternative package. The package chosen was the CLEO decay simulation, described below.

5.3.1 Semileptonic Decays

The CLEO decay package simulates decays of $B \to l\nu X$ using the model of Isgur, Scora, Grinstein, and Wise (ISGW) [121]. The original paper by these authors only treated decays $B \to Dl\nu$ and $B \to D^{*}l\nu$, but since then a set of D^{**} states has been identified [122]. Available spectra from CLEO, shown in Figure 5.1, are precise enough to demonstrate that the ISGW model will not fit unless a fraction of $B \to D^{**}l\nu$ decays is incorporated. Previous Monte Carlo models invoked nonresonant $B \to D\pi l\nu$ decays, but it has been shown that only resonant decays are necessary at the current precision to match the available inclusive lepton spectra [120]. SLD's branching fractions for the semileptonic decay modes are shown in Table 5.2. Furthermore, the calculations of ISGW assume that the leptons are massless. A modification of the CLEO code for the SLD environment was made in order to keep the final-state particles on their respective mass shells by re-scaling the momenta of all decay products, making a negligible contribution except in the case of $B \to \tau\nu X$.

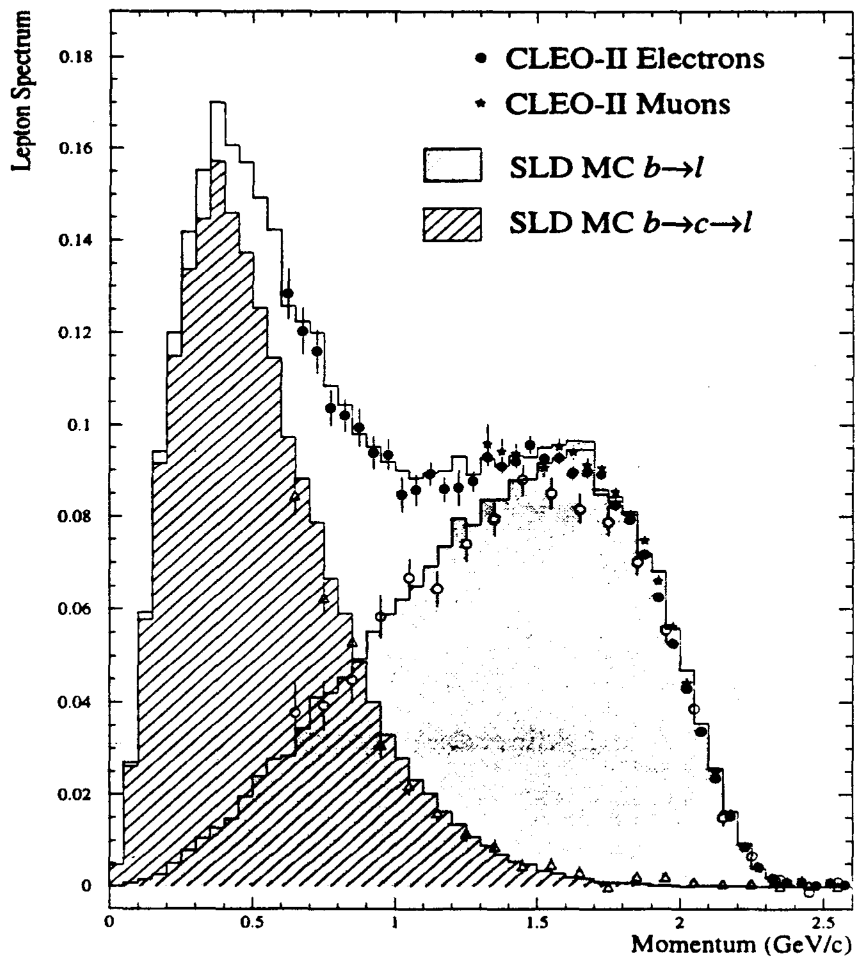

Figure 5.1: A comparison of the semileptonic decay spectra of a Monte Carlo sample composed of 50% B^0 decays and 50% $B^{\pm}$ decays, compared with data taken at the $\Upsilon(4S)$ by CLEO [120]. Open circles represent inferences of the prompt $B \to l$ signal from double tags. The momentum spectrum in the Monte Carlo has been smeared to account for the additional boost the B mesons receive at the $\Upsilon(4S)$. The Monte Carlo contributions from prompt $B \to l$ and cascade $B \to D \to l$ are shown shaded and hatched, respectively. The CLEO data have been corrected for bremsstrahlung both at the lepton production vertex and in the detector material, and also have had $B \to J/\psi X$, $B \to \tau\nu X$, and $B \to D_s X$ decays subtracted.

Table 5.3: Relative fractions of different D^{**} states generated in B decay in the SLD Monte Carlo. Fractions originate from the CLEO Monte Carlo [123].

D^{**} State	Relative Fraction
$3P^0$	12.3%
$3P^1$	24.7%
$1P^1$	45.7%
$3P^2$	17.3%

5.3.2 Hadronic Decays

The hadronic decays of the B mesons are considerably less well constrained. Fortunately, a large fraction (45%) of hadronic B decays can be reliably tabulated in known exclusive modes [123]. The charmonium states in particular leave distinctive leptonic signals in the detector, and knowledge of the branching fractions of charmonium into leptons allows inference of the charmonium content of B meson decay. But a large portion of hadronic decays must be modeled in a more inclusive manner, and the parameters of the model tuned to bring the inclusive spectra in agreement with available data.

The CLEO model handles hadronic decays by using a $V - A$ matrix element for the W emission and decay, and then, after choosing a final-state multiplicity, fragments the two quarks from the W decay. The available parameters that one may tune are the pseudoscalar fractions for the possible final-state mesons and the relative popping fractions of the quark species in the fragmentation process. These parameters are given in Table 5.4.

While neither CLEO nor ARGUS observes decays of the B_s for kinematic reasons, Monte Carlo models may extrapolate from tuned models of B^0 and B^- mesons to the B_s by replacing the light spectator with a strange quark. The Λ_b, on the other hand, is allowed to be decayed by JETSET.

Comparison of the CLEO decay model with data from CLEO [128] and ARGUS [124][125] are shown below. The total inclusive multiplicity observed by ARGUS is

Table 5.4: CLEO decay model hadronic tuning parameters.

Parameter	Value
s popping fraction	20.0%
Light pseudoscalar fraction	40.0%
Strange pseudoscalar fraction	50.0%
Charm pseudoscalar fraction	15.0%

Table 5.5: Comparison of inclusive multiplicities of $\pi^{\pm}$, $K^{\pm}$, and $P/\overline{P}$ between the CLEO/SLD decay model and ARGUS measurements [124],[125].

Quantity	Argus $\Upsilon(4S)$ Data	CLEO/SLD Model
$\langle n_{ch} \rangle$	10.81±0.05±0.23	11.04
Total $\pi^{\pm}$	8.21±0.05±0.16	8.40
$\pi^{\pm}$, no K_s^0 or Λ decay	7.17±0.05±0.14	7.46
$K^{\pm}$	1.55±0.03±0.05	1.49
Total $P/\overline{P}$	0.160±0.010±0.010	0.13
$P/\overline{P}$, no Λ decay	0.110±0.010±0.007	0.11

Table 5.6: Comparison of branching fractions of B mesons at the $\Upsilon(4S)$ to the different D mesons. Data are a CLEO/ARGUS average in August, 1994 [127].

Quantity	CLEO $\Upsilon(4S)$ Data	CLEO/SLD Model
$\mathcal{B}(B \to D^0 X)$	(62.1±2.6)%	64.8%
$\mathcal{B}(B \to D^+ X)$	(23.9±3.7)%	26.6%
$\mathcal{B}(B \to D_s^+ X)$	(10.0±2.5)%	10.7%

10.81±0.05 (stat.)±0.23 (syst.), as compared with 11.04 in the SLD tuned Monte Carlo. Most distributions agree fairly closely, except the very highest momentum tail of the inclusive pion spectrum.

The comparison of the D momentum spectrum from B decay, seen in Figures 5.3 and 5.4, shows the advantages of using the CLEO model. The D vector fraction was increased for the SLD version of the Monte Carlo because the D^0 and D^+ inclusive branching fractions disagreed with CLEO data. In order to raise the D^0 inclusive fraction, the vector fraction of charm mesons was increased, because of the preference for charmed vector mesons to decay to the D^0 state, owing to a small difference between the masses of the final states and the small phase space for the D^* decay. The momentum spectra of D mesons from B decay in the CLEO model is in agreement with the available data.

The corresponding comparison for JETSET 7.4 shows a D spectrum that is too hard, which would bias the estimated analyzing power of the momentum-weighted track charge technique.

5.4 Decays of Charmed Mesons

In order to model correctly the observed final-state particles from B hadron decay, it is important to model correctly the decays of heavy daughter hadrons, in particular the charmed hadrons. The SLD Monte Carlo uses the JETSET decay model for charmed hadrons [31], but the tables of branching fractions have been adjusted by Su Dong [129] to agree better with CLEO, ARGUS, and MARK III data. These modified tables of the decay channels are supplied in Appendix E for completeness.

5.5 Detector Simulation

The Monte Carlo needs to simulate the efficiency, acceptance, and resolution effects for observables of interest to physics analyses. Equally important, though, is the need to incorporate in the models the efficiency of the particle reconstruction algorithms applied to the data. To accomplish these dual purposes, the output of the physics

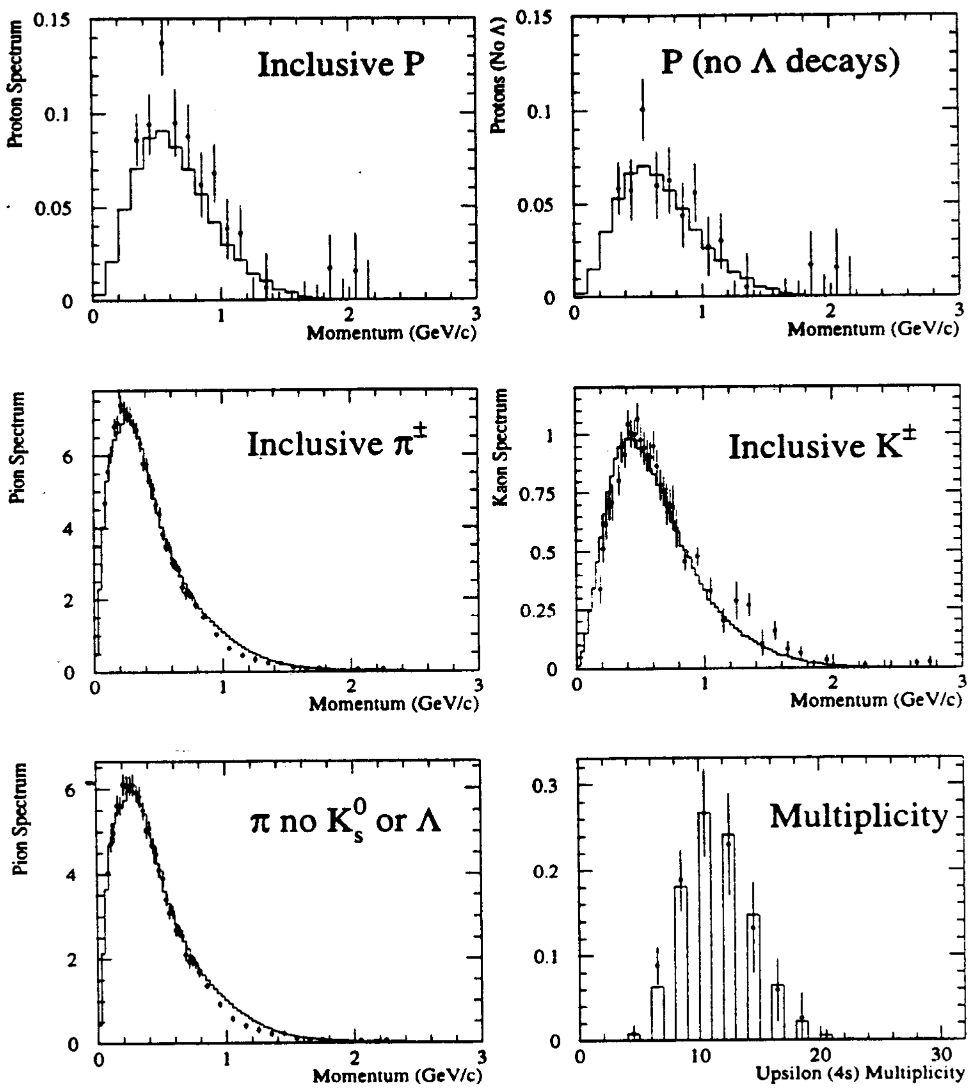

Figure 5.2: A comparison of the SLD-tuned CLEO B meson decay model (histogram) with inclusive particle spectra from Argus [124] (points). The Monte Carlo sample is a 50% B^0 and 50% $B^{\pm}$ sample, with the decay products boosted into the lab frame assuming the B meson was boosted from the $\Upsilon(4S)$ decay.

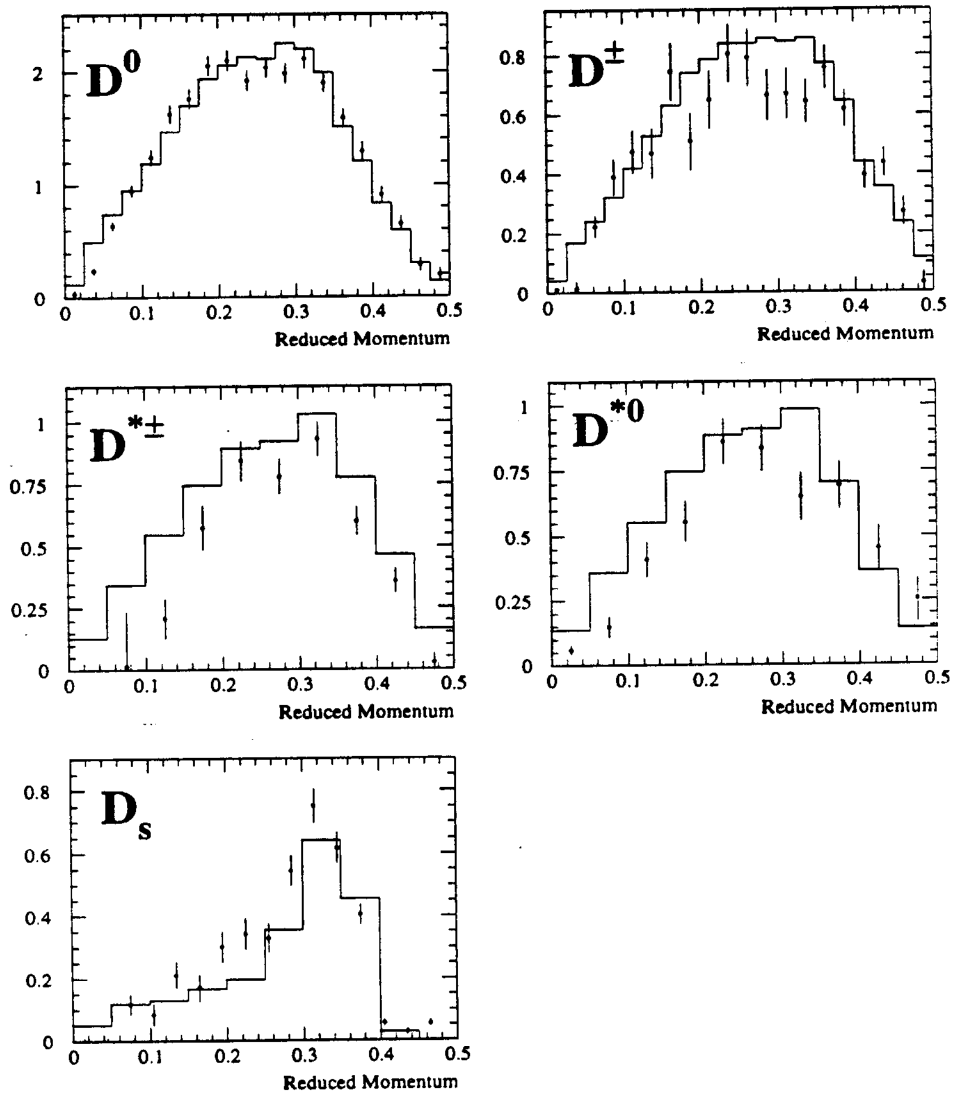

Figure 5.3: Comparison of the spectra of D mesons from B decay in the SLD Monte Carlo (histogram) against data measured by CLEO [128] (points). It is the details of these spectra to which the analyzing power of the momentum-weighted charge technique are most sensitive.

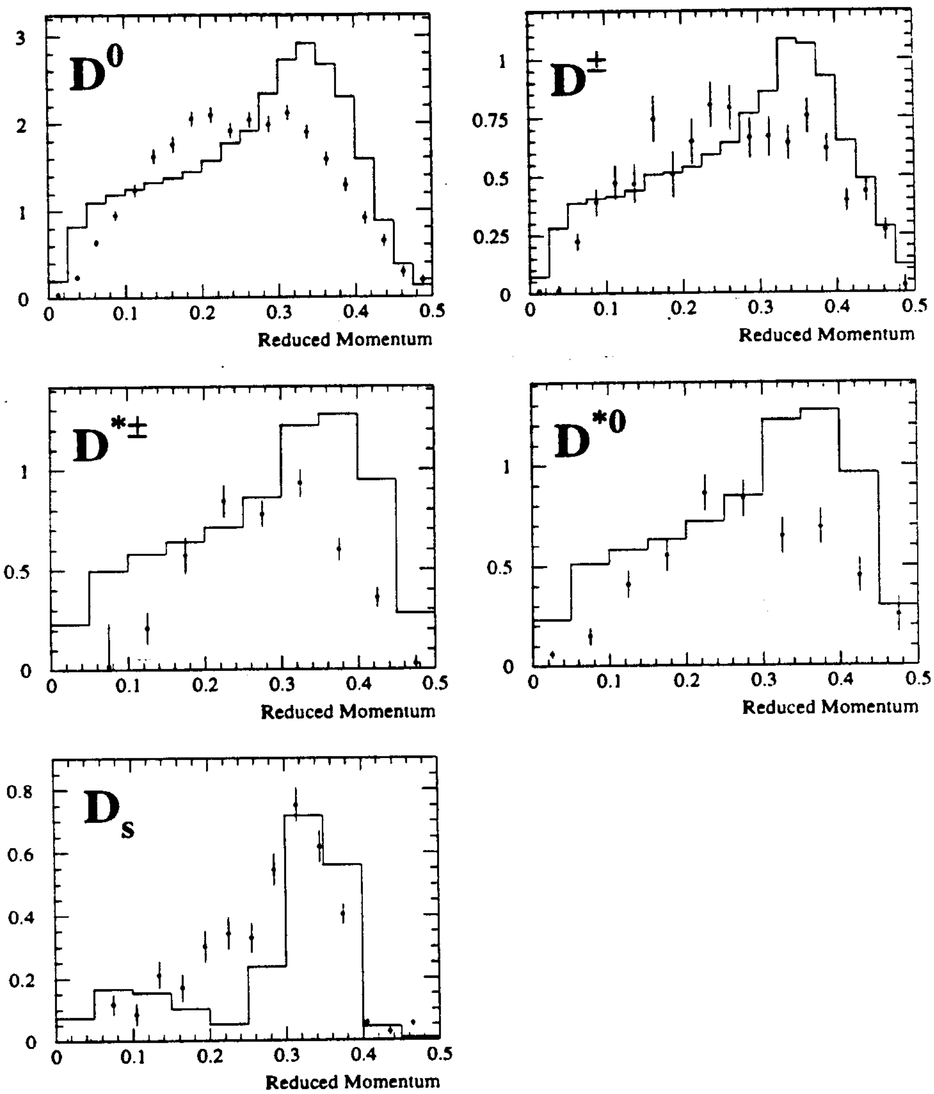

Figure 5.4: Comparison of the spectra of D mesons from B decay in the default JETSET 7.4 model (histogram) against data measured by CLEO [128] (points). The agreement is poor and shows the need to use a more accurate model.

simulation process must be in the same format as the data that is written to tape by the detector and data acquisition, so that the same reconstruction programs may be applied to simulated data as are applied to the actual data.

The input to the simulation is the set of final-state particles created by the event generator. The types, positions, momenta, and the histories of the particles as they traverse the detector must be preserved through the simulation, so that studies of efficiency may be performed. It is also often necessary to isolate model dependence arising from the generator from systematic uncertainties arising from the detector response, so the underlying event is often of great use, even after full detector simulation.

5.5.1 Detector/Particle Interactions

The resolution and efficiency of the detector subsystems depend strongly on the amount and location of material particles must pass through. Multiple scattering degrades position and momentum resolution, and electromagnetic or hadronic showers initiated in the detector material before or within the tracking volume introduce extraneous particles whose effect on the analysis must be understood.

Nearly all particles from the interaction region stop in the calorimeter, but not after showers of secondary particles are created. Some of these particles emerge from the calorimeter traveling back into the tracking volume of the detector.

These interactions must be simulated by the Monte Carlo to evaluate detector performance and to adjust the analysis for possible biases. In order for measurements from SLD to be directly comparable with those from other experiments, these interactions must be treated in a consistent manner, incorporating the best knowledge of interactions of high-energy particles and stationary material. To meet this need, the CERN Application Software Group has written a particle-detector simulation package called GEANT [130]; SLD uses Version 3.21.

GEANT starts with a list of particles from the Z^0 decay generator, a detailed description of the detector material, and a magnetic field map. It then traces the particles' trajectories until they reach boundaries of detector material, at which point GEANT calculates the interaction probability per unit of path length and randomly chooses whether or not to simulate an interaction of the particle with the detector. Geant includes the software routines from EGS4 [98] for simulating electromagnetic interactions and from GEISHA [131] for simulating hadronic interactions.

The final-state particles from the generator also include long-lived particles such as the K_s^0 and the Λ^0. These particles must not be decayed by JETSET as particles with shorter lifetimes are, because they often decay in the detector volume. They may therefore interact with the detector material before decaying.

Interactions with the calorimeter are particularly important, as both the physical layout of the material within the calorimeter and the details of the modeling of interactions between high-energy particles and the material affect the calorimeter's energy and spatial resolution.

One of GEANT's options is to simulate in full detail the showers of particles in the calorimeter by calling the GEISHA and EGS packages. Due to the high multiplicity of e^+e^- pairs in high-energy electromagnetic showers, this process consumes large amounts of computer time. This very multiplicity, however, reduces the relative statistical fluctuations in energy deposition. In addition, the transverse width of electromagnetic showers is small. These properties enable successful parameterizations which deposit energy in the sensitive elements according to carefully selected probability functions [133]. These functions describe the longitudinal development of the showers and also their transverse extent as a function of the shower depth. The simulation used by SLD is based on the GFLASH shower parameterization [132] developed by the H1 collaboration.

5.5.2 Digitization

The next step after GEANT creates its list of new particles formed by detector interactions and modifies the flight paths of old ones due to multiple scattering is to simulate the detector response to all of the particles. This stage incorporates information about which portions of the detector consist of sensitive material.

The VXD digitization simulates the charge deposited in the depletion layer of the silicon, as well as the efficiencies of the different CCD chips for recovering this charge. It also simulates random misalignments of the CCD chips by randomly fluctuating the CCD locations on each event based on their alignment errors‡.

Digitization for the CDC involves interpolating each charged particle's track to the charge collection plane for each wire that is to receive a signal from that track. The purpose is to find the closest distance from the track to the wire along the electric field lines, in order to calculate the time of the leading edge of the CDC pulse. The total ionization is calculated as a function of the particle's type, its momentum, and its total path length through the active region of the cell. The simulated charge is then distributed between the north and south readouts of the wire. Some fraction of the amplifiers and digitizers do not function, and the set of these, as determined from the data, are listed in blocks of time. If a set of electronics (usually confined to a motherboard) is non-functional in the data for a particular time, the Monte Carlo simulation of its signal will also not be present. The time of the event is taken from the background overlay event, to be discussed in Section 5.5.3. Also taken from the background overlay event is information about the state of the high voltage in each of the 10 superlayers of the CDC. If the voltage is not at least 95% of its nominal value, the layer is considered to be tripped off, and the Monte Carlo digitization does not deposit hits in the cells of that layer.

The digitization also takes into account known physical effects, such as the two-hit resolution of Figure 4.9. Additional hits are simulated at the digitization stage called "shadow hits." These are found in the data as hits on wires immediately after hits on real tracks, and typically have 40% of the charge or less. They are found more on tracks which have large charge deposition lengths and low momentum. On average. roughly 10% of real track hits are followed by shadow hits. It is hypothesized that they come from oscillations in the electronics and/or crosstalk between neighboring wires and/or the different arrival times at the sense wires of "clumps" of ionization. Some of them may be due to delta rays from the tracks, but these would produce an equal distribution of shadow hits on either side of the tracks. Only a small fraction of shadow hits are observed to precede the main track hit.

‡The real misalignments are constant, but unknown, so a random fluctuation is not a strictly correct model. Nonetheless, a constant misalignment of the CCD's in the Monte Carlo introduces biases just as bad those in the data with no information about whether they would augment or cancel the data biases.

The LAC is digitized in combination with the showering process of GEANT. The parameterized showers simulate energy depositions in the towers. The hadronic tracks' path lengths are found in the towers of the LAC and their energy is deposited using the minimum-ionizing scale as determined from cosmic-ray muon events. Also simulated are dead towers and towers with low energy response. WIC pads digitization is grouped with the LAC digitization owing to its similar tower structure.

5.5.3 Background Overlay

Accelerator-related backgrounds are difficult to simulate with Monte Carlo models — they are highly variable in time and have characteristics very different from particles from Z^0 decay. Muons generated far upstream traverse the calorimeter lengthwise. either passing through only lead tiles, or passing only through sensitive argon. Low-energy electrons looping in the magnetic field raise the occupancy of the inner tracking layers. Sometimes a spray of background particles strikes the electronics on the CDC endplate, saturating some of the amplifiers and causing all of the amplifiers in the immediate vicinity to oscillate. These backgrounds introduce hit-finding inefficiencies in the tracking chambers and add background energy to the calorimeter.

The best way to simulate accelerator-related backgrounds is to measure them from the data. For each Z^0 event identified in the data sample, a random trigger (see Section 6.2.1) taken at a nearby time is also culled from the raw tapes. The signals from the random trigger are then merged with the digitized signals from the Monte Carlo simulation. For the calorimeter, the tower energies are simply added, but for the CDC, the two-hit resolution is applied. If a background hit comes immediately before a Monte Carlo simulated hit on a track, the later hit will be lost in the simulation.